TRACING PLANETARY SCALE VOLATILE CYCLING WITH INERT GASES: A COMBINED EXPERIMENTAL AND NUMERICAL APPROACH

BY

JOHN A. KRANTZ
B.S., GEOLOGICAL ENGINEERING, COLORADO SCHOOL OF MINES, 2014
SC.M., EARTH, ENVIRONMENTAL, AND PLANETARY SCIENCES, BROWN UNIVERSITY, 2018

A DISSERTATION SUBMITTED IN PARTIAL FULFILMENT OF THE REQUIREMENTS FOR THE DEGREE OF DOCTOR OF PHILOSOPHY IN THE DEPARTMENT OF EARTH, ENVIRONMENTAL, AND PLANETARY SCIENCES AT BROWN UNIVERSITY

PROVIDENCE, RHODE ISLAND
MAY 2020

This dissertation by John A. Krantz is accepted in its present form
by the Department of Earth, Environmental, and Planetary Sciences
as satisfying the dissertation requirement for the degree of Doctor of Philosophy

Date _____ _____
Stephen W. Parman, Advisor

Recommended to the Graduate Council

Date _____ _____
Alberto E. Saal, Reader

Date _____ _____
Reid F. Cooper, Reader

Date _____ _____
Christian Huber, Reader

Date _____ _____
Peter H. Barry, Reader

Approved by the Graduate Council

Date _____ _____
Andrew G. Campbell, Dean of the Graduate School

John A. Krantz

CURRICULUM VITAE

OVERVIEW

I am a geochemist studying the physical and chemical behavior of volatiles, including noble gases, on scales ranging from individual grains to entire planets. I have a background in engineering and the geosciences and draw on my interdisciplinary training to perform high quality experimental, analytical, and numerical work. My research includes:

- Developing new experimental methods for determining solubility and diffusivity of noble gases
- High spatial-resolution measurement of noble gases in mineral phases
- Modelling the volatile contents of planetary bodies, including mantle and atmospheric reservoirs
- Modelling the onset of mantle regassing via volatile recycling in subducting slabs

EMPLOYMENT

2020 Visiting Assistant Professor, Brown University

Sustainability of Earth Resources

2014 Adjunct Professor, Colorado School of Mines

Field Geology

EDUCATION

2020 Ph.D. Earth, Environmental, and Planetary Sciences, Brown University

Dissertation: *Tracing Planetary Scale Volatile Cycling with Inert Gases: A Combined Experimental and Numerical Approach*

Advised by Stephen W. Parman

2018 Sc.M. Earth, Environmental, and Planetary Sciences, Brown University

2014 B.S. Geological Engineering (Exploration Track), Colorado School of Mines

PUBLICATIONS

Krantz, J.A., Parman, S.W., Kelley, S.P. (2019) Recycling of heavy noble gases by subduction of serpentinite. *Earth and Planetary Science Letters*. Elsevier B.V. 521, 120–127.

Krantz, J.A., Cannon, K.M. Parman, S.W. Sequestration of Xe in an early, hydrous Martian crust. *Submitted to Nature Geosciences 6 Aug. 2019.*

Krantz, J.A., Barry, P.H., Parman, S.W. Tracing Mantle Regassing and the Onset of Subduction Using Observations of H, N, and Xe. *In prep.*

AWARDS AND HONORS

2019 Brown University Deans' Faculty Fellow

2018 Goldschmidt Student Travel Grant, sponsored by NASA

2016 AGU Outstanding Student Presentation Award

PRESENTATIONS

Invited Presentations

2019 Geochemistry Seminar, WHOI, MA, USA

2017 AGU Fall Meeting, New Orleans, LA, USA

Conference Presentations

2019 Goldschmidt, Barcelona, Spain

2019 Developments In Noble Gas Understanding and Expertise VI, Zurich, Switzerland

2018 AGU Fall Meeting, Washington, D.C., USA

2018 Goldschmidt, Boston, MA, USA

2018 Lunar and Planetary Science Conference, Houston, TX, USA

2017 AGU Fall Meeting, New Orleans, LA, USA

2017 Goldschmidt, Paris, France

2017 Developments In Noble Gas Understanding and Expertise V, Paris, France

ONGOING WORK

Origin of High-An Archean Anorthosites: Fractional Crystallization of Komatiites

In collaboration with: S. Parman, G. Bybee, L. Ashwal

Onset of Mantle Regassing Controlled by Stability of Serpentinite in Subducting Slabs

In collaboration with: A. Smye, C. Jackson

TEACHING EXPERIENCE

Instructor – Sustainability of Earth's Resources (2020)

Teaching Assistant – Earth Materials (2016, 2018, 2019)

Teaching Assistant – Physical Processes in Geology (2017)

Adjunct Professor – Field Geology, Colorado School of Mines (2014)

Sheridan Center for Teaching and Learning at Brown University

2018 Course Design Seminar (Certificate II)

2014 Teaching Seminar – Reflective Teaching (Certificate I)

MENTORING

C.M. Hill, M.S., University of the Witwatersrand, 2017

- *Experimental constraints on crustal contamination in Proterozoic anorthosite*

A.T. Akinosho, B.S., College of the Holy Cross, anticipated 2020

- *Calibration of piston-cylinder P and T conditions by solid-solid reaction rate*

G. Usabal, B.S., Brown University, 2019

- *Crystallization of Proterozoic anorthosite*

J. Ruiz Gonzalez, B.S., Sonoma State University, anticipated 2020

- *Electrostatic potential of silicate ring sites*, Leadership Alliance SR-EIP

DEPARTMENTAL AND UNIVERSITY SERVICE

Graduate Council, 2016-2019

Graduate Student Council, Chair of Student Life, 2019

Graduate Student Council, Nominations Committee, 2016-2019

Graduate Student Council, Departmental Representative, 2016-2019

Student Conduct Board, 2017-2019

Departmental Faculty Representative, 2017-2019

GeoGrad Student Organization, President, 2015-2016

COURSES PREPARED

Principles and Processes of Geology

Fundamentals of Mineralogy

Mineral Resources and Sustainability

PROFESSIONAL ACTIVITIES

American Geophysical Union (Joined 2014)

Geochemical Society (Joined 2016)

COMMUNITY INVOLVEMENT AND OUTREACH

Science Teaching and Outreach Program (2017-2018)

North Scituate Volunteer Fire Department, RI **(**2016-Present)

ACKNOWLEDGEMENTS

To Steve—to whose eternal struggle—I will be brief: thank you.

—

To KR, whose enormous support has been endless.

—

To RV, without whom none of this would have been possible.

TABLE OF CONTENTS

INTRODUCTION

Classically, geologists are field scientists, spending their time outside, digging in the dirt, studying one marvellously successful experiment: Earth, or in the words of the late Carl Sagan, our "Pale Blue Dot." By unravelling the mysteries hidden within every mountain and sea, we try to work backwards to understand how they formed, where they came from, and how that relates to the modern world. Nature, however, is not always a willing participant in this investigation: erosion erases entire sections of the rock record, alteration hides the original character of a rock, and tectonics bury huge swaths of land. Natural processes, as any geologist will attest, are messy.

Our natural experiment requires teasing apart the influence of every process to identify the original rock and its composition. The experimentalist, however, takes the opposite approach: nature is complicated, instead let us run our own experiments. The temperature of the reaction will be set, the composition of our rock will be exactly what we intend, reactions will proceed for as long as we allow them, as many times as we allow them, and we can repeat them.

This forward approach to geology is, to many, the very antithesis of what they adore: replacing mountain tops with bench tops, fires with furnaces, and digging with decanting. Nonetheless, experiments provide the foundation for understanding the natural world. It is based on the results of experimental work that we interpret our observations, validate our models, and connect inputs to outputs. This thesis is the result of years of experimental work aimed at exactly those goals.

Earth, home to all life as we have ever known it, is today a welcoming and hospitable world. This, however, has not always been the case: the early Earth was an inhospitable place, steadily bombarded with meteorites, hundreds of degrees hotter than today, and with, at times, an atmosphere composed of rock vapor (Sleep *et al.*, 2001). Preston Cloud—a geologist at the University of California, Santa Barbara—dubbed this early period of Earth history the Hadean (1972); so inhospitable was this time, he felt, that it deserved the very name of the Greek god of the underworld.

How then did the Earth, unlike every other planet we know of, become a Pale *Blue* Dot? Perhaps equally importantly for humanity, we must also ask why this ocean planet is dotted with land—havens for life? While nearly all materials from the Hadean (> 4 Ga) have been destroyed, a number of detrital zircons contain direct evidence of the conditions of the early Earth going as far back as 4.404 Ga (Wilde *et al.*, 2001). Preserved within the oxygen isotopes of these ancient crystals is a record of liquid water and surface temperatures <200 °C at 4.4 Ga (Valley *et al.*, 2002). Thus, early, thermophilic life may have experienced less of a Hadean hellscape and more of a pleasant sauna.

The continents as we recognize them, however, would not form for billions of years after these early zircons crystallized. Though debate remains, a consensus is being approached that these large, stable land masses began forming 2.5 to 3.0 Ga as a result of subduction processes (e.g., Fisher and Vervoort, 2018; Keller and Schoene, 2012; Shirey and Richardson, 2011; Tang *et al.*, 2018). This marks, perhaps, the single most important period in Earth history: onset of modern subduction, formation of stable continents, and the beginning of the Great Oxidation Event (Lyons *et al.*, 2014).

In an ongoing effort to better understand this period, this thesis represents the results of experiments and numerical models, each intended to be a piecewise improvement. Despite being physically and biologically important, volatiles like water and carbon dioxide are challenging subjects for analytical investigation. They readily react with any number of other materials and have limited potential for isotopic analysis. There are, however, other volatiles which are less reactive and have a greater variety of isotopic information available. At the extreme opposite end of reactivity are the nominally inert noble gases. The noble gases experience the same physical processes which the major, life-essential volatiles experience without the complexity of chemical interactions. As such, this thesis focuses on improving our understanding of how the noble gases interact with geological materials—particularly during subduction—and the implications thereof.

Tracing volatiles during subduction (Chapters 1-3)

The first chapter presents a manuscript entitled "Recycling of heavy noble gases by subduction of serpentinite" and published in *Earth and Planetary Science Letters*. In this chapter we provide constraints on the role of altered lithospheric mantle in recycling noble gases. Experimentally-measured solubilities for the full suite of noble gases in natural serpentinite are presented. Serpentinite fractionates the heavy noble gases, with solubilities increasing from Ar to Kr to Xe. Kr/Ar and Xe/Ar ratios in MORB are quite similar to those predicted for subducted serpentinite, consistent with most heavy noble gases in the MORB-source coming from subducted serpentinite. Heavy noble gas elemental ratios in most EM1- and EM2-type OIBs can also be explained primarily by serpentinite recycling. A prominent exception is Iceland, which appears to require dominantly sediment recycling, with little or no serpentinite. HIMU OIBs

have highly fractionated elemental ratios that cannot be explained by serpentinite recycling but are consistent with recycling via amphibole in altered oceanic crust (Chavrit *et al.*, 2016).

The second chapter presents a manuscript entitled "Tracing mantle regassing and the onset of subduction" and in preparation for submission to *Geochemical Perspectives Letters*. The distribution of volatiles between the surface and interior of the Earth is largely controlled by two processes: degassing at mid-ocean ridges and regassing in subduction zones. As major volatiles like water and carbon dioxide are challenging to track through geological time, we use more inert volatiles (nitrogen and xenon) to provide constraints on the physical processes experienced by volatiles while avoiding the complexity of chemical reactions. Thus, it is possible to use relatively rare volatiles to trace more important major volatiles. The results of our model constrain the degree to which the mantle has been processed (8-8.5 reservoirs processed). The constraints from the coupled N-Xe system are also used to model the evolution of H. The timing of the mantle's transition from degassing to regassing is calculated for each volatile system studied. These results show that volatile input to the mantle increased during the Archean, overtaking outgassing at 3.1 Ga, 2.5 Ga, and 1.8 Ga for H, N, and Xe, respectively. The timing of the transition to a net regassing regime is consistent with models of the onset of subduction (Keller and Schoene, 2012; Shirey and Richardson, 2011; Tang *et al.*, 2018).

The third chapter presents a manuscript entitled "Komatiitic origin of Archean anorthosites." Anorthosites from the Archean are characterized by their high Ca content and unique, megacrystic texture. These megacrystic anorthosites formed only between 2.5 and 3.8 Ga and are closely associated with contemporaneous greenstone belts. Previous works have speculated on a connection between these anorthosites and komatiites, which are similarly temporally constrained (Ashwal and Bybee, 2017). To explore this possible connection, we

perform thermodynamic modelling of the formation of Archean, megacrystic anorthosites from high-Al basalt and komatiites. The high-Ca plagioclase observed in Archean anorthosites is most consistent with fractional crystallization of komatiites, especially wet, Al-undepleted komatiites. The petrogenetic connection between Archean megacrystic anorthosites and komatiites explains, in part, the temporal restriction of megacrystic, high-Ca anorthosites to the Archean as their source—komatiites—is also restricted to that period. The cause of komatiites' temporal restriction remains an open and important question for future work. The similarity of plagioclase found in modern boninites and Archean anorthosites adds to the growing evidence that boninites are a modern parallel to komatiites, and these results imply that the Archean mantle was slightly hotter but substantially wetter than the modern mantle. That Archean anorthosites form from hydrous komatiites and abruptly stop forming 2.5 Ga suggests that the mantle was extensively degassing during the Archean and transitioned to a distinctly different tectonic regime (i.e., modern subduction) at 2.5 Ga.

Mars: A world without subduction (Chapter 4)

The fourth chapter presents a manuscript entitled "A mineralogic solution to the Martian Xe paradox" and is in review at *Geochemical Perspectives Letters*. This work explores the long-term effects of ingassing and outgassing on a planet without subduction. Where the surface of the Earth has been repeatedly processed through mantle melting and subduction, the Martian surface has been, effectively, preserved since its earliest formation. New volcanic and sedimentary units, as well as impact ejecta, have been added on top of preexisting rocks, but those preexisting rocks were not all destroyed in the process. As a result, Mars may still have material which formed within the first tens of millions of years of solar system history exposed at the surface. To

investigate events which took place within the first 100 Myr after solar system formation, the xenon isotopic system provides a complex but incredibly useful set of tools.

Xenon isotopic ratios in the Martian atmosphere are dominated by fractionation processes. Superimposed on this smooth fractionation pattern is a large overabundance of ^{129}Xe from within 100 Myr after solar system formation. Similarly, a range of Xe isotopes were produced over the first 500 Myr, however, there are no overabundances of these Xe isotopes in the Martian atmosphere. Retaining early radiogenic ^{129}Xe, while later Xe isotopes are lost is an apparent paradox. We demonstrate that hydrous minerals, especially clays, produced in the crust in the presence of an early steam atmosphere and hydrosphere (~10 Myr after accretion) could have incorporated and sequestered substantial amounts of ^{129}Xe. Subsequent atmospheric loss would have removed Xe from the atmosphere, but sequestered ^{129}Xe would be protected from this loss. The sequestered Xe could be reintroduced to the atmosphere over billion-year timescales, producing the ^{129}Xe anomaly seen today without creating anomalies in the other Xe isotopes. If excavated exposures of these primordial clays are present on Mars today, analyzing their noble gas contents should distinguish them from later hydrated silicates produced by low-temperature weathering.

References

Ashwal, L.D., Bybee, G.M. (2017) Crustal evolution and the temporality of anorthosites. *Earth-Science Reviews*. Elsevier 173, 307–330.

Chavrit, D., Burgess, R., Sumino, H., Teagle, D.A.H., Droop, G., Shimizu, A., Ballentine, C.J. (2016) The contribution of hydrothermally altered ocean crust to the mantle halogen and noble gas cycles. *Geochimica et Cosmochimica Acta*. Elsevier Ltd 183, 106–124.

Cloud, P. (1972) A Working Model of the Primitive Earth. *American Journal of Science* 272, 537–548.

Fisher, C.M., Vervoort, J.D. (2018) Using the magmatic record to constrain the growth of continental crust — The Eoarchean zircon Hf record of Greenland. *Earth and Planetary Science Letters*. Elsevier B.V. 488, 79–91.

Keller, C.B., Schoene, B. (2012) Statistical geochemistry reveals disruption in secular lithospheric evolution about 2.5 Gyr ago. *Nature*. Nature Publishing Group 485, 490–493.

Lyons, T.W., Reinhard, C.T., Planavsky, N.J. (2014) The rise of oxygen in Earth's early ocean and atmosphere. *Nature*. Nature Publishing Group 506, 307–315.

Shirey, S., Richardson, S. (2011) Start of the Wilson Cycle at 3 Ga Shown by Diamonds from Subcontinental Mantle. *Science* 333, 434–437.

Sleep, N.H., Zahnle, K., Neuhoff, P.S. (2001) Initiation of clement surface conditions on the. *Proceedings of the National Academy of Sciences* 98, 3666–3672.

Tang, M., Chen, K., Rudnick, R.L. (2018) Archean upper crust transition from mafic to felsic marks the onset of plate tectonics. *Science* 351.

Valley, J.W., Peck, W.H., King, E.M., Wilde, S.A. (2002) A cool early Earth. *Geology* 30, 351–354.

Wilde, S.A., Valley, J.W., Peck, W.H., Graham, C.M. (2001) Evidence from detrital zircons for the existence of continental crust and oceans on the Earth 4.4 Gyr ago. *Nature* 409, 175–178.

CHAPTER ONE: RECYCLING OF HEAVY NOBLE GASES BY SUBDUCTION OF SERPENTINITE

John A. Krantz[a], Stephen W. Parman[a], Simon P. Kelley[b,1]

a Department of Earth, Environmental, and Planetary Sciences,

Brown University, Providence, RI

b Department of Environment, Earth, and Ecosystems,

The Open University, Milton Keynes, Buckinghamshire, UK

Submitted to:

Earth and Planetary Science Letters

9 April 2019

Accepted:

7 June 2019

1 Present address: School of Geosciences, University of Edinburgh, Edinburgh, UK.

Abstract

Isotopic analyses of natural samples suggest that the heavy noble gases (HNG; Ar, Kr, and Xe) in the mantle are dominated by components recycled by subduction (Holland and Ballentine, 2006; Kendrick et al., 2011; Parai and Mukhopadhyay, 2018; Smye et al., 2017). However, the mechanism of recycling is not clear: are they primarily trapped in pore spaces and inclusions, are the gases dissolved in the lattices of mineral phases, or are they located along grain boundaries? Serpentinite is a dominant volatile-bearing lithology in subducting plates, and experimental studies suggest that HNG may be highly soluble in serpentinite (Jackson et al., 2015; Zaikowski and Schaeffer, 1979). To understand its role in HNG recycling, the solubility of noble gases in natural serpentinite has been experimentally measured at pressures from 0.15 to 1.13 kbar. Measured solubilities for He, Ne, Ar, Kr, and Xe are $1.78 \cdot 10^{-9}$, $1.35 \cdot 10^{-10}$, $3.03 \cdot 10^{-10}$, $1.25 \cdot 10^{-9}$, and $3.29 \cdot 10^{-9}$ mol $\cdot$ g^{-1} $\cdot$ bar^{-1} with an average relative error of 9%. The solubilities are relatively high, indicating that even if less than 1% of the initial HNG estimated to be in subducting serpentinite survives slab dehydration, there would be enough remaining to dominate the mantle HNG budget. That the MORB and OIB mantle sources retain any primordial Kr or Xe in the face of such a large potential slab flux suggests subduction zones extract most (but not all) HNG from the slab at shallow depths. Serpentinite fractionates the HNG, with solubilities increasing from Ar to Kr to Xe. Kr/Ar and Xe/Ar ratios in MORB are quite similar to those predicted for subducted serpentinite, consistent with most HNG in the MORB-source coming from subducted serpentinite, possibly in combination with marine sediments. HNG ratios in most EM1- and EM2-type OIBs can also be explained primarily by serpentinite recycling. A prominent exception is Iceland, which appears to require dominantly sediment recycling, with little or no serpentinite. HIMU OIBs have highly fractionated HNG

ratios that cannot be explained by serpentinite recycling but are consistent with subduction of HNG in amphibole (Chavrit et al., 2016).

1. Introduction

Noble gases serve as powerful tracers of the chemical and physical evolution of the mantle (Allègre et al., 1987, 1983; Graham, 2002; Kurz et al., 2009, 1982; Moreira and Allègre, 1998; Mukhopadhyay, 2012; Porcelli and Ballentine, 2002). The noble gas composition of the mantle is a balance of the fluxes of gases out of the mantle (predominantly at mid-ocean ridges) and flux into the mantle at subduction zones (Moreira and Raquin, 2007; Porcelli and Wasserburg, 1995). The absolute fluxes of these gases are difficult to constrain, largely due to contamination of samples by modern atmospheric gases. Based on models which attempt to determine the flux of noble gases into subduction zones and the release of noble gases from subduction-related volcanoes, some studies have concluded that the recycling of noble gases is minimal (>98% of gas in the subducting slab returned to atmosphere) (Staudacher and Allègre, 1988). However, mounting evidence from isotopic analyses of ocean island basalts (OIBs), mid-ocean ridge basalts (MORBs), continental well gases, and exhumed subduction materials indicates that recycling of noble gases via subduction is substantial (Ballentine and Holland, 2008; Holland and Ballentine, 2006; Kendrick et al., 2018, 2011; Parai and Mukhopadhyay, 2015).

In detail, it appears that most noble gases (Ne, Ar, Kr, and Xe) are recycled into both the MORB and OIB mantle source regions, while He is not recycled. He concentrations are very low in the atmosphere and seawater because He escapes the atmosphere to space (Torgersen, 1989). Therefore, the amount of He that can be recycled into the mantle via altered oceanic crust and lithosphere is small. Studies of natural samples have concluded that from 0-16% of mantle Ne is

recycled (Holland and Ballentine, 2006; Kendrick et al., 2011; Williams and Mukhopadhyay, 2018). Uncertainty in the behavior of Ne is primarily related to uncertainty in the original Ne isotopic composition of the mantle and the amount of Ne being subducted due to its low solubility in seawater.

The heavy noble gases (Ar, Kr, and Xe) are not lost from the atmosphere to space and have relatively high solubilities in water, opening the possibility that substantial amounts of HNG are introduced into altered oceanic crust and lithosphere through hydrothermal alteration. The Xe contents of the modern mantle reflect contributions from primordial gases stored during accretion, gases produced by the decay of ^{129}I, fission of ^{244}Pu and ^{238}U, and recycled atmospheric gases. By precisely measuring the isotopes of Xe, it has been shown that 85-92% of the ^{132}Xe in MORBs and OIBs is recycled atmosphere (Parai and Mukhopadhyay, 2015). Additionally, measurements of ^{40}Ar/^{36}Ar and ^{129}Xe/^{130}Xe in MORB samples show variability, even at constant values of ^{4}He/^{3}He, which has been attributed to variable incorporation of recycled atmospheric gases (Parai et al., 2012).

Isotope ratios are the most robust tracers of noble gases in the mantle. However, elemental ratios have also been used to investigate recycling. Ratios are used because gas concentrations are affected by degassing and contamination, but by normalizing to another noble gas (most commonly Ar) these factors can be minimized for Kr and Xe. Consistent with isotopic data, the elemental ratios (Kr/Ar and Xe/Ar) also show evidence for considerable recycling (Ballentine and Holland, 2008; Kendrick et al., 2011). Somewhat surprisingly, MORB does not fall along a mixing line between air and seawater (Table 1; Figure 1). Air has low ^{84}Kr/^{36}Ar and ^{130}Xe/^{36}Ar ratios (0.0207 and 0.000113, respectively). Seawater has higher ratios than air (0.0403 and 0.000455), consistent with air-seawater partitioning (Holland and Ballentine, 2006; Patterson

et al., 1990; Pepin and Porcelli, 2002; Potter and Clynne, 1978). MORBs have even higher $^{84}Kr/^{36}Ar$ and $^{130}Xe/^{36}Ar$ ratios than seawater (0.0564 and 0.00103), which requires that a third component contribute noble gases to the MORB mantle and have HNG ratios equal to or greater than MORB. Identifying this third component is the focus of this study. Any noble gases being recycled in subducting lithosphere must be added after its formation at a mid-ocean ridge because both the mantle and basaltic crust are extensively degassed (Sarda and Graham, 1990). The main candidates for the third component are subducted sediments, altered oceanic crust (amphibolite), and altered oceanic lithospheric mantle (serpentinite).

Measurements of noble gases in oceanic sediments (Matsuda and Nagao, 1986; Staudacher and Allègre, 1988) show that they have Kr/Ar and Xe/Ar ratios greater than MORB (Fig. 1). The MORB source has thus been modelled as a mixture of seawater and oceanic sediments, with sediments carrying 13% of the gases (Ballentine and Holland, 2008). There is, however, significant variation in the noble gas compositions of oceanic sediments. If the MORB source is not well mixed, control of HNG by sediment subduction should result in a wide range of MORB compositions. Conversely, if the MORB source is well mixed, the third component should be a weighted average of sediments being subducted, but there is currently insufficient data to test this hypothesis. With the limited existing data, MORB appears to have fairly constant Kr/Ar and Xe/Ar ratios, and evidence from multiple systems indicates that the MORB source is not well mixed (Parai et al., 2012; Shimizu et al., 2016). Rather, the consistency of MORB suggests that some form of thermodynamically-controlled partitioning sets the ratios.

Altered ocean lithospheric mantle is another potential source of recycled noble gases. Silicates with ring structures, like serpentine, have high noble gas solubilities (Jackson et al., 2015, 2013a; Zaikowski and Schaeffer, 1979). Serpentinite, a product of hydrothermal alteration

of lithospheric mantle, is abundant in subducting slabs and has noble gas contents acquired by equilibration with seawater-derived hydrothermal fluids carrying surface derived gases. Its potential to hold large amounts of noble gases means serpentinite could transport substantial quantities into the mantle. Noble gas solubility in serpentine and magnetite (an important accessory phase in serpentinite) have previously been studied in the context of meteorites. These studies found extremely high solubilities for both phases (Lancet and Anders, 1973; Zaikowski and Schaeffer, 1979). Such high solubilities were likely the result of inclusions produced in the samples during the synthesis experiments and analyzed by melting the entire sample. More recent studies can take advantage of in-situ laser-ablation analyses to avoid inclusion-rich areas. These experiments have found much lower solubilities for He, Ne and Ar, though still high relative to mantle phases such as olivine and pyroxene (Jackson et al., 2015). However, these studies do not include Kr and Xe, the noble gases with the clearest recycling signature.

Natural serpentinites, and their residues after dehydration, have high Kr/Ar and Xe/Ar ratios, much like sediments (Fig. 2) (Kendrick et al., 2011). Recent work indicates Ne is also recycled, possibly by subduction of serpentinite (Williams and Mukhopadhyay, 2018). Thus, serpentinites appear to be a good candidate for the third component contributing heavy noble gases to the MORB source, potentially in combination with sediments. The high Kr/Ar and Xe/Ar ratios in natural samples of dehydrated serpentinite (Kendrick et al., 2011) implies that noble gases can be retained during transport through subduction zones and possibly carried deep into the mantle (Fig. 2). Additional evidence for the retention of noble gases by subducted serpentine can be found in inclusions of serpentine within olivines from the Higashi-Akaishi peridotite body. These samples contain atmosphere-derived noble gases in near-seawater proportions (Sumino et al., 2010) and have retained this signature through the dewatering of the

subducting slab, hydration reactions in the mantle-wedge, and exhumation from depths of up to 120km (Mizukami and Wallis, 2005).

Serpentine contains as much as 15 wt% water and is a major source of volatiles in subduction zone systems (Rüpke et al., 2004). However, the fingerprints of individual components of water are difficult to trace through subduction. If the noble gases are recycled by serpentinite, they may be good tracers of water cycling into and throughout the mantle. This has been demonstrated in studies which use serpentinite-derived noble gases to trace much of the water involved in subduction (e.g., Rüpke et al. 2004) as well as other incompatible, fluid mobile elements (Bebout et al., 1999; Kendrick et al., 2011).

To constrain the role of serpentinites in recycling noble gases into the mantle, this study experimentally investigates the solubility of noble gases in natural serpentinites primarily composed of antigorite, the high-pressure phase of serpentine. Natural serpentinites gain noble gases during hydrothermal alteration of the lithospheric mantle at mid-ocean ridges, along the seafloor, and via fractures at the outer rise of subduction zones (Kerrick, 2002; Peacock, 2001; Ranero et al., 2003). In some areas, serpentinization extends to at least 40km depth (Li and Lee, 2006). Since seawater is the source of the hydrothermal fluids causing serpentinization, it is expected that the noble gas contents of serpentinite reflect equilibration with seawater as well as any fluid inclusions trapped within the serpentinite. The results of these new experiments indicate that enough HNG are being subducted in serpentinites to dominate the mantle budget, consistent with isotopic studies. Kr/Ar and Xe/Ar ratios in MORBs and OIBs are similar to the ratios we predict to be present in subducted serpentinite, based on our experimental results, suggesting that volatiles in the MORB and OIB mantle sources are primarily sourced from serpentinite.

2. Methods

2.1 Starting Materials

Samples were prepared from a natural, relatively homogenous serpentinite containing randomly oriented antigorite, along with a small amount of magnetite. The composition of the serpentinite is given in Supplementary Table S1. The bulk sample was sectioned into individual samples (3 x 1.5 x 0.5 mm) using a low-speed diamond blade wafering saw. Samples were ground to thicknesses less than 0.2 mm and polished with alumina powder and colloidal silica (Fig. 3).

2.2 Experimental Methods

Noble gases were dissolved into serpentinite using a TZM-type externally-heated pressure vessel apparatus placed in a horizontal furnace. An equal mixture of either He-Ne-Ar or Ar-Kr-Xe gas was used as the pressure medium for all experiments, precisely controlling the fugacity of the noble gases. Observed pressure loss over the course of an experiment was less than 1% of the total pressure. Reported pressures are those recorded at the end of the experiment, before quenching. Experiments were conducted at a temperature of 350 ± 5°C, pressures ranging from 0.15 to 1.13 kbar, and for durations ranging from 24 to 188 hours. Initial heating asymptotically approached the target temperature over ten minutes. Temperature and pressure measurements were made using a Type K thermocouple and an Astra gauge. Graphite filler rods were used to prevent convection and minimize gas volumes within the pressure vessel. The filler rods also contain adsorbed water, which reduces the extent of antigorite dehydration. Oxygen fugacity is likely controlled by the molybdenum in the pressure vessel (Mo-MoO buffer).

Each experiment contained three serpentinite samples, contained in separate graphite capsules with loose lids. Previous work indicates that graphite capsules do not significantly affect noble gas solubilities or cause reactions between the sample and capsule (Jackson et al., 2013a). Experiments were quenched by turning off and opening the furnace, allowing the vessel to cool against air. The vessel cooled to ~35°C within 15 minutes. Once cooled, the pressure vessel was rapidly depressurized and unloaded.

2.3 Analytical Methods

Noble gas concentrations in the run products were determined using UV laser ablation-mass spectrometry at The Open University, UK (Heber et al., 2007; Jackson et al., 2015). Laser pulse frequencies of 5-20 Hz were used with ablation times of 3-45 seconds to achieve desired pit depths. Three SAES AP-10 getters removed active gases released during ablation, before introduction of the gases into a MAP215-50 mass spectrometer. ^{4}He, ^{22}Ne, ^{40}Ar, ^{84}Kr, and ^{132}Xe were measured by a multiplier collector in peak hopping mode. The sensitivity of the mass spectrometer was determined by gas pipetting a known volume of noble gases with known isotopic ratios into the mass spectrometer. Blanks were determined as a function of time during each session (defined as continuous analyses on a single port, during a single day). During He-Ne-Ar experiment analyses, blanks accounted for, on average, 9%, 32%, and 23% of the He, Ne, and Ar signals, respectively. For Ar-Kr-Xe experiments, blanks accounted for 55%, 45%, and 41% of the Ar, Kr, and Xe signals, respectively. In all cases, blanks were consistent and predictable as a function of time (R^2 >90%), with the majority of deviations from the expected blank contributions resulting from the release of unexpectedly large quantities of gas (i.e., "hot spots," likely fluid inclusions).

The volume of each pit is measured in order to calculate concentrations for the extracted noble gases. Laser ablation pit volumes were determined using a Zygo Instruments white light interferometer (Figure 4). The instrument creates a map of the ablated surface and surroundings which necessitates minimal interpolation of unknown values. A pre-ablation surface is calculated by masking out the pit area and interpolating across this area. Ablation volume is then calculated as the difference between the interpolated original surface and measured post-ablation surface. If positive-relief rims are present after ablation (from redeposition of ablated materials), these volumes are not included in the calculations by excluding points above the interpolated original surface. Additional scatter is present in the data from shallow pits and pits with complex geometries. Based on previous work, uncertainties of ±15% on the pit volume are estimated (Jackson et al., 2015, 2013a). All samples were carbon coated before imaging with the white light interferometer to improve the reflectivity of the antigorite and moderate the reflectivity of the magnetite. More even reflectivities allow for better imaging and require less interpolation.

2.4 Calculation of Solubility

Individual analyses of noble gas concentrations were used to calculate Henry's constants. Henry's constants (H) are normalized measurements of solubility with units of mol · g^{-1} · bar^{-1}, based on the measured concentration of the gas (C) and the partial pressure of the gas during the experiment (P):

$$H_x = \frac{C_x}{P_x}$$

Ablated volumes were converted to mass using the density of serpentinite (Coleman, 1971). Several analyses have anomalous concentrations or elemental ratios, attributed to relatively large fluid inclusions, and are therefore excluded from fractionation calculations. Such anomalous

measurements were made in both experimental and control (i.e., not exposed to partial pressures above atmospheric) samples, precluding experimentally induced inclusions. Analyses of magnetite inclusions and boundaries between serpentinite and magnetite show no concentration of noble gases in magnetite above the blank, and magnetite is thus discounted as a cause of the anomalous measurements. The solubility of He and Ne was calculated as the uncertainty-weighted mean of all He-Ne-Ar experiments. Ar solubility was calculated as the uncertainty-weighted mean of all experiments within the prediction interval defined by He-Ne-Ar experiments. Kr and Xe solubilities were calculated as the uncertainty-weighted mean of all experiments within the Ar prediction interval. For calculations of Ar-Kr-Xe fractionation, uncertainty-weighted means of the only the Ar-Kr-Xe experiments within the prediction interval were used (see Supplementary Methods, Figure S1 for the basis of selection).

3. Results

3.1 Assessment of equilibrium and Henrian Behavior

To assess whether or not the noble gases equilibrated with the serpentinite during the experiment, analyses of laser ablation pits with a variety of depths were performed. An equilibrated sample should show no change of concentrations or NG ratios with depth or with the duration of the experiment. Progressively deeper ablation pits in these samples show no systematic changes in the concentrations or ratios of the noble gases, consistent with equilibrium having been reached (See Supplementary Methods, Figure S2). Likewise, variations in experimental duration do not correlate with any changes in Henry's constants, indicating that dehydration or decomposition did not substantially affect experimental solubility.

The experiments were conducted at much higher noble gas partial pressures than those found in nature. The results can thus only be applied to natural serpentinites if the solubilities are

independent of partial pressure (i.e., Henry's Law behavior). Henry's constants for the experimental serpentinites are constant for pressures ranging from 0.15 to 1.13 kbar, indicating that Henry's Law applies to these conditions (See Supplementary Methods, Figure S1).

3.2 Solubility in Serpentinite

Henry's constants for He, Ne, Ar, Kr, and Xe in serpentinite have been calculated based on the experimental measurements (Figure 5, Table 2). Each plotted Henry's constant is the average of 10-30 laser ablation spots on a single experimental sample. The large (1 order of magnitude) variation in the measured NG solubilities is likely due to the influence of fluid inclusions in these natural samples and surface contaminants from new experimental apparatus. We interpret the lowest values from the experiments run with Ar, Kr, and Xe (Fig. 5, circles) to be closest to pure antigorite-gas partitioning, though even these likely contain some fluid inclusions. The higher values represent samples with greater concentrations of fluid inclusions or surface contaminants. Analyses of serpentinite samples that were not experimentally exposed to noble gases show that randomly distributed "hot spots" containing significant quantities of noble gas with a distinct isotopic composition exist within the starting material. Similarly, fluid inclusions in olivine and clinopyroxene contain orders of magnitude more gas than their host crystals (Heber et al., 2007). On average, the bulk serpentinite being subducted in slabs will have more fluid inclusions than our data, as the experimental sample was chosen to be relatively 'clean' and the laser spots were placed to avoid inclusion-rich, 'cloudy' regions. To be conservative, we use the lowest solubility values in our calculations of recycling. The actual amount of NG recycled by serpentinite is likely to be higher, though less fractionated.

Apart from He, heavier noble gases are progressively more soluble: Ne<Ar<Kr<Xe. The new values agree with previous laser analyses for He, Ne, and Ar (Jackson et al., 2015), but are

an order of magnitude lower than the results from bulk analyses (Zaikowski and Schaeffer, 1979). The solubility of noble gases in serpentinite is 2-4 orders of magnitude higher than in common mantle silicates like olivine and pyroxene (Heber et al., 2007; Jackson et al., 2013b). The solubility of He and Ar in serpentinite is similar to that measured in single crystals of amphibole, but Ne is approximately two orders of magnitude less soluble in serpentinite than in amphibole (Jackson et al., 2013a). Currently, there are no experimental data on Kr or Xe solubility in amphibole.

4. Discussion

4.1 Subduction Mass Balance

The noble gas composition of natural serpentinites can be calculated using the new experimental serpentinite solubility data and published seawater compositions (Fig. 6). Calculations were performed using seawater as an initial source of noble gases, and by multiplying the measured $^{84}Kr/^{36}Ar$ and $^{130}Xe/^{36}Ar$, or $^{132}Xe/^{36}Ar$ where ^{130}Xe data is not available, by the experimentally determined relative solubilities of Kr to Ar and Xe to Ar:

$$\left(\frac{C^i}{C^j}\right)_{Serp} = \left(\frac{C^i}{C^j}\right)_{SW} \cdot \left(\frac{H^i}{H^j}\right)$$

Where C^i and C^j are the concentrations of two noble gases in the serpentinite (Serp) and seawater (SW), and H^i and H^j are the respective, experimentally determined Henry's Constants. Any changes in these isotope ratios are the result of physical processes only since they are primordial (not produced by radiogenic decay or fission).

To estimate the amount of heavy noble gas in subducting slabs, a simplified model consisting of sediments, altered oceanic crust (AOC), and serpentinite has been used. Noble gas

contents of the sediments and AOC were calculated using the least air-like and most gas-rich analyses from natural systems (Chavrit et al., 2016; Kendrick et al., 2011; Matsuda and Nagao, 1986), while serpentinite was modelled using the results of this study. Layer thicknesses were assessed over the full range of reported values: 1 to 12 km of sediments, 5 to 9 km of AOC, and 1 to 30 km of serpentinite (Supplementary methods; Table S2). In all cases, the serpentinite layer contains at least half of the Ar and Kr. At typical thicknesses (1 km of sediments, 7 km of AOC, and 1 km of serpentinite), Xe is distributed roughly equally between the three layers (Supplementary Methods; Figure S3). Thus, the serpentinite lithology should dominate the recycling of Kr and Ar and will be important for Xe.

Combining these thicknesses with models of global subduction rates (Hacker, 2008), calculated noble gas fluxes are: $1.11 \cdot 10^{11}$ mol/Myr of ^{36}Ar, $9.19 \cdot 10^{9}$ mol/Myr of ^{84}Kr, and $3.27 \cdot 10^{8}$ mol/Myr of ^{130}Xe. These fluxes would reach the equivalent to the total ^{36}Ar, ^{84}Kr, and ^{130}Xe contents of the depleted mantle (Marty, 2012) in 100, 65, and 35 Myr of subduction, respectively. Likewise, the fluxes would reach values equivalent to the contents of the bulk mantle in 2,800, 800 and 300 Myr respectively. In summary, if all noble gases dissolved in serpentinite made it past the subduction zone and into the deep mantle, it would completely overprint whatever primordial noble gases were there in times significantly less than the period during which subduction is known to have been active on Earth. The fact that Kr and Xe in the mantle are not completely overprinted by recycling, indicates that the majority (>99%) of subducted noble gas must escape back to the surface in the subduction zone. Thus, subduction does act as a substantial barrier for noble gas recycling, as has been previously proposed (Staudacher and Allègre, 1988), but the small percentage that remains in the slab after

dehydration and arc magma genesis is still enough to substantially affect the mantle heavy noble gas budget.

4.2 Heavy noble gas elemental ratios and the MORB source

Elemental ratios of HNG in MORB do not fall on a mixing line between air and seawater (Figure 2). This indicates that at least one additional component, with high Xe/Ar and Kr/Ar contributes to the HNG budget of the mantle. Here, we explore the extent to which the MORB composition is consistent with serpentinite subduction by calculating a mixing line between seawater and serpentinite (Fig. 6). The mixing line for experimental serpentinites passes through the field of antigorites analyzed by Kendrick et al. (2011), which were analyzed by melting, after crushing. This process removes most gases from inclusions and grain boundaries (i.e., the fluids) by crushing before melting the solids to extract the remaining gases. The correspondence of the post-crush natural samples and the experimental solubilities suggests that the experimentally measured values are dominated by the solubility of noble gases in the crystal lattice of antigorite, rather than in inclusions, and supports previous work which interprets these natural antigorites as a portion of the subducting slab. This relationship further suggests that the use of unusually inclusion-poor serpentinite and avoiding inclusions by using laser analyses was effective in estimating the inclusion-free solubilities. Additionally, the similarity of Xe/Ar and Kr/Ar ratios in natural samples before and after dehydration of antigorite to olivine-enstatite suggests that serpentinite-derived noble gas ratios are robust to modification by dehydration (Fig. 6) (Kendrick et al., 2011).

The values of Kr/Ar and Xe/Ar in MORB are near the serpentinite-seawater mixing line, consistent with the convecting mantle's noble gas inventory being controlled by the subduction of serpentinite. If the heavy noble gases act as passive tracers of other volatiles (e.g., water,

carbon, halogens), then this further suggests that most of the volatiles in the mantle were carried there by the subduction of serpentinites, not amphibole or sediments. The small divergence from the mixing line may be accounted for by the influence of relatively low Xe/Kr sediments, as has been previously suggested (Ballentine and Holland, 2008), or may represent a contribution of the fluids released during antigorite crushing (Kendrick et al., 2011).

4.3 Heavy noble gases in the OIB source

Ocean island basalts have significantly more variable HNG elemental ratios than MORB. HNG data from Hawaii, one of the most extensively and precisely studied OIBs, is shown in Fig. 7 (Trieloff et al., 2000). These HNG compositions are compared with calculated mixing lines for recycling by subduction of serpentinite. The Hawaiian samples have high Xe/Kr (relative to MORB), consistent with serpentinite being the recycled component. Noble gas data from subaqueous Loihi dunites lie along a mixing line between seawater and subducted serpentinite if modern air contamination is removed (Figure 7). No sediment contribution is required to match the HNG ratios in Hawaii's source. These trends are consistent with lithophile isotope observations which indicate that hydrothermally altered, ultramafic lower crust or lithospheric mantle (i.e., serpentinite) is present in the Hawaiian source (Lassiter and Hauri, 1998; Pietruszka et al., 2013).

Icelandic samples, in contrast, have substantially lower Xe/Kr than MORB, indicating that the dominant recycled material is likely sediments (Fig. 7), with little or indication of a subducted serpentinite component. This HNG based observation is consistent with lithophile isotopes, which suggest that subduction-processed sediments are present in the Icelandic source (Manning and Thirlwall, 2014). A clear difference exists between these mantle plumes and

indicates that heterogeneity in the heavy noble gas compositions of OIBs is related to differences in contributions from recycled materials.

Additional hotspot data for a range of ocean islands from the Polynesian region (Hanyu et al., 1999) are presented in Figure 8. These analyses only report ^{132}Xe, which has a small radiogenic component that must be accounted for. Overall, data from EM1 and EM2 Polynesian OIBs (Rarotonga, modern Rurutu lavas, Moorea and Tahiti) fall in a small field between air, seawater, and a slightly higher Xe/Kr end-member, much like the Hawaiian samples in Fig. 7. HIMU OIBs (Mangaia, Tubuai, and ancient Rurutu lavas), however, have much higher Xe/Ar and Kr/Ar ratios than MORB and other OIBs. Such high ratios cannot be explained by mixing air, seawater, sediments, and serpentinites. Analyses of natural samples of altered oceanic crust (Chavrit et al., 2016) show high Xe/Ar and Kr/Ar ratios, similar to those in HIMU OIBs, suggesting that altered oceanic crust may be the source of HNG in HIMU OIBs. This observation is in agreement with Sr-Nd-Pb isotopic studies suggesting that recycled oceanic crust is a major component of HIMU OIBs (Day and Hilton, 2011; Hanyu et al., 1999). Amphibole is one of the major phases in altered oceanic crust, and studies have demonstrated that light noble gases are highly soluble in amphiboles, similar to or more so than in serpentinite (Jackson et al., 2015). A detailed study of heavy noble gas behavior in amphibole is needed to clarify the role of amphibolite in the HIMU source.

5. Conclusions

Experimentally measured solubilities (Henry's constants) for He, Ne, Ar, Kr, and Xe are $1.78 \cdot 10^{-9}$, $1.35 \cdot 10^{-10}$, $6.86 \cdot 10^{-10}$, $1.28 \cdot 10^{-9}$, and $4.57 \cdot 10^{-9}$ mol $\cdot$ g^{-1} $\cdot$ bar^{-1} with an average relative error of 9%. Measured solubilities for He, Ne, and Ar are two orders of magnitude higher in serpentinite than in olivine and clinopyroxene, while Kr and Xe are four orders of

magnitude more soluble (Heber et al., 2007; Jackson et al., 2013b). Solubilities of noble gases (other than He) in serpentinites increase with the atomic number of the noble gas: Ne<Ar<Kr<Xe. This relationship indicates that subducting serpentinite should have fractionated HNG, with high Kr/Ar, Xe/Ar, and Xe/Kr ratios. The experimental solubilities are consistent with measurements of heavy noble gases in natural serpentinites (Kendrick et al., 2011).

The experimental results indicate that subducting hydrated mantle contains substantial amounts of heavy noble gases, and dominates the Ar, Kr and Xe budget of the convecting mantle. If the noble gases trace the flux of H_2O out of slabs, our results suggest that most of the water in the convecting mantle was carried there by serpentinite. Noble gas analyses of OIBs in Hawaii, Iceland, and Polynesia demonstrate that there is heterogeneity in the heavy noble gas composition of OIB sources. The noble gas composition of EM1- and EM2-type OIBs are consistent with HNG recycling via serpentinites with little or no sediment. HIMU OIBs, in contrast, require a component with significantly higher Kr/Ar, Xe/Ar, and Xe/Kr ratios than in serpentinite or sediments, consistent with recent analyses of altered oceanic crust (Chavrit et al., 2016). These results imply that most volatiles in the HIMU source were carried thereby altered oceanic crust and are consistent with previous work identifying relative volatile enrichment in HIMU glasses (e.g., Kendrick et al., 2017).

Acknowledgments

We thank Alison Halton, James Malley, and Sarah Sherlock for their assistance completing the noble gas analyses. This work was supported by the National Science Foundation through grant #EAR-1347772.

References

Allègre, C.J., Staudacher, T., Sarda, P., 1987. Rare gas systematics: formation of the atmosphere,

evolution and structure of the Earth's mantle. Earth Planet. Sci. Lett. 81, 127–150. https://doi.org/10.1016/0012-821X(87)90151-8

Allègre, C.J., Staudacher, T., Sarda, P., Kurz, M., 1983. Constraints on evolution of Earth's mantle from rare gas systematics. Nature 303, 762–766. https://doi.org/10.1038/303762a0

Ballentine, C.J., Holland, G., 2008. What CO 2 well gases tell us about the origin of noble gases in the mantle and their relationship to the atmosphere. Phil. Trans. R. Soc. A 366, 4183–4203. https://doi.org/10.1098/rsta.2008.0150

Bebout, G.E., Ryan, J.G., Leeman, W.P., Bebout, A.E., 1999. Fractionation of trace elements by subduction-zone metamorphism - effect of convergent-margin thermal evolution. Earth Planet. Sci. Lett. 171, 63–81. https://doi.org/10.1016/S0012-821X(99)00135-1

Chavrit, D., Burgess, R., Sumino, H., Teagle, D.A.H., Droop, G., Shimizu, A., Ballentine, C.J., 2016. The contribution of hydrothermally altered ocean crust to the mantle halogen and noble gas cycles. Geochim. Cosmochim. Acta 183, 106–124. https://doi.org/10.1016/j.gca.2016.03.014

Coleman, R.G., 1971. Petrologic and geophysical nature of serpentinites. Bull. Geol. Soc. Am. 82, 897–918. https://doi.org/10.1130/0016-7606(1971)82[897:PAGNOS]2.0.CO;2

Day, J.M.D., Hilton, D.R., 2011. Origin of 3He/4He ratios in HIMU-type basalts constrained from Canary Island lavas. Earth Planet. Sci. Lett. 305, 226–234. https://doi.org/10.1016/j.epsl.2011.03.006

Graham, D.W., 2002. Noble gas isotope geochemistry of mid-ocean and ocean island basalts: characterization of mantle source reservoirs. Rev. Mineral. Geochemistry 47, 247–317.

https://doi.org/10.2138/rmg.2002.47.8

Hacker, B.R., 2008. H2O subduction beyond arcs. Geochemistry, Geophys. Geosystems 9. https://doi.org/10.1029/2007GC001707

Hanyu, T., Kaneoka, I., Nagao, K., 1999. Noble gas study of HIMU and EM ocean island basalts in the Polynesian region. Geochim. Cosmochim. Acta 63, 1181–1201. https://doi.org/10.1016/S0016-7037(99)00044-7

Heber, V.S., Brooker, R.A., Kelley, S.P., Wood, B.J., 2007. Crystal-melt partitioning of noble gases (helium, neon, argon, krypton, and xenon) for olivine and clinopyroxene. Geochim. Cosmochim. Acta 71, 1041–1061. https://doi.org/10.1016/j.gca.2006.11.010

Holland, G., Ballentine, C.J., 2006. Seawater subduction controls the heavy noble gas composition of the mantle. Nature 441, 186–91. https://doi.org/10.1038/nature04761

Jackson, C.R.M., Parman, S.W., Kelley, S.P., Cooper, R.F., 2015. Light noble gas dissolution into ring structure-bearing materials and lattice influences on noble gas recycling. Geochim. Cosmochim. Acta 159, 1–15. https://doi.org/10.1016/j.gca.2015.02.036

Jackson, C.R.M., Parman, S.W., Kelley, S.P., Cooper, R.F., 2013a. Noble gas transport into the mantle facilitated by high solubility in amphibole. Nat. Geosci. 6, 562–565. https://doi.org/10.1038/ngeo1851

Jackson, C.R.M., Parman, S.W., Kelley, S.P., Cooper, R.F., 2013b. Constraints on light noble partitioning at the conditions of spinel-peridotite melting. Earth Planet. Sci. Lett. 384, 178–187. https://doi.org/10.1016/j.epsl.2013.09.046

Kendrick, M.A., Hémond, C., Kamenetsky, V.S., Danyushevsky, L.V., Devey, C.W., Rodemann,

T., Jackson, M.G., Perfit, M.R., 2017. Seawater cycled throughout Earth's mantle in partially serpentinized lithosphere. Nat. Geosci. 10, 222–228. https://doi.org/10.1038/NGEO2902

Kendrick, M.A., Scambelluri, M., Hermann, J., Padrón-Navarta, J.A., 2018. Halogens and noble gases in serpentinites and secondary peridotites: Implications for seawater subduction and the origin of mantle neon. Geochim. Cosmochim. Acta 235, 285–304. https://doi.org/10.1016/j.gca.2018.03.024

Kendrick, M.A., Scambelluri, M., Honda, M., Phillips, D., 2011. High abundances of noble gas and chlorine delivered to the mantle by serpentinite subduction. Nat. Geosci. 4, 807–812. https://doi.org/10.1038/ngeo1270

Kerrick, D., 2002. Serpentinite Seduction. Science (80-.). 298, 1344–1345. https://doi.org/10.1126/science.298.5597.1344

Kurz, M.D., Curtice, J., Fornari, D., Geist, D., Moreira, M., 2009. Primitive neon from the center of the Galápagos hotspot. Earth Planet. Sci. Lett. 286, 23–34. https://doi.org/10.1016/j.epsl.2009.06.008

Kurz, M.D., Jenkins, W.J., Hart, S.R., 1982. Helium isotopic systematics of oceanic islands and mantle heterogeneity. Nature 297, 43–47.

Lancet, M.S., Anders, E., 1973. Solubilities of noble gases in magnetite: implications for planetary gases in meteorites. Geochim. Cosmochim. Acta 37, 1371–1388. https://doi.org/10.1016/0016-7037(73)90067-7

Lassiter, J.C., Hauri, E.H., 1998. Osmium-isotope variations in Hawaiian lavas: Evidence for

recycled oceanic lithosphere in the Hawaiian plume. Earth Planet. Sci. Lett. 164, 483–496. https://doi.org/10.1016/S0012-821X(98)00240-4

Li, Z.X.A., Lee, C.T.A., 2006. Geochemical investigation of serpentinized oceanic lithospheric mantle in the Feather River Ophiolite, California: Implications for the recycling rate of water by subduction. Chem. Geol. 235, 161–185. https://doi.org/10.1016/j.chemgeo.2006.06.011

Manning, C.J., Thirlwall, M.F., 2014. Isotopic evidence for interaction between Öræfajökull mantle and the Eastern Rift Zone, Iceland. Contrib. to Mineral. Petrol. 167, 1–22. https://doi.org/10.1007/s00410-013-0959-1

Marty, B., 2012. The origins and concentrations of water, carbon, nitrogen and noble gases on Earth. Earth Planet. Sci. Lett. 313–314, 56–66. https://doi.org/10.1016/j.epsl.2011.10.040

Matsuda, J., Nagao, K., 1986. Sediment gas core abundances from eastern in a deep-sea Pacific equatorial. Geochem. J. 20, 71–80.

Mizukami, T., Wallis, S.R., 2005. Structural and petrological constraints on the tectonic evolution of the garnet-lherzolite facies Higashi-akaishi peridotite body, Sanbagawa belt, SW Japan. Tectonics 24, 1–17. https://doi.org/10.1029/2004TC001733

Moreira, M., Allègre, C.J., 1998. Helium-neon systematics and the structure of the mantle. Chem. Geol. 147, 53–59. https://doi.org/10.1016/S0009-2541(97)00171-X

Moreira, M., Kunz, J., Allègre, C., 1998. Rare gas systematics in popping rock: Isotopic and elemental compositions in the upper mantle. Science (80-.). 279, 1178–1181. https://doi.org/10.1126/science.279.5354.1178

Moreira, M., Raquin, A., 2007. The origin of rare gases on Earth: The noble gas "subduction barrier" revisited. Comptes Rendus - Geosci. 339, 937–945. https://doi.org/10.1016/j.crte.2007.09.009

Mukhopadhyay, S., 2012. Early differentiation and volatile accretion recorded in deep-mantle neon and xenon. Nature 486, 101–4. https://doi.org/10.1038/nature11141

Ozima, M., Podosek, F.A., 2002. Noble Gas Geochemistry. Cambridge University Press.

Parai, R., Mukhopadhyay, S., 2018. Xenon isotopic constraints on the history of volatile recycling into the mantle. Nature 560, 223–227. https://doi.org/10.1038/s41586-018-0388-4

Parai, R., Mukhopadhyay, S., 2015. The evolution of MORB and plume mantle volatile budgets: Constraints from fission Xe isotopes in Southwest Indian Ridge basalts. Geochemistry, Geophys. Geosystems 16, 719–735. https://doi.org/10.1002/2014GC005566

Parai, R., Mukhopadhyay, S., Standish, J.J., 2012. Heterogeneous upper mantle Ne, Ar and Xe isotopic compositions and a possible Dupal noble gas signature recorded in basalts from the Southwest Indian Ridge. Earth Planet. Sci. Lett. 359–360, 227–239. https://doi.org/10.1016/j.epsl.2012.10.017

Patterson, D.B., Honda, M., McDougall, I., 1990. Atmospheric contamination: a possible source for heavy noble gases in basalts from Loihi Seamount, Hawaii 17, 705–708.

Peacock, S.M., 2001. Are the lower planes of double seismic zones caused by serpentine dehydration in subducting oceanic mantle? Geology 29, 299–302. https://doi.org/10.1130/0091-7613(1980)?8<11:APCAKM>?2.0.CO

Pepin, R.O., Porcelli, D., 2002. Origin of Noble Gases in the Terrestrial Planets. Rev. Mineral.

Geochemistry 47, 191–246. https://doi.org/10.2138/rmg.2002.47.7

Pietruszka, A.J., Norman, M.D., Garcia, M.O., Marske, J.P., Burns, D.H., 2013. Chemical heterogeneity in the Hawaiian mantle plume from the alteration and dehydration of recycled oceanic crust. Earth Planet. Sci. Lett. 361, 298–309. https://doi.org/10.1016/j.epsl.2012.10.030

Porcelli, D., Ballentine, C.J., 2002. Models for Distribution of Terrestrial Noble Gases and Evolution of the Atmosphere. Rev. Mineral. Geochemistry 47, 411–480. https://doi.org/10.2138/rmg.2002.47.11

Porcelli, D., Wasserburg, G.J., 1995. Mass transfer of helium, neon, argon, krypton, and xenon through a steady-state upper mantle. Geochim. Cosmochim. Acta 59, 4921–4937.

Potter, R.W., Clynne, M.A., 1978. The solubility of the noble gases He, Ne, Ar, Kr, and Xe in water up to the critical point. J. Solution Chem. 7, 837–844. https://doi.org/10.1007/BF00650811

Ranero, C.R., Morgan, J.P., McIntosh, K., Reichert, C., 2003. Bending-related faulting and mantle serpentinization at the Middle America trench. Nature 425, 367–373.

Rüpke, L.H., Morgan, J.P., Hort, M., Connolly, J.A.D., 2004. Serpentine and the subduction zone water cycle. Earth Planet. Sci. Lett. 223, 17–34. https://doi.org/10.1016/j.epsl.2004.04.018

Sarda, P., Graham, D., 1990. Mid-ocean ridge popping rocks: implications for degassing at ridge crests. Earth Planet. Sci. Lett. 97, 268–289. https://doi.org/10.1016/0012-821X(90)90047-2

Sawai, M., Katayama, I., Hamada, A., Maeda, M., Nakashima, S., 2013. Dehydration kinetics of

antigorite using in situ high-temperature infrared microspectroscopy. Phys. Chem. Miner. 40, 319–330. https://doi.org/10.1007/s00269-013-0573-9

Shimizu, K., Saal, A.E., Myers, C.E., Nagle, A.N., Hauri, E.H., Forsyth, D.W., Kamenetsky, V.S., Niu, Y., 2016. Two-component mantle melting-mixing model for the generation of mid-ocean ridge basalts: Implications for the volatile content of the Pacific upper mantle. Geochim. Cosmochim. Acta 176, 44–80. https://doi.org/10.1016/j.gca.2015.10.033

Smye, A.J., Jackson, C.R.M., Konrad-schmolke, M., Hesse, M.A., Parman, S.W., Shuster, D.L., Ballentine, C.J., 2017. Noble gases recycled into the mantle through cold subduction zones. Earth Planet. Sci. Lett. 471, 65–73. https://doi.org/10.1016/j.epsl.2017.04.046

Staudacher, T., Allègre, C.J., 1988. Recycling of oceanic crust and sediments: the noble gas subduction barrier. Earth Planet. Sci. Lett. 89, 173–183. https://doi.org/10.1016/0012-821X(88)90170-7

Sumino, H., Burgess, R., Mizukami, T., Wallis, S.R., Holland, G., Ballentine, C.J., 2010. Seawater-derived noble gases and halogens preserved in exhumed mantle wedge peridotite. Earth Planet. Sci. Lett. 294, 163–172. https://doi.org/10.1016/j.epsl.2010.03.029

Torgersen, T., 1989. Terrestrial helium degassing fluxes and the atmospheric helium budget : Implications with respect to the degassing processes of continental crust 79, 1–14.

Trieloff, M., Kunz, J., Clague, D.A., Harrison, D., Allègre, C.J., 2000. The Nature of Pristine Noble Gases in Mantle Plumes. Science (80-.). 288, 1036–1038. https://doi.org/10.1126/science.288.5468.1036

Williams, C.D., Mukhopadhyay, S., 2018. Capture of nebular gases during Earth's accretion is

preserved in deep-mantle neon. Nature. https://doi.org/10.1038/s41586-018-0771-1

Zaikowski, A., Schaeffer, O.A., 1979. Solubility of noble gases in serpentine: Implications for meteoritic noble gas abundances. Earth Planet. Sci. Lett. 45, 141–154. https://doi.org/10.1016/0012-821X(79)90116-X

Figure 1 Noble gas contents of air, seawater, MORB, and oceanic sediments. No mixture of air and seawater can produce the composition observed for MORB. Ballentine & Holland (2008) suggest that a mixture of sediments with seawater can explain these observations. However, there is significant variability in the noble gas composition of oceanic sediments, and this model does not account for the altered oceanic crust or hydrated lithospheric mantle. Composition of MORB based on "popping rock" 2ΠD43 (Moreira et al., 1998). Compositions of air and seawater from Ozima and Podosek (2002). Sediment data from Matsuda & Nagao (1986) and Staudacher & Allègre (1988).

Figure 2 Data from natural systems representative of sub-seafloor alteration and subsequent dehydration (Kendrick et al., 2011). Serpentinites have high Xe/Kr ratios, seen as a steeper slope extending upwards from seawater, and retain their noble gases during dehydration metamorphism as measured in olivine-enstatite residues of dehydration. Data for antigorites are shown as circles, ol-en residues are squares, early fluids are upright triangles, and final fluids are inverted triangles. The arrow points towards the compositions of Matsuda & Nagao (1986) and reflects the mixing model of Ballentine & Holland (2008). Other data from sources as in Fig. 1.

Figure 3 Reflected light photomicrograph of a representative sample of serpentinite used in these experiments. Samples consist of antigorite with macro- and micro-scale magnetite. Laser ablation pits were placed to avoid magnetite where possible.

Figure 4 Oblique view of an example laser ablation pit as measured by white light interferometry. The flat, outer area is interpolated to produce a pre-ablation surface. This pre-

ablation surface is then subtracted from the measured surface to determine the volume of the laser ablation pit.

Figure 5 Noble gas Henry's constants in serpentinite, calculated from experiments run at 350°C and pressures ranging from 0.15 to 1.13 kbar, plotted against atomic number. Each data point represents an average of multiple laser ablation spots on a single sample of serpentinite. Data shown as squares are from experiments run with He, Ne, and Ar, while circles are from experiments run with Ar, Kr, and Xe. Also shown are previously published solubility data from Jackson et al. (2015) and Zaikowski and Schaeffer (1979). Except for He, the noble gases show an increase in solubility with increasing atomic number. The range of solubilities is attributed to the variable influence of fluid inclusions, surface contaminants, grain- and phase-boundaries in the natural samples. In experiments run with Ar, Kr, and Xe (circles), the lowest values are the most representative of serpentinite, while higher values represent the variable influence of fluid inclusions and contaminants. The dashed line represents our preferred values for Ar, Kr, and Xe fractionation, based on Ar-Kr-Xe experiments (Supplementary methods; figure S1). Error bars are one standard deviation.

Figure 6 Experimentally determined fractionations due to differences in solubility are shown in comparison to data from natural serpentinites (Kendrick et al., 2011). A mixing line is calculated using the initial noble gas composition of seawater—the source of noble gases in serpentinites—multiplied by the experimentally determined relative solubilities of Kr to Ar and Xe to Ar. The mixing line closely matches the data from antigorites measured by Kendrick et al. (2011). The

arrow points towards the compositions of Matsuda & Nagao (1986) and reflects the model of Ballentine & Holland (2008). Data as in Fig. 2.

Figure 7 Noble gas data from Iceland (circles) and Hawaii (squares) are compared to the calculated seawater-serpentinite mixing line. Samples from Iceland trend towards sediments while samples from Hawaii trend along a high Xe/Kr ratio towards serpentinites. Data for Hawaii and Iceland from Trieloff et al. (2000). Air, MORB, seawater, and sediments as in Fig. 2.

Figure 8 Noble gas data from Polynesian OIBs are compared to the calculated seawater-serpentinite mixing line (bold arrow) and measurements of altered oceanic crust (dashed line; Chavrit et al., 2016). EM1 and EM2 OIBs have Kr/Ar and Xe/Ar ratios which are too Xe rich to be a mixture of air, seawater, and MORB, much like EM1 samples from Hawaii (Fig. 7). HIMU OIBs have much higher Kr/Ar and Xe/Ar ratios. The range of HIMU OIBs closely resembles the data from altered oceanic crust. Correlation of noble gases in altered oceanic crust with HIMU OIBs suggests that some component of altered oceanic crust is controlling the noble gas budget of the HIMU source. Data for Polynesian OIBs from Hanyu et al. (1999). Data for altered oceanic crust from Chavrit et al. (2016). Air and seawater as in Figure 2. MORB data from Holland and Ballentine (2006).

Table 1 Noble gas ratios in air, seawater, and MORB

	$^{84}Kr/^{36}Ar$	$^{130}Xe/^{36}Ar$	$^{132}Xe/^{36}Ar$	Source
Air				
	0.0207	0.000113	0.000744	Ozima and Podosek (2002)
Seawater				
Air saturated				
at 0 °C	0.0403	0.000455	0.00301	Ozima and Podosek (2002)
MORB				
Popping Rock	0.0564	0.00103	—	Moreira et al. (1998)
Bravo Dome				
Well Gas[a]	0.0556	0.001045	0.007088	Holland and Ballentine (2006)

a End-member MORB isotope ratios defined based on air-crust-mantle mixing trends by Holland and Ballentine (2006).

Table 2 Experimentally determined Henry's Constants of noble gases in serpentinite (in 10^{-9} mol $\cdot$ g^{-1} $\cdot$ bar^{-1}). Error represents one standard deviation of the uncertainty-weighted mean. For the results of individual experiments, please see the online supplementary materials.

^{4}He	1.78	± 0.0319
^{22}Ne	0.135	± 0.00831
^{40}Ar	0.295	± 0.0129
^{84}Kr	1.25	± 0.455
^{130}Xe	3.29	± 1.18

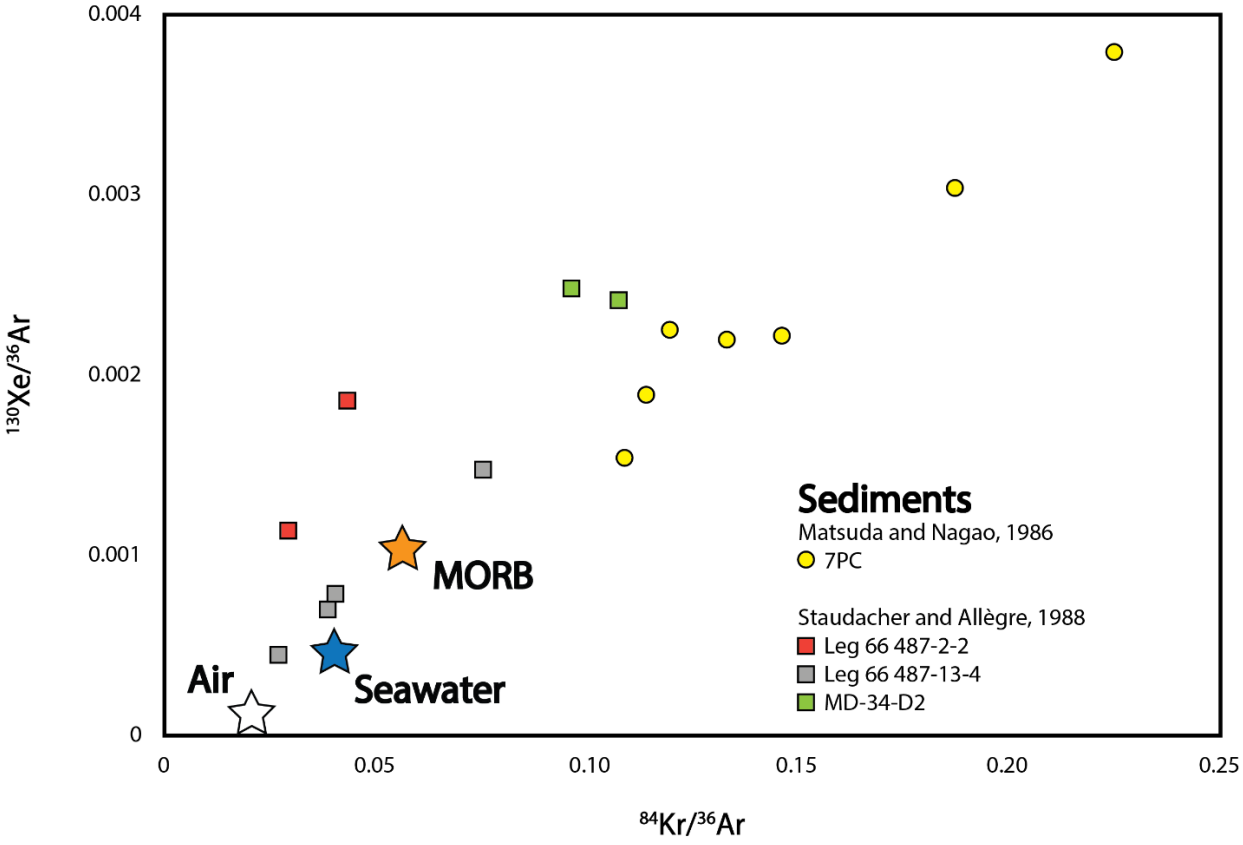
0.004
0.003
0.002
0.001
0
$^{130}Xe/^{36}Ar$
0
0.05
0.10
0.15
0.20
0.25
$^{84}Kr/^{36}Ar$
Sediments
Matsuda and Nagao, 1986
7PC
Staudacher and Allègre, 1988
Leg 66 487-2-2
Leg 66 487-13-4
MD-34-D2
MORB
Seawater
Air

Figure 1

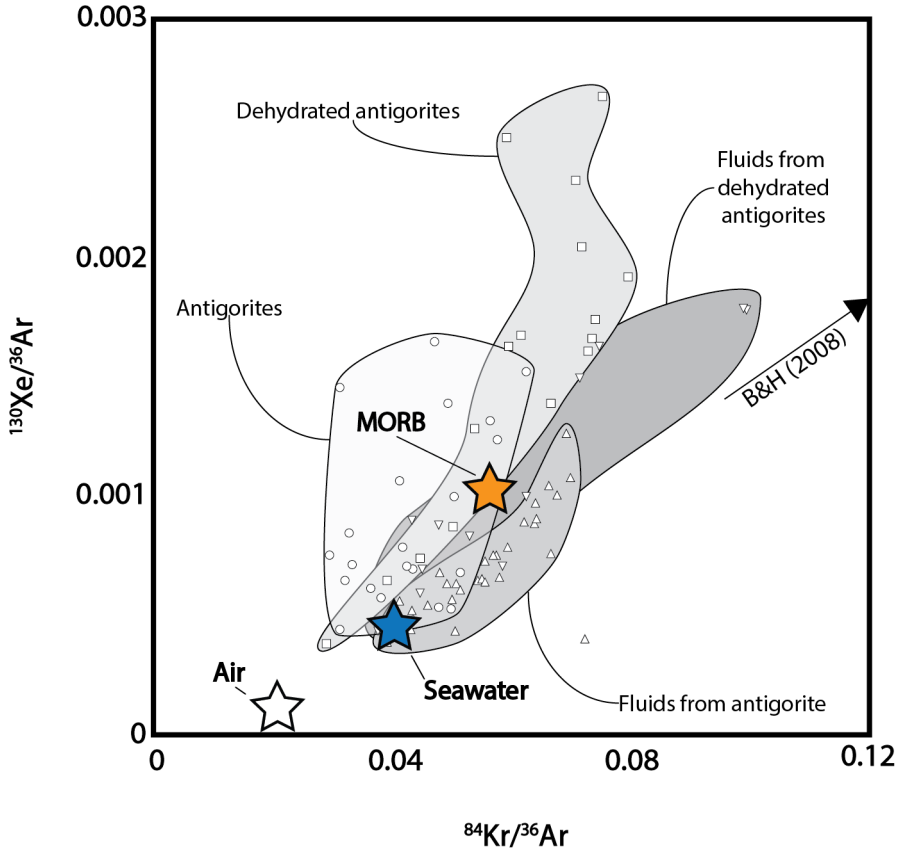
0.003
0.002
0.001
0
0
0.04
0.08
0.12
$^{130}Xe/^{36}Ar$
$^{84}Kr/^{36}Ar$
Dehydrated antigorites
Fluids from dehydrated antigorites
Antigorites
B&H (2008)
MORB
Air
Seawater
Fluids from antigorite

Figure 2

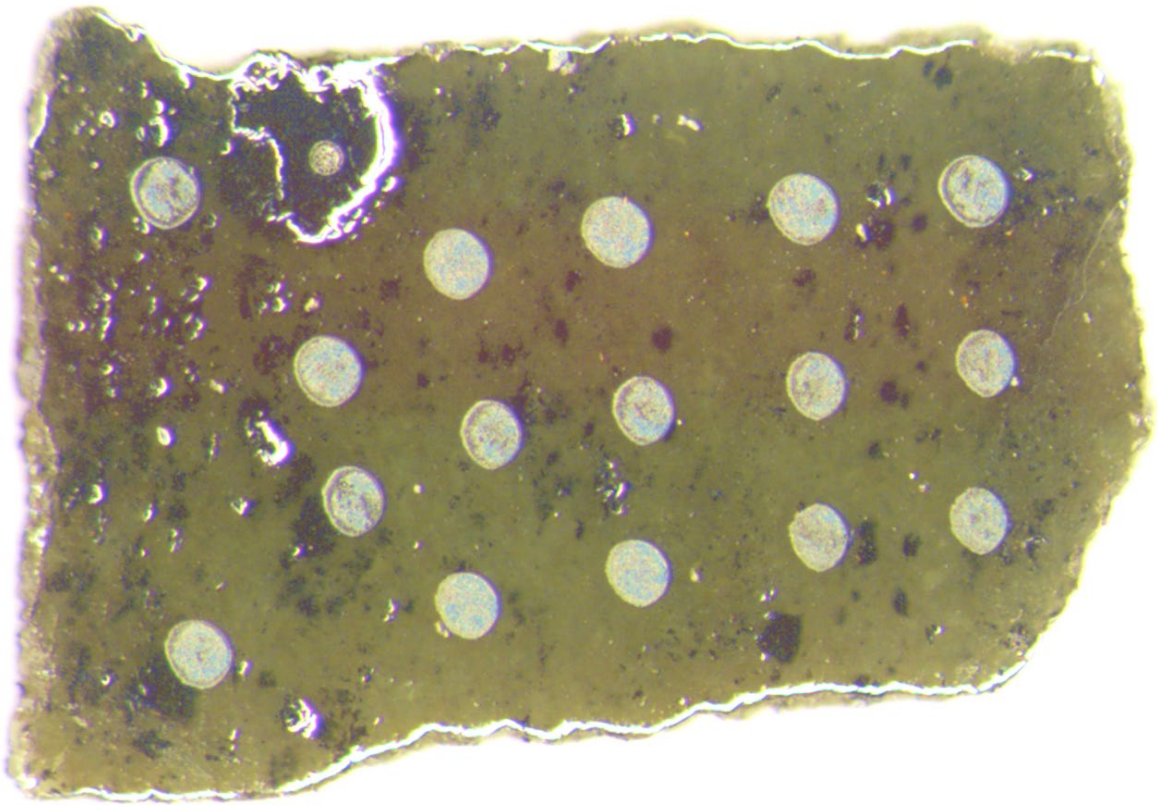

Figure 3

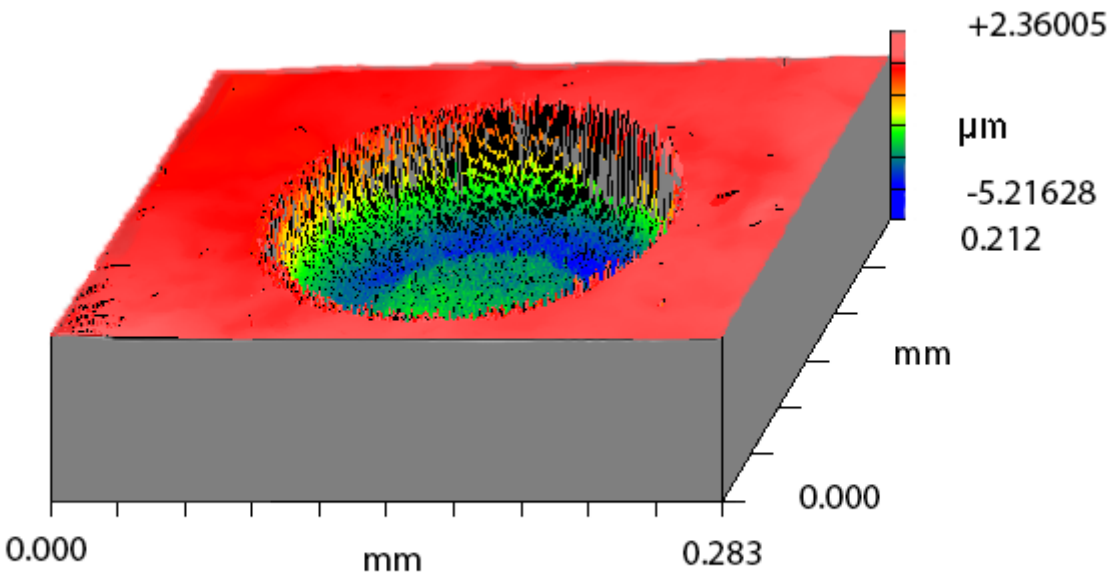

Figure 4

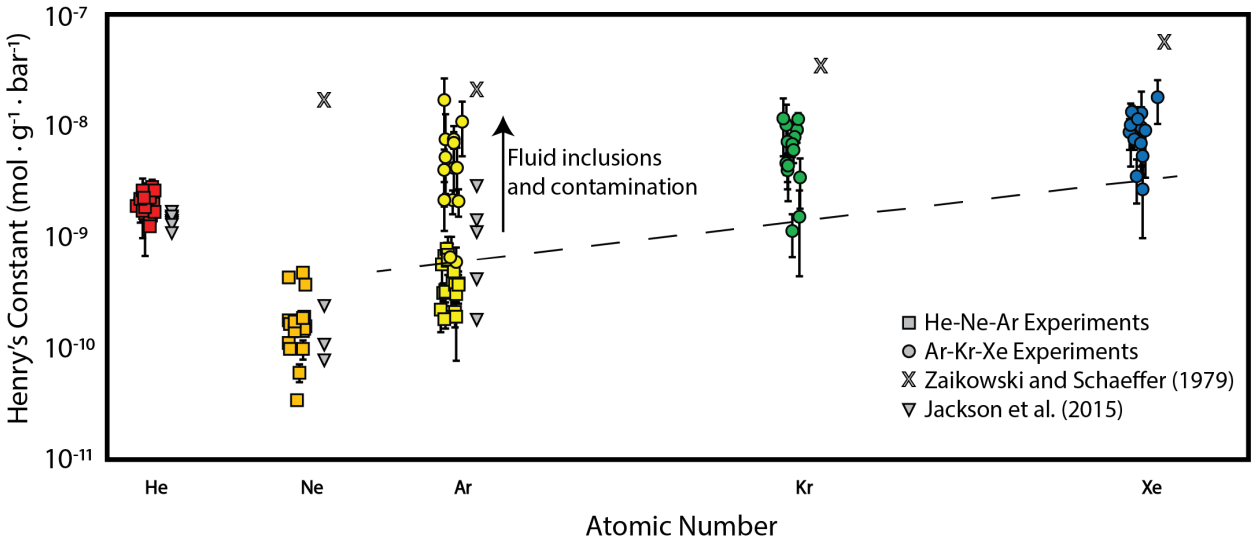
Henry's Constant (mol · g-1 · bar-1)
10-7
10-8
10-9
10-10
10-11
Fluid inclusions
and contamination
He-Ne-Ar Experiments
Ar-Kr-Xe Experiments
Zaikowski and Schaeffer (1979)
Jackson et al. (2015)
He
Ne
Ar
Kr
Xe
Atomic Number

Figure 5

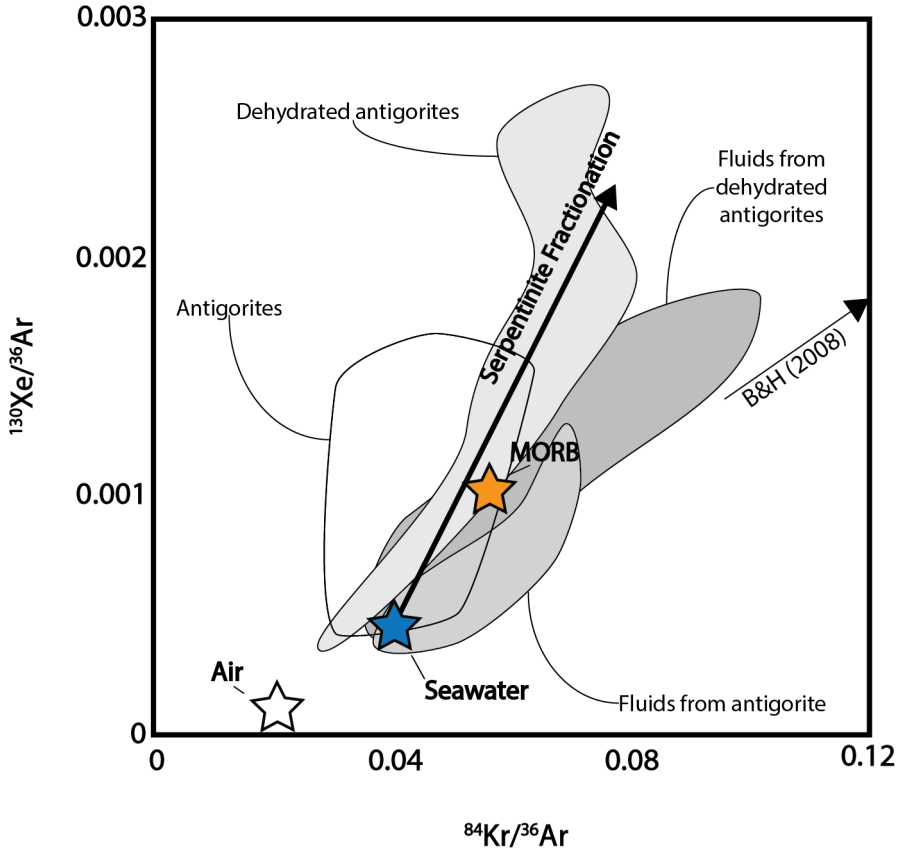
0.003
0.002
0.001
0
0
0.04
0.08
0.12
$^{130}Xe/^{36}Ar$
$^{84}Kr/^{36}Ar$
Dehydrated antigorites
Fluids from dehydrated antigorites
Antigorites
Serpentinite Fractionation
B&H (2008)
MORB
Air
Seawater
Fluids from antigorite

Figure 6

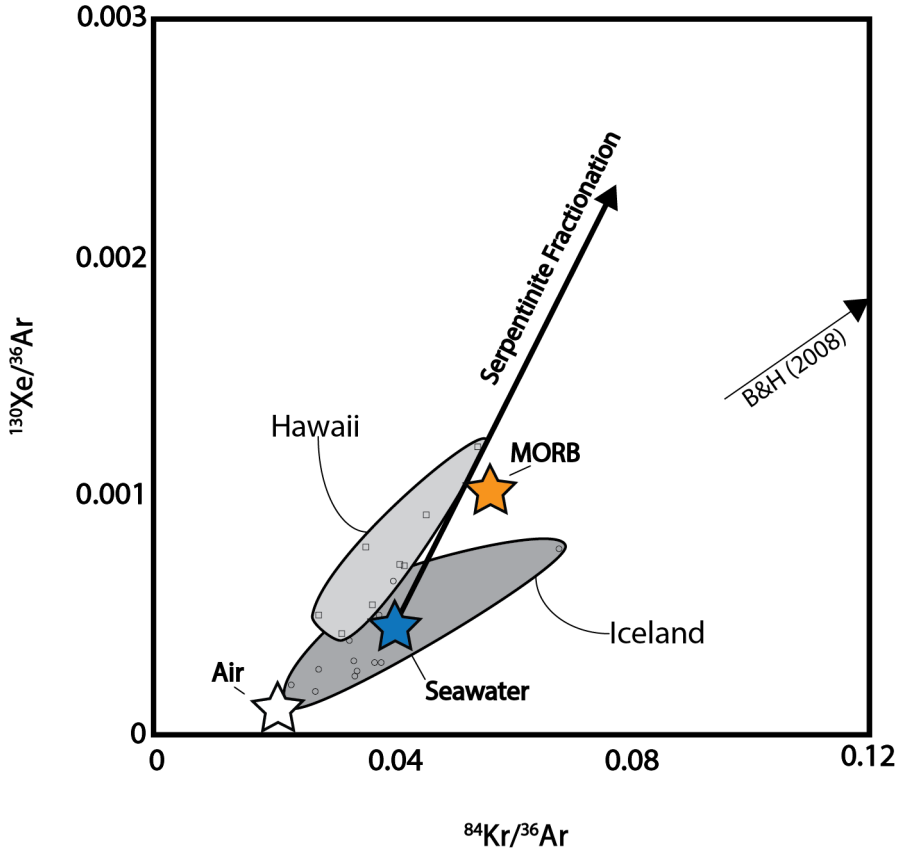
0.003
0.002
0.001
0
$^{130}Xe/^{36}Ar$
Serpentinite Fractionation
B&H (2008)
Hawaii
MORB
Iceland
Air
Seawater
0
0.04
0.08
0.12
$^{84}Kr/^{36}Ar$

Figure 7

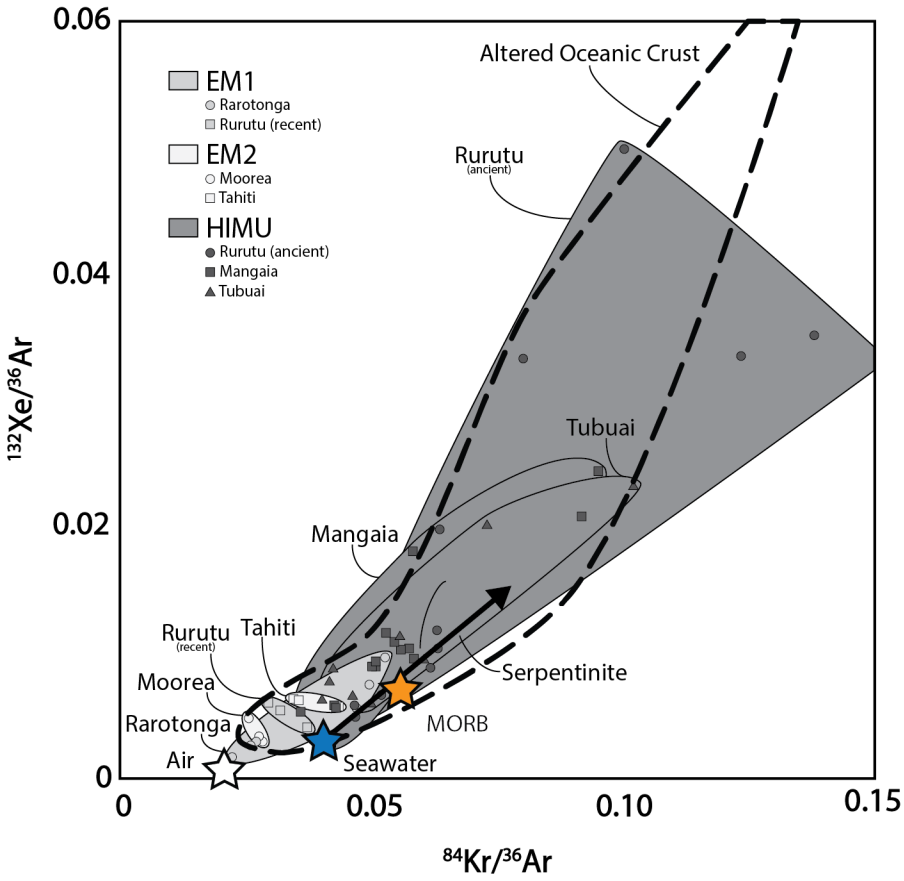
0.06
0.04
0.02
0
0
0.05
0.10
0.15
$^{132}Xe/^{36}Ar$
$^{84}Kr/^{36}Ar$
EM1
Rarotonga
Rurutu (recent)
EM2
Moorea
Tahiti
HIMU
Rurutu (ancient)
Mangaia
Tubuai
Altered Oceanic Crust
Rurutu (ancient)
Tubuai
Mangaia
Rurutu (recent)
Tahiti
Moorea
Rarotonga
Air
Serpentinite
MORB
Seawater

Figure 8

Supplementary Methods

1. Calculation of Solubility

To determine if experimental samples reached equilibrium, depth vs. concentration profiles were calculated. As is observed in these experiments (Fig. S1), a constant concentration with variations in depth is indicative of equilibrium conditions. Similarly, experiments run for different durations do not show a systematic variation indicating that samples are stable under experimental conditions and at equilibrium.

2. Mass Balance

Mass balance calculations for sediments and altered oceanic crust (AOC) were made using the least air-like (i.e. the furthest from air in a $^{84}Kr/^{36}Ar$-$^{130}Xe/^{36}Ar$ plot) and the highest measured concentrations. Sediment values used were Sample Depth 195 cm (Matsuda and Nagao, 1986) while AOC values were from Sample 1256-12R-11 (Chavrit et al., 2016). Concentrations in serpentinite were calculated using experimentally determined Henry's Constants, noble gas solubility in water, and previously reported noble gas concentrations in seawater (Allègre et al., 1987; Ozima and Podosek, 2002; Potter and Clynne, 1978). Serpentinization occurs over a range of temperatures, however, the relative contribution of the three layers was assessed at 300 °C and 235 °C (Ozima and Podosek, 2002; Wenner and Taylor, 1971). While Henry's Constants are assumed to be temperature independent between experimental conditions (350 °C) and the conditions of serpentinization, gas-water partitioning was calculated at each temperature. Lower temperatures favor partitioning of gases into minerals, so the results of calculations at 300 °C have been reported to produce a minimum concentration of gas in serpentinite.

To constrain the relative contribution of the three layers, concentrations were multiplied by density and layer thickness to determine a total amount of noble gas in each layer (Table S2). Sediment density was assessed for the range from 1.7 to 1.96 g/cm^3 while thickness ranged from 1 to 12 km (Sykes, 1996). The density of altered oceanic crust ranges from 2.62 to 2.97 g/cm^3 and thickness varies from 5 to 9 km (Carlson and Herrick, 1990; White et al., 1992). The density of serpentinite used for calculations was 2.61 g/cm^3 and thickness ranged from 3 to 30 km (Barnes and Straub, 2010; Coleman, 1971; Li and Lee, 2006). The full range of these conditions was investigated to determine the relative contribution of each layer, while only one set of conditions was used to calculate fluxes. Fluxes were calculated using 1 km of sediments with a density of 1.7 g/cm^3, 9 km of AOC with a density of 2.97 g/cm^3, and 3 km of serpentinite with a density of 2.61 g/cm^3.

A global index of trench length and orthogonal convergence rate (Hacker, 2008) was used to calculate the total global flux of gas as:

$$Flux = Conc. \cdot Thickness \cdot Length \cdot Orthogonal\ convergence\ rate$$

To compare the total flux to the amount of gas in the Earth, estimates of the concentration of noble gases in the depleted and bulk mantle were used (Marty, 2012). Concentrations were then normalized to the mass of the bulk silicate earth ($4 \cdot 10^{27}$ g). Total concentration in the mantle was then divided by the flux to determine the time scale over which subduction could deliver that much gas.

Supplementary References

Allègre, C.J., Staudacher, T., Sarda, P., 1987. Rare gas systematics: formation of the atmosphere,

evolution and structure of the Earth's mantle. Earth Planet. Sci. Lett. 81, 127–150. https://doi.org/10.1016/0012-821X(87)90151-8

Barnes, J.D., Straub, S.M., 2010. Chorine stable isotope variations in Izu Bonin tephra: Implications for serpentinite subduction. Chem. Geol. 272, 62–74. https://doi.org/10.1016/j.chemgeo.2010.02.005

Carlson, R.L., Herrick, C.N., 1990. Densities and porosities in the oceanic crust and their variations with depth and age. J. Geophys. Res. 95, 9153. https://doi.org/10.1029/JB095iB06p09153

Chavrit, D., Burgess, R., Sumino, H., Teagle, D.A.H., Droop, G., Shimizu, A., Ballentine, C.J., 2016. The contribution of hydrothermally altered ocean crust to the mantle halogen and noble gas cycles. Geochim. Cosmochim. Acta 183, 106–124. https://doi.org/10.1016/j.gca.2016.03.014

Coleman, R.G., 1971. Petrologic and geophysical nature of serpentinites. Bull. Geol. Soc. Am. 82, 897–918. https://doi.org/10.1130/0016-7606(1971)82[897:PAGNOS]2.0.CO;2

Hacker, B.R., 2008. H2O subduction beyond arcs. Geochemistry, Geophys. Geosystems 9. https://doi.org/10.1029/2007GC001707

Kendrick, M.A., Scambelluri, M., Honda, M., Phillips, D., 2011. High abundances of noble gas and chlorine delivered to the mantle by serpentinite subduction. Nat. Geosci. 4, 807–812. https://doi.org/10.1038/ngeo1270

Li, Z.X.A., Lee, C.T.A., 2006. Geochemical investigation of serpentinized oceanic lithospheric mantle in the Feather River Ophiolite, California: Implications for the recycling rate of water by subduction. Chem. Geol. 235, 161–185. https://doi.org/10.1016/j.chemgeo.2006.06.011

Marty, B., 2012. The origins and concentrations of water, carbon, nitrogen and noble gases on Earth. Earth Planet. Sci. Lett. 313–314, 56–66. https://doi.org/10.1016/j.epsl.2011.10.040

Matsuda, J., Nagao, K., 1986. Sediment gas core abundances from eastern in a deep-sea Pacific equatorial. Geochem. J. 20, 71–80.

Ozima, M., Podosek, F.A., 2002. Noble Gas Geochemistry. Cambridge University Press.

Potter, R.W., Clynne, M.A., 1978. The solubility of the noble gases He, Ne, Ar, Kr, and Xe in water up to the critical point. J. Solution Chem. 7, 837–844. https://doi.org/10.1007/BF00650811

Sawai, M., Katayama, I., Hamada, A., Maeda, M., Nakashima, S., 2013. Dehydration kinetics of antigorite using in situ high-temperature infrared microspectroscopy. Phys. Chem. Miner. 40, 319–330. https://doi.org/10.1007/s00269-013-0573-9

Sykes, T.J.S., 1996. A correction for sediment lead upon the ocean floor: Uniform versus varying sediment density estimations - Implications for isostatic correction. Mar. Geol. 133, 35–49. https://doi.org/10.1016/0025-3227(96)00016-3

Wenner, D.B., Taylor, H.P., 1971. Temperatures of serpentinization of ultramafic rocks based on O18/O16 fractionation between coexisting serpentine and magnetite. Contrib. to Mineral. Petrol. 32, 165–185. https://doi.org/10.1007/BF00643332

White, R.S., McKenzie, D., O'Nions, R.K., 1992. Oceanic crustal thickness from seismic measurements and rare earth element inversions. J. Geophys. Res. 97, 19683–19715. https://doi.org/10.1029/92JB01749

Figure S1: Henry's Law plots for He, Ne, and Ar data. Linearity of the trends in He-Ne-Ar experimental data indicates that Henrian behaviour dominates the system. The calculated 95% prediction interval for Ar in the He-Ne-Ar experiments has been used to identify the two experiments which are used for HNG solubility and fractionation calculations. The grey line represents the uncertainty-weighted Ar trend for comparison to the regression and intervals shown.

Figure S2: Demonstration of equilibrium conditions. Plots of pit depth and calculated Henry's constants for the two experiments used to calculate Ar-Kr-Xe fractionation (Experiments CS-JP1-2, blue circles, 27 hours, 800 bars; and CS-JP2-3, orange diamonds, 38 hours, 690 bars). The near horizontal trend of these measurements indicates that samples are at equilibrium.

Figure S3: Concentration of heavy noble gases (ccSTP/unit area) in slab model as a function of layer thickness. Noble gas contents of the sediments, altered oceanic crust (AOC), and natural serpentinite were calculated using the least air-like and most gas-rich analyses from natural systems (Chavrit et al., 2016; Kendrick et al., 2011; Matsuda and Nagao, 1986). Experimental serpentinite concentrations were derived from the results of this study.

Table S1 Composition of serpentinite sample (Sawai et al., 2013)

Oxide	wt%		
SiO_2	40.72	±	0.27
TiO_2	0.03	±	0.01
Al_2O_3	1.73	±	0.24
FeO	6.23	±	0.32
MnO	0.10	±	0.02
Cr_2O_3	0.35	±	0.05
MgO	37.04	±	0.36
CaO	0.01	±	0.00
Na_2O	0.00	±	0.00
K_2O	0.01	±	0.01
NiO	0.19	±	0.07
Total	86.41	±	0.26

Table S2: Parameters used to model noble gas subduction. Gas concentrations represent the least air-like and most gas-rich analyses from natural systems (Chavrit et al., 2016; Kendrick et al., 2011; Matsuda and Nagao, 1986) and the calculations herein.

	^{36}Ar (ccSTP/g)	^{84}Kr (ccSTP/g)	^{130}Xe (ccSTP/g)	Density (g/cm^3)	Thickness (km)
Sediments	1.20E-09	2.70E-10	4.55E-10	1.7-1.95	1-12
Altered Oceanic Crust	1.01E-08	8.59E-10	2.90E-11	2.62-2.97	5-7
Natural Serpentinite	6.71E-08	4.28E-09	1.03E-10	2.61	1-30
Serpentinite (This study)	2.66E-07	2.16E-08	5.08E-10	2.61	1-30

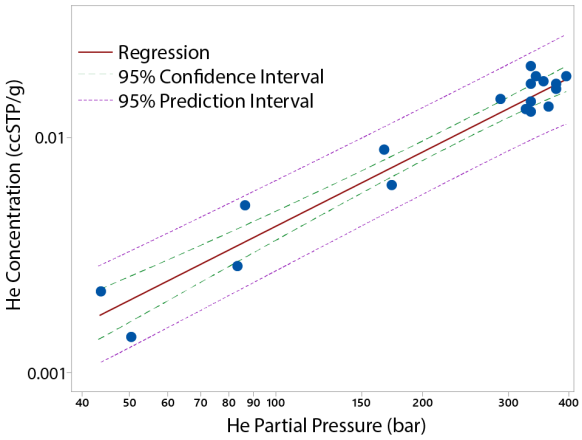
Regression
95% Confidence Interval
95% Prediction Interval
He Concentration (ccSTP/g)
0.01
0.001
40 50 60 70 80 90 100 150 200 300 400
He Partial Pressure (bar)

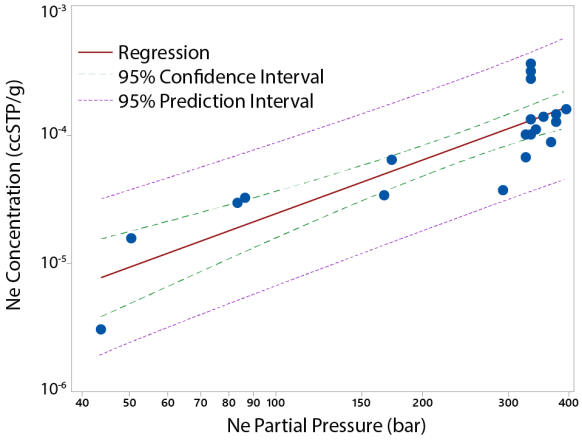
Regression
95% Confidence Interval
95% Prediction Interval
Ne Concentration (ccSTP/g)
10-3
10-4
10-5
10-6
40 50 60 70 80 90 100 150 200 300 400
Ne Partial Pressure (bar)

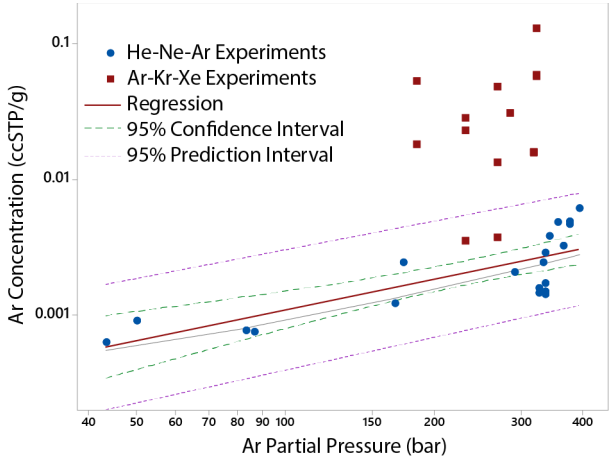
He-Ne-Ar Experiments
Ar-Kr-Xe Experiments
Regression
95% Confidence Interval
95% Prediction Interval
Ar Concentration (ccSTP/g)
0.1
0.01
0.001
40 50 60 70 80 90 100 150 200 300 400
Ar Partial Pressure (bar)

Figure S1

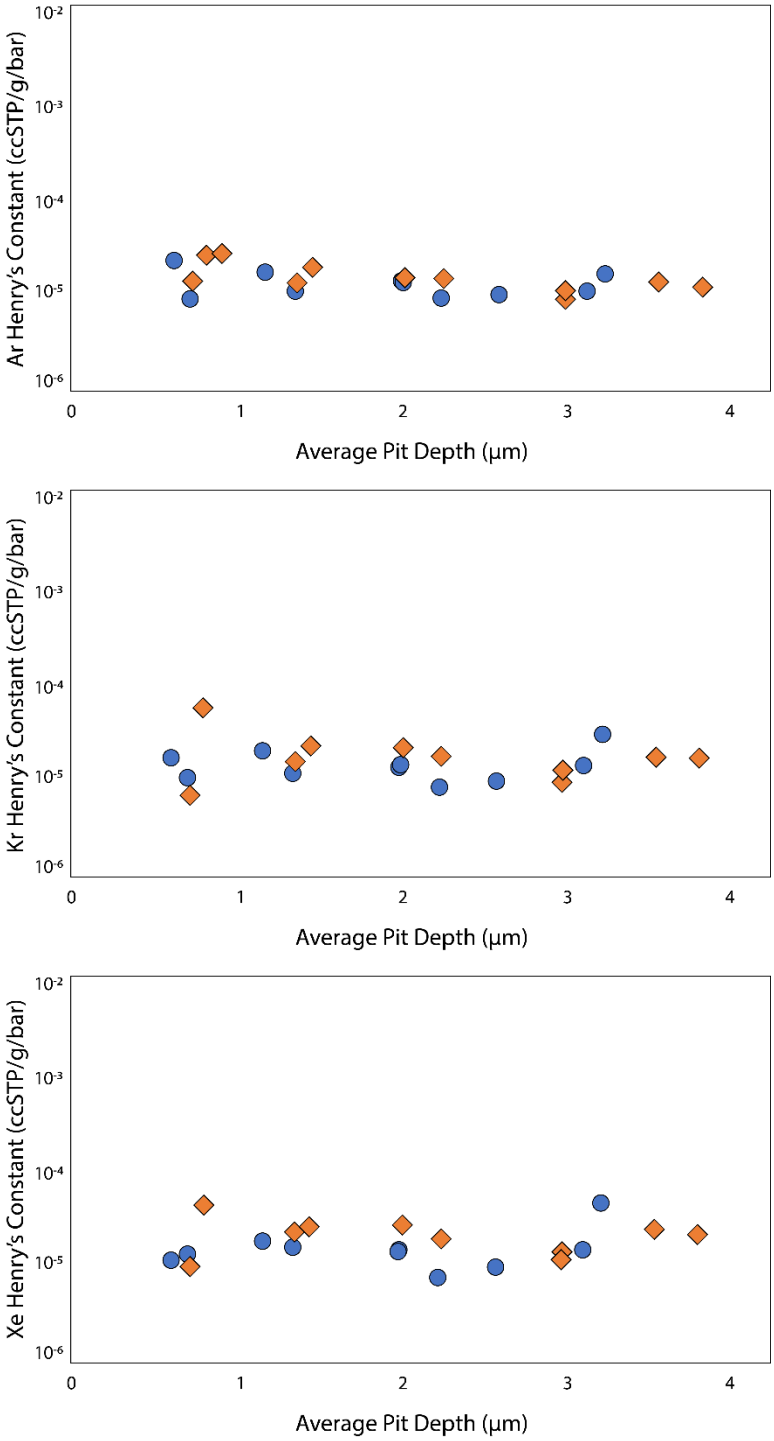
Ar Henry's Constant (ccSTP/g/bar)
Kr Henry's Constant (ccSTP/g/bar)
Xe Henry's Constant (ccSTP/g/bar)
10-2
10-3
10-4
10-5
10-6
0
1
2
3
4
Average Pit Depth (μm)

Figure S2

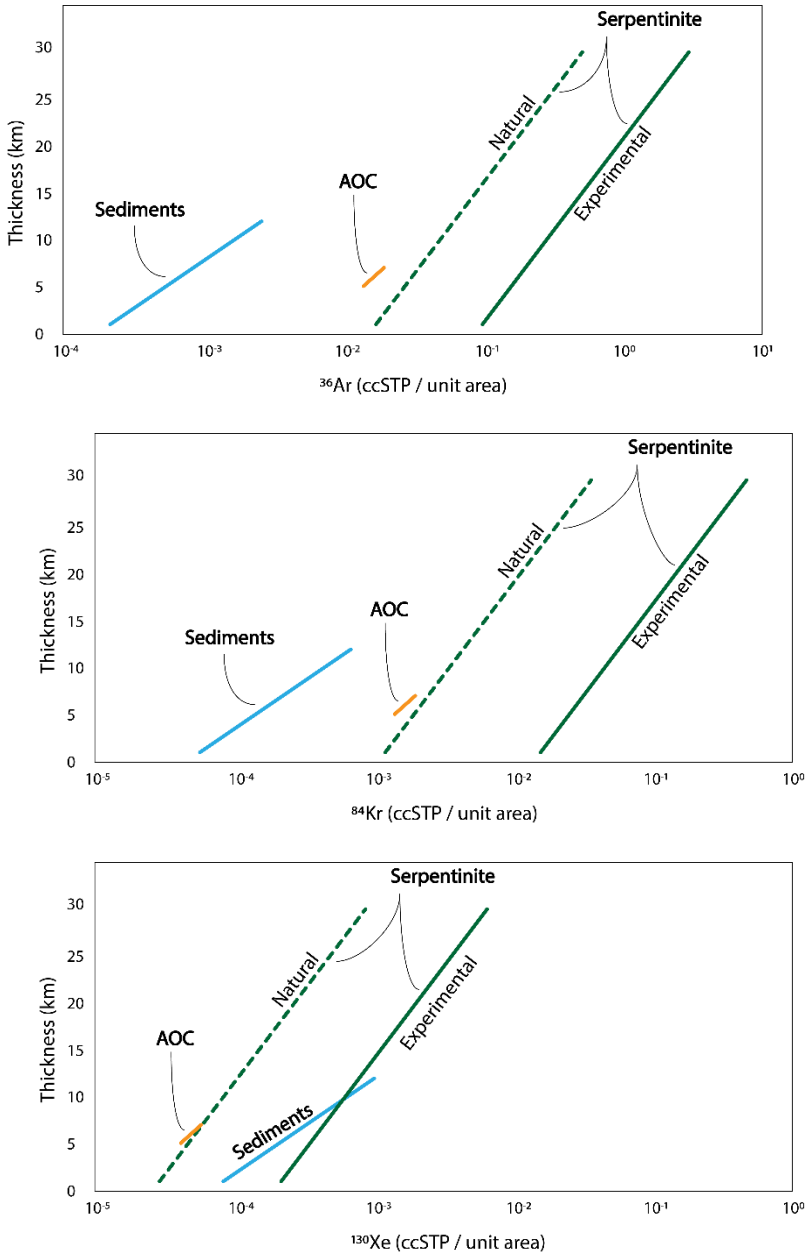
Serpentinite
Natural
Experimental
AOC
Sediments
Thickness (km)
30
25
20
15
10
5
0
10-4
10-3
10-2
10-1
100
101
36Ar (ccSTP / unit area)
Serpentinite
Natural
Experimental
AOC
Sediments
Thickness (km)
30
25
20
15
10
5
0
10-5
10-4
10-3
10-2
10-1
100
84Kr (ccSTP / unit area)
Serpentinite
Natural
Experimental
AOC
Sediments
Thickness (km)
30
25
20
15
10
5
0
10-5
10-4
10-3
10-2
10-1
100
130Xe (ccSTP / unit area)

Figure S3

CHAPTER TWO: TRACING MANTLE REGASSING AND THE ONSET OF SUBDUCTION USING OBSERVATIONS OF H, N, AND XE

John A. Krantz[a], Peter H. Barry[b], Stephen W. Parman[a]

a Department of Earth, Environmental, and Planetary Sciences,

Brown University, Providence, RI

b Woods Hole Oceanographic Institution, Woods Hole, MA

Abstract

The distribution of volatiles between the surface and interior of the Earth is largely controlled by two processes: degassing at mid-ocean ridges and regassing in subduction zones. Major volatiles like water and carbon dioxide are challenging to track through geological processes as they readily react with other materials. More inert volatiles, like nitrogen and xenon, provide constraints on the physical processes experienced by volatiles while negating the chemical reactions. Thus, it is possible to use relatively rare volatiles to trace more important major volatiles.

There is abundant evidence for the inclusion of atmospheric nitrogen and noble gases within the source of both MORBs and OIBs (Barry and Hilton, 2016; Holland and Ballentine, 2006; Parai and Mukhopadhyay, 2018). The fraction of the nitrogen and xenon in the mantle today which originated in the atmosphere (84-92% and 73-87%, respectively) is very similar despite their different chemical behaviours. Since N and Xe exhibit similar behaviour despite their different chemical behaviour, the larger processes controlling their recycling must be broadly related (Barry and Hilton, 2016; Jackson *et al.*, 2015; Krantz *et al.*, 2019). This similarity may be the result of broader physical processes which control the recycling of volatiles, like subduction and mantle temperature. Herein, we present the results of a new model which shows that coupling between the N and Xe systems produces results consistent with the isotopic ratios and concentration of both N and Xe in the modern mantle.

The results of our model constrain the degree to which the mantle has been processed (8-8.5 reservoirs processed). The constraints from the coupled N-Xe system are also used to model the evolution of H. The timing of the mantle's transition from degassing to regassing is calculated for

each volatile system studied. These results show that volatile input to the mantle increased during the Archean, overtaking outgassing 3.1 Ga, 2.5 Ga, and 1.8 Ga for H, N, and Xe, respectively. The timing of the transition to a net regassing regime is consistent with models of the onset of subduction (Keller and Schoene, 2012; Shirey and Richardson, 2011; Tang *et al.*, 2018). Measuring ancient mantle volatile isotopes would both test the results of this model and provide valuable constraints on the interactions between Earth's mantle and surface reservoirs.

Introduction

The distribution of volatiles between the modern mantle and atmosphere is the result of the combined effects of retention of primordial components, outgassing of mantle reservoirs during melting, and recycling via subduction from surface reservoirs. Over billions of years, this volatile exchange has influenced mantle viscosity, cooling, and surface conditions (Crowley *et al.*, 2011; Korenaga, 2011; Mei and Kohlstedt, 2000; Nakagawa *et al.*, 2015; Sandu *et al.*, 2011). Due to its importance, Earth's volatile history has been extensively studied, however no clear consensus has yet formed as it is difficult to trace H_2O and most other major volatiles due to their chemical reactivity (Abe *et al.*, 2000; Dauphas, 2000; Drake, 2005; Marty, 2012; Marty and Yokochi, 2019; Morbidelli *et al.*, 2000; Robert, 2003).

Estimates of volatile concentrations and isotopic ratios suggest that as much as 90% of Earth's water and 97% of its carbon are in the mantle (Marty, 2012). These chemically reactive volatiles, as well as nitrogen, are primarily stored in the modern mantle, whereas the more inert noble gases are primarily in the atmosphere. Nitrogen is essentially inert as molecular N_2, but other forms are reactive and the speciation depends on a variety of factors including N concentration, oxygen

fugacity, pH, pressure and temperature (Mikhail and Sverjensky, 2014). The distribution of N between the mantle and atmosphere thus reflects the time-integrated effects of these factors.

The abundance of these volatiles is largely in line with the contribution of 2 % of Earth's mass coming CC meteorites. The cause of their distribution is, however, debated, with two major theories having been proposed: under more reducing conditions, C, H_2O, and N could be sequestered in the mantle during outgassing (Kadik *et al.*, 2011), or, alternatively, these volatiles were preferentially recycled into the mantle via subduction (Marty, 2012). Recent work has identified recycled atmospheric gases in the mantle and strongly favours the latter hypothesis (e.g., Barry and Hilton, 2016; Holland and Ballentine, 2006; Parai and Mukhopadhyay, 2015; Williams and Mukhopadhyay, 2018).

The nitrogen and xenon isotopic systems have been used to develop constraints on the history of mantle outgassing and regassing in order to improve our understanding of mantle convection and plate tectonics (Barry and Hilton, 2016; Parai and Mukhopadhyay, 2018). Models of the distribution and flux of N predict that the convecting mantle (MORB source) represents a mixture of primordial and recycled components, and that substantial regassing of N likely began 2.6 Ga (Barry and Hilton, 2016; Cartigny and Marty, 2013). Likewise, a detailed study of Xe isotopes shows that Earth's mantle received Xe from at least two distinct cosmochemical sources and substantial recycling of atmospheric Xe did not occur prior to 2.5 Ga (Caracausi *et al.*, 2016; Parai and Mukhopadhyay, 2018). Furthermore, the recycling efficiency (the fraction which remains in the mantle after arc magma generation) of N is similar to that of the heavy noble gases: 84-92% and 73-87%, respectively (Barry and Hilton, 2016; Holland and Ballentine, 2006; Parai and Mukhopadhyay, 2012). This similarity in recycling efficiency is unlikely as the two

elements are recycled via fundamentally different mechanisms: N is biologically fixed as NH_4^+ is bound in recycled sediments and crust, whereas the heavy noble gases are instead weakly held within hydrous silicates and pore fluids (Holland and Ballentine, 2006; Jackson *et al.*, 2015; Krantz *et al.*, 2019).

In an effort to understand the remarkably similar history of N and Xe, we develop a model for the evolution of, and exchange of volatiles between, the mantle and surface reservoirs over the lifetime of the Earth. As there is evidence of a primordial origin for, and a clear distinction between, the modern atmosphere and mantle for both N and Xe this model allows for investigation of the evolution of Earth's volatile reservoirs. By combining previously identified constraints from N and Xe, we are able to better understand the broader physical processes which control volatile recycling. Of particular interest, subduction and mantle temperature are expected to be the two primary controls on the extent and timing of recycling.

In this framework, the time at which volatiles begin to be returned to the mantle is likely directly tied to the onset of modern subduction. During the Archean, continental crust was forming, suggesting that some earlier form of subduction was taking place. However, this crust transitioned, relatively rapidly, towards what we see today between 3.0 and 2.5 Ga (Dhuime *et al.*, 2015; Keller and Schoene, 2012; Tang *et al.*, 2018). At the same time, diamonds with eclogitic inclusions begin to appear, most likely as the result of fluids related to subduction (Shirey and Richardson, 2011). Together, these changes, suggest that plate tectonics and subduction as we know it began roughly 2.5 to 3.0 Ga. This hypothesis, is, however, contentious. The existence of zircons as old as 4.4 Ga has been interpreted by other authors to be the result of subduction processes at the time (e.g., Wilde *et al.*, 2001). Conversely, the absence of blueschist

facies rocks prior to 1.0 Ga has been interpreted by some as evidence that modern subduction began relatively recently (e.g., Stern, 2005) Consequently, we expect to find a major shift in volatile cycling at that time.

Methods

We use a forward model with a time-step of 1000 yrs to track stable isotopes during volatile exchange between the atmosphere and mantle based on previous work by Parai and Mukhopadhyay (2018). Our model is applicable to systems which meet the following requirements: the mantle component initially has a chondritic composition; the surface reservoir is isotopically distinct and known through time; the modern mantle is distinguishable from the modern surface reservoir; and the modern mantle's concentration and isotopic composition are known. The surface reservoir's isotopic character is defined by data from Archean fluid inclusions: Archean N had the same $\delta^{15}N$ as the modern atmosphere while $\delta^{128}Xe$ decreases from an initial value of 97‰ to 0‰ by 2 Ga (Avice *et al.*, 2017; Marty *et al.*, 2013). The mantle's initial volatile inventory was defined based on the addition of average carbonaceous chondrites (AVCC) totalling 1% of the mass of the Earth to a reservoir representing 90% of the mantle (Marty, 2012; Owen *et al.*, 2001; Pepin, 2000; Porcelli *et al.*, 2002; Sephton *et al.*, 2003). While the concentration of volatiles in the mantle is modelled through time, the atmosphere is assumed to be an infinite reservoir.

We investigate two further volatile systems within the parameter space identified by the N-Xe system: neon and hydrogen. The Ne system was modelled using the ^{20}Ne and ^{22}Ne concentrations and ratios of AVCC and an atmosphere matching the modern (Marty, 2012; Williams and Mukhopadhyay, 2018). For models of H, the initial D/H ratio of both the mantle and surface

reservoir are based on the extreme primordial end-member of -870‰ (Marty and Yokochi, 2019). From this initial composition, the surface reservoir is fractionated by hydrodynamic escape, reaching the modern value after 3.5 Gyr (Genda and Ikoma, 2008). While this is likely more depleted than the actual initial end-member, the nature of our model is such that a less depleted initial composition will produce similar evolution paths at proportionately lower δD values.

To constrain the timing and intensity of regassing, the concentration of volatiles being recycled is modelled as an increasing and sigmoidal function (Fig. 1):

$$V_r(t) = \frac{V_r^m}{1 + e^{-\alpha(t-\beta)}}$$

Where V_r^m is the maximum amount of the volatile (V) being recycled (i.e. V_r at t = ∞), α is the growth rate, β is the inflection point, and t is the time from Earth formation. At each time step, a volume of mantle is fully degassed, and the same volume is added into the mantle with volatile contents defined by Eq. 1. The volume of mantle processed at each step is controlled by an exponentially decreasing mantle processing rate (η) which has been pinned to the modern mid-ocean ridge processing rate:

$$Q(t) = Q_p \, e^{\eta(\mathrm{T}-\mathrm{t})}$$

Where Q(t) is the mass of mantle being processed at time t, Q_p is the present-day mantle processing rate, T is the age of the Earth (4.568 Gyr), and η is a free parameter controlling the number of mantle reservoirs processed (for additional details of this methodology, see Parai and Mukhopadhyay, 2018). At each time-step, the volume of mantle from Eq. 2 is fully degassed while the amount of each volatile being added to the mantle reservoir is the product of the concentration in recycled material (Eq. 1) and the mantle processing rate (Eq. 2).

Values of V_r^m, α, β, and η were initially explored using a rough grid search to identify the range of successful conditions for each volatile independently (Supplementary Table 1). To be considered a successful run, the model was required to reproduce the modern mantle's concentration and isotopic composition. Specifically, the isotopic ratios $\delta^{15}N$, $\delta^{128}Xe$, δD, and $^{20}Ne/^{22}Ne$ of -5±2, 10±3, -60±5, and 12.5±0.5, respectively, and concentrations of ^{14}N in the range $1.3 \times 10^{16} – 1.8 \times 10^{18}$, ^{130}Xe in the range $4.3–9.2 \times 10^5$, H in the range $5.3 \times 10^{18} – 6.3 \times 10^{19}$, and Ne in the range $1.7 \times 10^9 – 6.0 \times 10^9$ (Cartigny and Marty, 2013; Marty, 2012; Parai and Mukhopadhyay, 2018). Subsequent models were run using a Monte Carlo method with uniform probability for each variable within the range which overlapped for N and Xe. To couple the N and Xe systems, values of α, β, and η were the same for both systems while the maximum concentrations of N and Xe in recycled material were varied independently. In order to thoroughly sample this space, on the order of 10^{10} instances of the model were run.

In the parameter space identified by the coupled N-Xe system, models run with H, N and Xe produce systems which are successful for either N and Xe, H and N, or H and Xe. It is, perhaps, unsurprising that these three enormously different volatiles do not behave in exactly the same manner, however, the success of model runs for each possible combination of two volatiles indicates that their behaviour is similar. Based on this similarity, we model the H-N-Xe system using a less coupled system. In this less coupled model, the mantle processing rate is fixed for all three systems, while each volatile has a distinct inflection point, growth rate, and maximum recycling concentration. The mantle processing rates used are those identified from the coupled N-Xe system (8-8.5 reservoir volumes processed), while the other variables are explored through the entire range of plausible values.

Results

The coupled N-Xe system is successful for a broad range of growth rates, inflection points, and recycled concentrations (Supplementary Figures 1-3). However, only a narrow range of mantle processing rates—between 8 and 8.5 reservoir volumes processed—are consistent with the constraints from the modern mantle for both volatile systems (Supplementary Figure 4). In this narrow range of mantle processing rates, the history of mantle Xe is tightly constrained against time due to the changing atmospheric component (Fig. 2a). In contrast, the surface reservoir of N has remained isotopically constant since the Archean and N provides tighter constraints on the total extent of mantle degassing and regassing (Fig. 2b) (Johnson and Goldblatt, 2015; Marty, 2012).

As a result of the two systems' different sensitivities to the timing and extent of volatile recycling, when looked at as a coupled system, there is a narrow range of solutions that fit both systems (Fig. 2c). During the first 2 Gyr, there is little change in either $\delta^{15}N$ or $\delta^{128}Xe$, as expected since all inflection points for recycling sigmoids are greater than 1.75 Gyr (i.e. more recent than 2.8 Ga), with little to no constraints on growth rate. After that point, however, there is a rapid change towards modern air along a very narrow path defined by mantle processing rates between 8 and 8.5 reservoir volumes processed. The consistency of the mantle's N-Xe evolution path over the full range of successful model runs indicates that this is a robust result of coupling between the two systems. Of the roughly 10^{10} H-N-Xe model runs, 629 were successful and the distribution of variables producing successful runs is shown in Supplementary Figures 5-8. The loosened constraints for H-N-Xe models produce results for N and Xe which are similar to the initial coupled models and a relatively narrow field of mantle δD values with relatively low growth rates and inflection points greater than 2.5 Gyr (Fig. 4a).

For Ne, our model does not produce matching concentrations and isotopic ratios for the modern mantle (i.e., MORB) for any combination of parameters which produce successful N-Xe models. Successful models for only Ne require drastically lower mantle processing rates, and thus less degassing of the mantle. We suggest that this is a consequence of the assumptions underlying the model. Specifically, this model is designed to explore systems in which the dominant factor controlling mantle volatiles is the degassing/regassing exchange with the surface. If, for example, Ne is being added to the MORB source via another pathway (e.g., release from the plume source or core), a more complex model would be required to accommodate that exchange. Other factors may also account for the lack of successful Ne-N-Xe runs including the possibility that the initial mantle, as a whole, did not consist of AVCC Ne.

Discussion

The balance of mantle degassing and regassing at each time-step is calculated, and for all successful model runs, the transition from net mantle degassing to regassing occurs, at the earliest, 3.1 Ga for H, 2.5 Ga for N, and 1.8 Ga for Xe (Fig. 3). The difference in timing reflects the combined effects of concentrations in the mantle and the concentration in recycled material, both of which vary for each volatile system. The progressive shift to younger ages for less reactive volatiles is an emergent result (i.e. not prescribed by any of the model parameters) and provides strong evidence for the robustness of the model.

For the fully coupled N-Xe model, two families of solutions are produced by the model: those which reach a maximum regassing flux (red lines in Fig. 3) and those which show gradual, monotonic increases (black lines in Fig. 3). These two types of solutions predict either that

regassing peaked within the last 2 Gyr and is now approaching steady-state or that the modern flux of volatiles to the mantle is greater than it has been in the past and it will continue to increase. A continued increase in regassing is consistent with previous work which identified that lower temperatures in subduction zones increase the likelihood of a given volatile reaching the mantle (Smye *et al.*, 2017). At this time, it is not clear what physical processes may be represented by the models with peaks.

As with the coupled N-Xe model solutions, the model produces two families of solutions to the for net H flux: those which peak roughly 2 Ga and those which monotonically increase. The physical implication of the models in which net flux peaks near 2 Ga would most likely be related to the rapid onset of modern, hydrous subduction. The age of these peaks, however, does not align with most evidence for the onset of subduction based on lithophile elements (e.g., Dhuime *et al.*, 2015; Keller and Schoene, 2012; Shirey and Richardson, 2011; Stern, 2005; Tang *et al.*, 2018; Wilde *et al.*, 2001). As such, we suggest that they instead represent a "critical temperature" below which subducted H was retained in the mantle. Models in which the H flux gradually increases may, instead, represent a gradual, thermal change which increases the stability of subducting, hydrous phase (e.g., secular cooling). If the monotonically increasing family of solutions is true, and subduction began 2.5 to 3.5 Ga, then the onset of subduction must not have had a dramatic effect on the net flux of H.

While our model is not able to distinguish between the two families of solutions, it is sensitive to the addition of any new constraints from natural samples. Measurement of the mantle's Xe composition within the last 2 Gyr, for example, would drastically narrow the possible evolution paths for both Xe and N. Measurements of both $\delta^{15}N$ and $\delta^{128}Xe$ in the same sample would serve

to validate our model and further narrow the possible evolution path of N, Xe, and any other volatiles which can be shown to exhibit similar behaviour (Fig. 2).

For all successful model runs, inflection points are at times greater than 2 Gyr (i.e., <2.5 Ga) and net regassing begins roughly 2 to 3 Ga. Specifically, in the case of H, net regassing begins between 2.5 and 3.1 Ga. Hydrogen, being the most reactive of the studied volatiles, represents the element most likely to be retained by a subducting slab, whereas the progressively less reactive elements may require a colder subduction zone. Since any early, subducted material was almost certainly hydrous, this clearly suggests that subduction began at least 2.5 Ga. This is consistent with evidence from Archean diamond inclusions, crustal composition, and statistical geochemistry which indicates that plate tectonics and subduction as we see them today began 2.5 to 3.0 Ga (Keller and Schoene, 2012; Shirey and Richardson, 2011; Tang *et al.*, 2018).

Conclusions

Our model results show that coupling between the N and Xe systems is possible and produces results consistent with constraints on the isotopic ratios and concentration of both N and Xe. The combined N-Xe model places strong constraints on the history of volatile exchange between the mantle and surface. While N is incorporated in oceanic sediments as NH_4^+ and Xe is weakly bound in silicate ring sites, the similarity of their behaviour clearly indicates that their recycling is controlled by external physical parameters: the temperature and rate of subduction.

Our model further constrains the degree to which the mantle has been processed via melting (8-8.5 reservoirs) and these results produce a very narrow field in $\delta^{15}N$-$\delta^{128}Xe$ space. The timing of the mantle's transition from degassing to regassing for each volatile system has been identified:

3.1 Ga, 2.5 Ga and 1.8 Ga for H, N, and Xe, respectively. The overlap of the beginning of mantle regassing for the most reactive volatiles (H and N) with the onset of subduction suggests that the onset of subduction at this time directly led to the recycling of volatiles to the mantle.

References

Abe, Y., Ohtani, E., Okuchi, T., Righter, K., Drake, M.J. (2000) Water in the Early Earth. In: Canup, R.M., Righter, K. (eds) *Origin of the Earth and Moon*. University of Arizona Press, Tucson, 413–433.

Avice, G., Marty, B., Burgess, R. (2017) The origin and degassing history of the Earth's atmosphere revealed by Archean xenon. *Nature Communications*. Nature Publishing Group 8, 1–9.

Barry, P.H., Hilton, D.R. (2016) Release of subducted sedimentary nitrogen throughout Earth's mantle. *Geochemical Perspectives Letters* 148–159.

Caracausi, A., Avice, G., Burnard, P.G., Füri, E., Marty, B. (2016) Chondritic xenon in the Earth's mantle. *Nature*. Nature Publishing Group 533, 82–5.

Cartigny, P., Marty, B. (2013) Nitrogen isotopes and mantle geodynamics: The emergence of life and the atmosphere-crust-mantle connection. *Elements* 9, 359–366.

Crowley, J.W., Gérault, M., O'Connell, R.J. (2011) On the relative influence of heat and water transport on planetary dynamics. *Earth and Planetary Science Letters*. Elsevier B.V. 310, 380–388.

Dauphas, N. (2000) The Late Asteroidal and Cometary Bombardment of Earth as Recorded in Water Deuterium to Protium Ratio. *Icarus* 512, 508–512.

Dhuime, B., Wuestefeld, A., Hawkesworth, C.J. (2015) Emergence of modern continental crust about 3 billion years ago. 8–11.

Drake, M.J. (2005) Origin of water in the terrestrial planets. *Meteoritics and Planetary Science* 40, 519–527.

Genda, H., Ikoma, M. (2008) Origin of the ocean on the Earth: Early evolution of water D/H in a hydrogen-rich atmosphere. *Icarus* 194, 42–52.

Holland, G., Ballentine, C.J. (2006) Seawater subduction controls the heavy noble gas composition of the mantle. *Nature* 441, 186–91.

Jackson, C.R.M., Parman, S.W., Kelley, S.P., Cooper, R.F. (2015) Light noble gas dissolution into ring structure-bearing materials and lattice influences on noble gas recycling. *Geochimica et Cosmochimica Acta*. Elsevier Ltd 159, 1–15.

Johnson, B., Goldblatt, C. (2015) Earth-Science Reviews The nitrogen budget of Earth. *Earth Science Reviews* 148, 150–173.

Kadik, A.A., Kurovskaya, N.A., Ignat, Y.A., Kononkova, N.N. (2011) Influence of Oxygen Fugacity on the Solubility of Nitrogen , Carbon , and Hydrogen in FeO – Na 2 O – SiO 2 – Al 2 O 3 Melts in Equilibrium with Metallic Iron at 1 . 5 GPa and 1400 ° C. 49, 429–438.

Keller, C.B., Schoene, B. (2012) Statistical geochemistry reveals disruption in secular lithospheric evolution about 2.5 Gyr ago. *Nature*. Nature Publishing Group 485, 490–493.

Korenaga, J. (2011) Thermal evolution with a hydrating mantle and the initiation of plate tectonics in the early Earth. *Journal of Geophysical Research* 116, 1–20.

Krantz, J.A., Parman, S.W., Kelley, S.P. (2019) Recycling of heavy noble gases by subduction of serpentinite. *Earth and Planetary Science Letters*. Elsevier B.V. 521, 120–127.

Marty, B. (2012) The origins and concentrations of water, carbon, nitrogen and noble gases on Earth. *Earth and Planetary Science Letters*. Elsevier B.V. 313–314, 56–66.

Marty, B., Yokochi, R. (2019) Water in the Early Earth. *Reviews in Mineralogy and Geochemistry* 62, 421–450.

Marty, B., Zimmermann, L., Pujol, M., Burgess, R., Philippot, P. (2013) Nitrogen Isotopic Composition and Density of the Archean Atmosphere. *Science* 342, 101–104.

Mei, S., Kohlstedt, D.L. (2000) Influence of water on plastic deformation of olivine aggregates. *Journal of Geophysical Research* 105, 21457–21469.

Mikhail, S., Sverjensky, D.A. (2014) Nitrogen speciation in upper mantle fluids and the origin of Earth's nitrogen-rich atmosphere. *Nature Geoscience* 7, 816–819.

Morbidelli, A., Chambers, J., Lunine, J.I., Petit, J.M., Robert, F., Valsecchi, G.B., Cyr, K.E. (2000) Source regions and timescales for the delivery of water to the Earth. *Meteoritics & Planetary Science* 1320, 1309–1320.

Nakagawa, T., Nakakuki, T., Iwamori, H. (2015) Water circulation and gloal mantle dynamics: Insight from numerical modeling. *Geochemistry, Geophysics, Geosystems* 16, 1449–1464.

Owen, T., Mahaffy, P.R., Niemann, H.B., Atreya, S.K., Wong, M. (2001) Protosolar Nitrogen. *The Astrophysical Journal* L77–L79.

Parai, R., Mukhopadhyay, S. (2012) How large is the subducted water flux? New constraints on mantle regassing rates. *Earth and Planetary Science Letters*. Elsevier B.V. 317–318, 396–406.

Parai, R., Mukhopadhyay, S. (2015) The evolution of MORB and plume mantle volatile budgets: Constraints from fission Xe isotopes in Southwest Indian Ridge basalts. *Geochemistry, Geophysics, Geosystems* 16, 719–735.

Parai, R., Mukhopadhyay, S. (2018) Xenon isotopic constraints on the history of volatile recycling into the mantle. *Nature*. Springer US 560, 223–227.

Pepin, R.O. (2000) On the Isotopic Composition of Primordial Xenon in Terrestrial Planet Atmospheres. *Space Science Reviews* 92, 371–395.

Porcelli, D., Ballentine, C.J., Wieler, R. (2002) An Overview of Noble Gas Geochemistry and

Cosmochemistry. *Reviews in Mineralogy and Geochemistry* 47, 1–19.

Robert, F. (2003) The D/H Ratio in Chondrites. *Space Science Reviews* 106, 87–101.

Sandu, C., Lenardic, A., Mcgovern, P. (2011) The effects of deep water cycling on planetary thermal evolution. *Journal of Geophysical Research* 116, 1–15.

Sephton, M.A., Verchovsky, A.B., Bland, P.A., Gilmour, I., Grady, M.M., Wright, I.P. (2003) Investigating the variations in carbon and nitrogen isotopes in carbonaceous chondrites. *Geochim. Cosmochim. Acta* 67, 2093–2108.

Shirey, S., Richardson, S. (2011) Start of the Wilson Cycle at 3 Ga Shown by Diamonds from Subcontinental Mantle. *Science* 333, 434–437.

Smye, A.J., Jackson, C.R.M., Konrad-schmolke, M., Hesse, M.A., Parman, S.W., Shuster, D.L., Ballentine, C.J. (2017) Noble gases recycled into the mantle through cold subduction zones. *Earth and Planetary Science Letters*. Elsevier B.V. 471, 65–73.

Stern, R.J. (2005) Evidence from ophiolites, blueschist and ultrahigh-pressure metamorphic terranes that the modern episode of subduction tectonics began in Neoproterozoic time. *Geology* 33, 557–560.

Tang, M., Chen, K., Rudnick, R.L. (2018) Archean upper crust transition from mafic to felsic marks the onset of plate tectonics. *Science* 351.

Wilde, S.A., Valley, J.W., Peck, W.H., Graham, C.M. (2001) Evidence from detrital zircons for the existence of continental crust and oceans on the Earth 4.4 Gyr ago. *Nature* 409, 175–178.

Williams, C.D., Mukhopadhyay, S. (2018) Capture of nebular gases during Earth's accretion is preserved in deep-mantle neon. *Nature*. Springer US.

Figure 1 Control of parameters on regassing histories of nitrogen and xenon, shown as concentration in recycled material. Modelled regassing histories are controlled by four parameters: maximum recycling concentration (V_r^m), inflection point (β), growth rate (α) and, mantle processing rate (η). The maximum recycling concentration controls the final concentration in downwelling material and varies between zero and estimates of modern concentrations. The inflection point and growth rate control the timing and how rapidly the sigmoid transitions from zero downwelling to the maximum downwelling concentration, respectively. Growth rates ranging from 10^{-10} to 10^{-7} produce regassing histories ranging from effectively linear to nearly a step-function with inflection points ranging from 0 to 10 Gyr. The mantle processing rate represents the amount of material being degassed and recycled at each time step. Mantle processing rates decline exponentially, representative of secular cooling, and are used in combination with the regassing histories shown to calculate the amount of each volatile being recycled.

Figure 2 Predicted evolution of mantle nitrogen and xenon isotopes due to outgassing and coupled subduction. **(a,b)** Solid lines represent model results that produce accurate isotopic ratios and concentrations in the modern mantle and the dashed line represents the isotopic composition of the corresponding surface reservoir. **(c)**, Solid lines represent models producing accurate isotopic ratios and concentrations in the modern mantle whereas the field enclosed by dashed lines represents the full range of models which meet the criteria of success for either nitrogen or xenon. Due to very limited volatile recycling early in Earth history, there is little change in the mantle's $\delta^{15}N$ and $\delta^{128}Xe$ until 2.5 Ga.

Figure 3 Net flux of ^{14}N and ^{130}Xe into the mantle for successful models. Regassing of the mantle does not start until, at the earliest, 2.5 Ga for nitrogen and 1.8 Ga for xenon. For both systems there are two families of solutions. In those which peak (red lines), regassing of the mantle reaches a maximum in the last 2 Gyr and has since decreased towards steady-state. In those which gradually increase (black lines), the mantle is being regassed more today than it has in the past and the extent of that regassing will increase going forwards.

Figure 4 Predicted systematics for the hydrogen isotope system. **(a)** Solid lines show model results for δD in the mantle based on mantle processing rates constrained by the coupled N-Xe system. The corresponding surface reservoir for H is shown as dashed lines and changes through time as the result of hydrodynamic escape. **(b)** Net flux of H for successful models. Regassing of H into the mantle starts between 3.1 and 2.5 Ga and shows the same two types of solutions as the coupled N and Xe system: those which reached peak regassing in the past (red) and those in which regassing rates are still increasing (black). For comparison to the N and Xe systems, see Fig. 3.

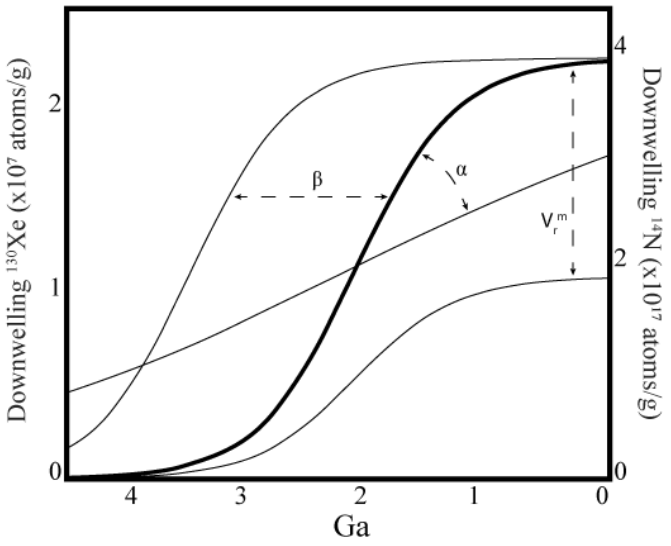
Downwelling ^{130}Xe (x10^{7} atoms/g)
Downwelling ^{14}N (x10^{17} atoms/g)
β
α
V_r^m
Ga
0
1
2
3
4

Figure 1

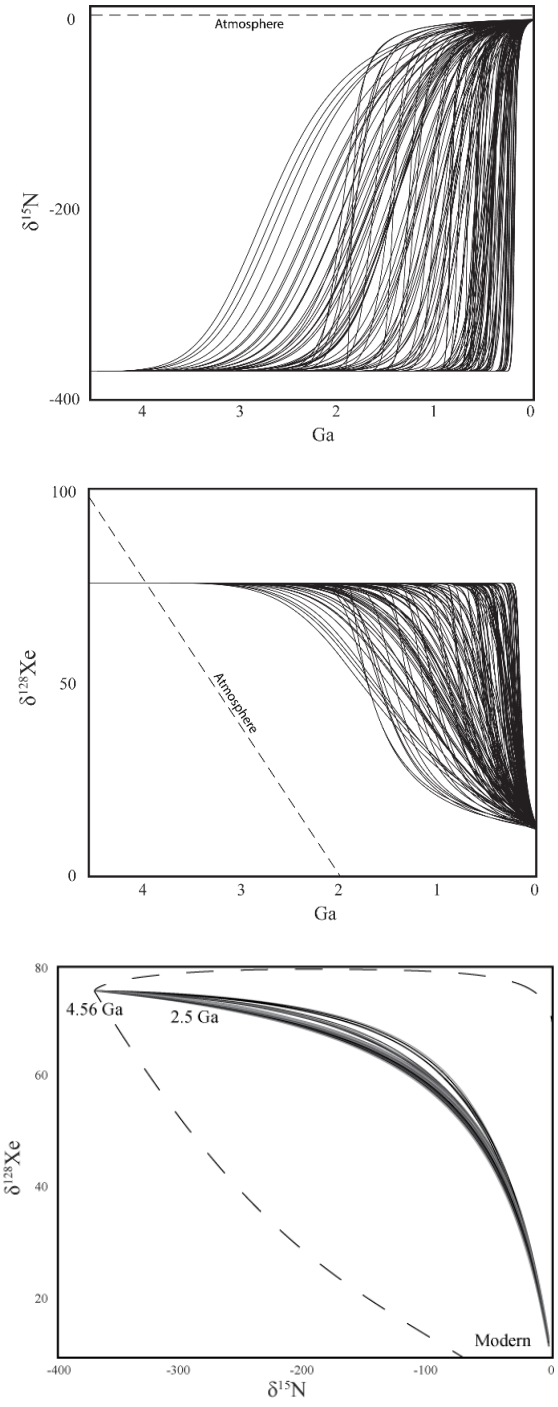
Atmosphere
0
-200
-400
δ15N
4
3
2
1
0
Ga
100
50
0
δ128Xe
Atmosphere
4
3
2
1
0
Ga
80
60
40
20
δ128Xe
4.56 Ga
2.5 Ga
Modern
-400
-300
-200
-100
0
δ15N

Figure 2

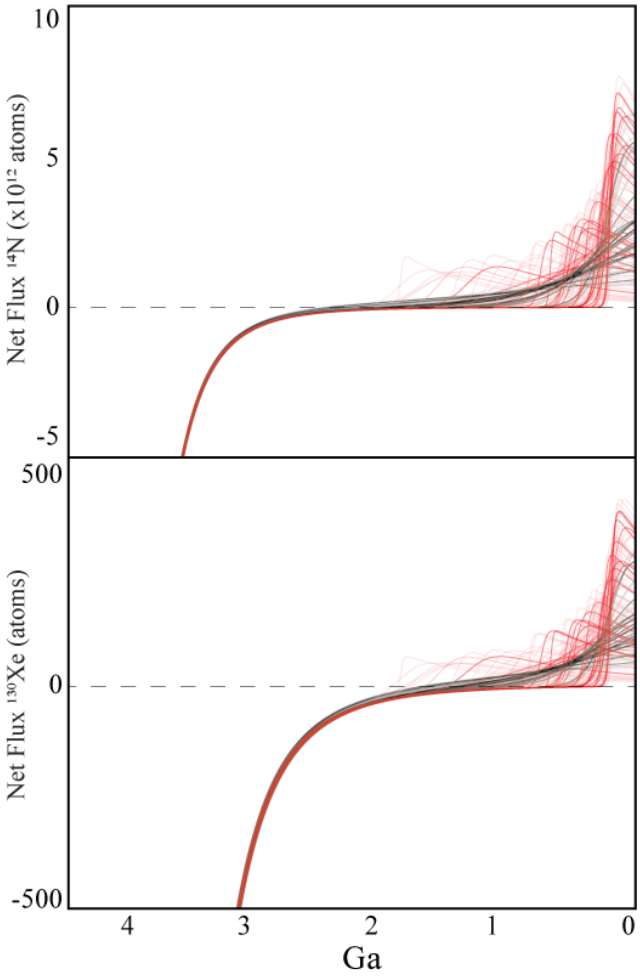
10
5
0
-5
Net Flux ^{14}N (x10^{12} atoms)
500
0
-500
Net Flux ^{130}Xe (atoms)
4
3
2
1
0
Ga

Figure 3

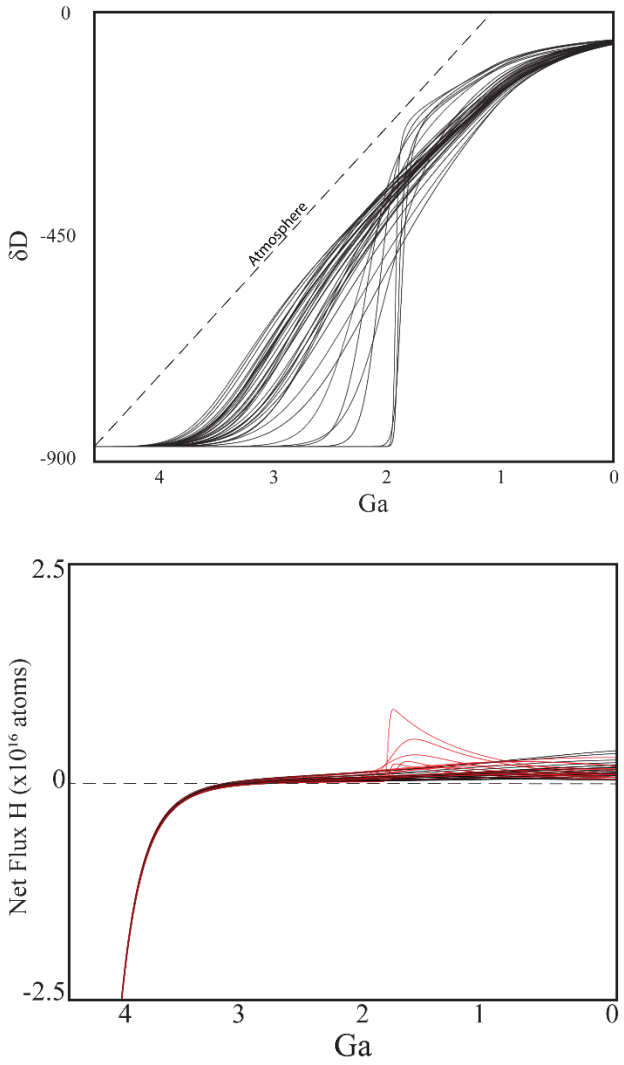
0
-450
-900
δD
Atmosphere
4
3
2
1
0
Ga
2.5
0
-2.5
Net Flux H (x10¹⁶ atoms)
4
3
2
1
0
Ga

Figure 4

Supplementary Materials

Supplementary Table 1: Range of variables used to model degassing and regassing.

			Symbol	Minimum	Maximum
		Inflection Point	α	0	1.00E+10
		Growth Rate	β	1.00E-10	5.00E-07
		Mantle Processing Rate	η	1.00E-10	1.00E-09
Maximum Recycled	Concentrations	H	V_r^H	0	3.10E+21
		N	V_r^N	0	4.50E+17
		Ne	V_r^{Ne}	0	1.00E+11
		Xe	V_r^{Xe}	0	5.00E+08

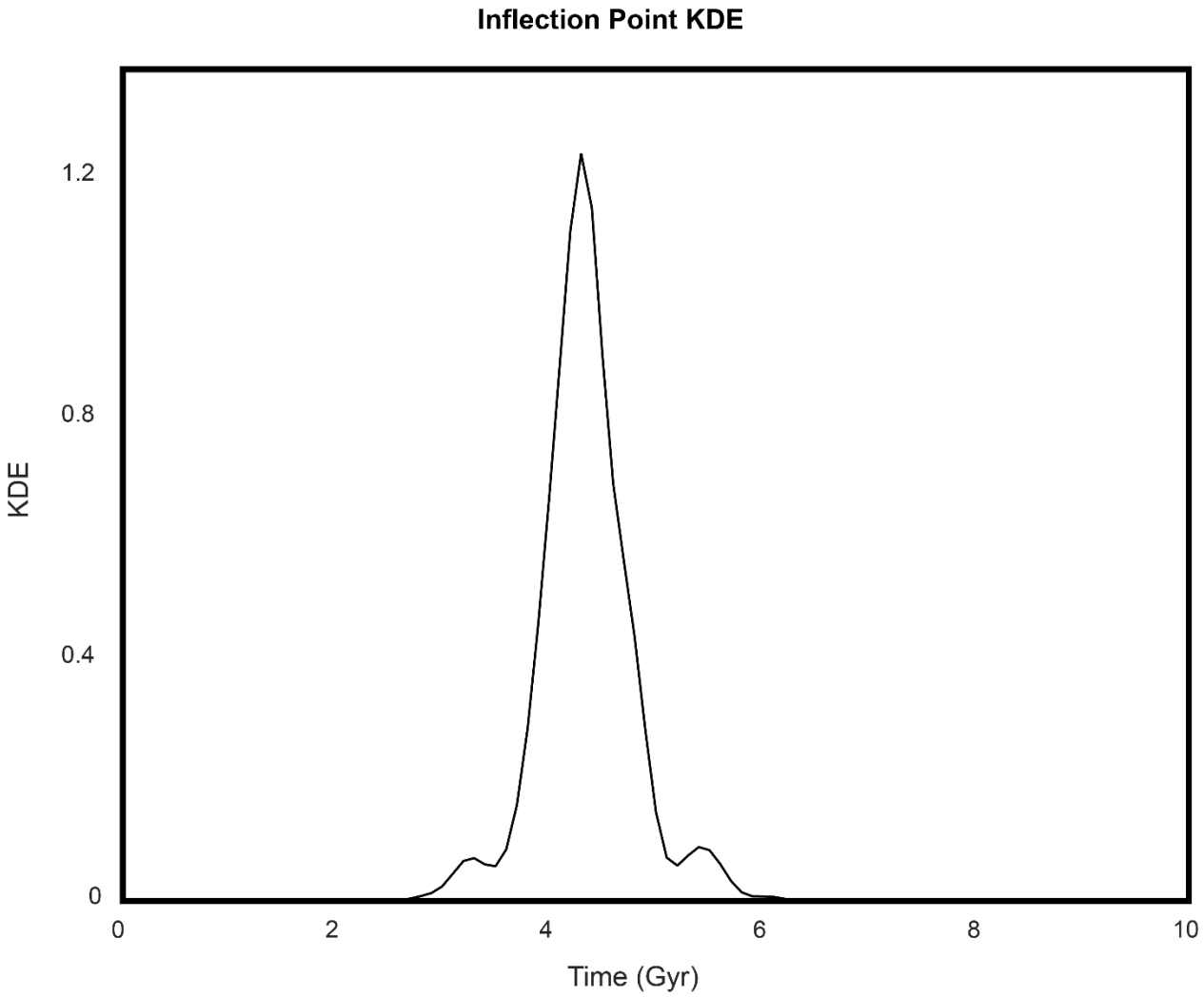

Supplementary Figure 1: Kernel density estimate of inflection points for successful N-Xe coupled model runs.

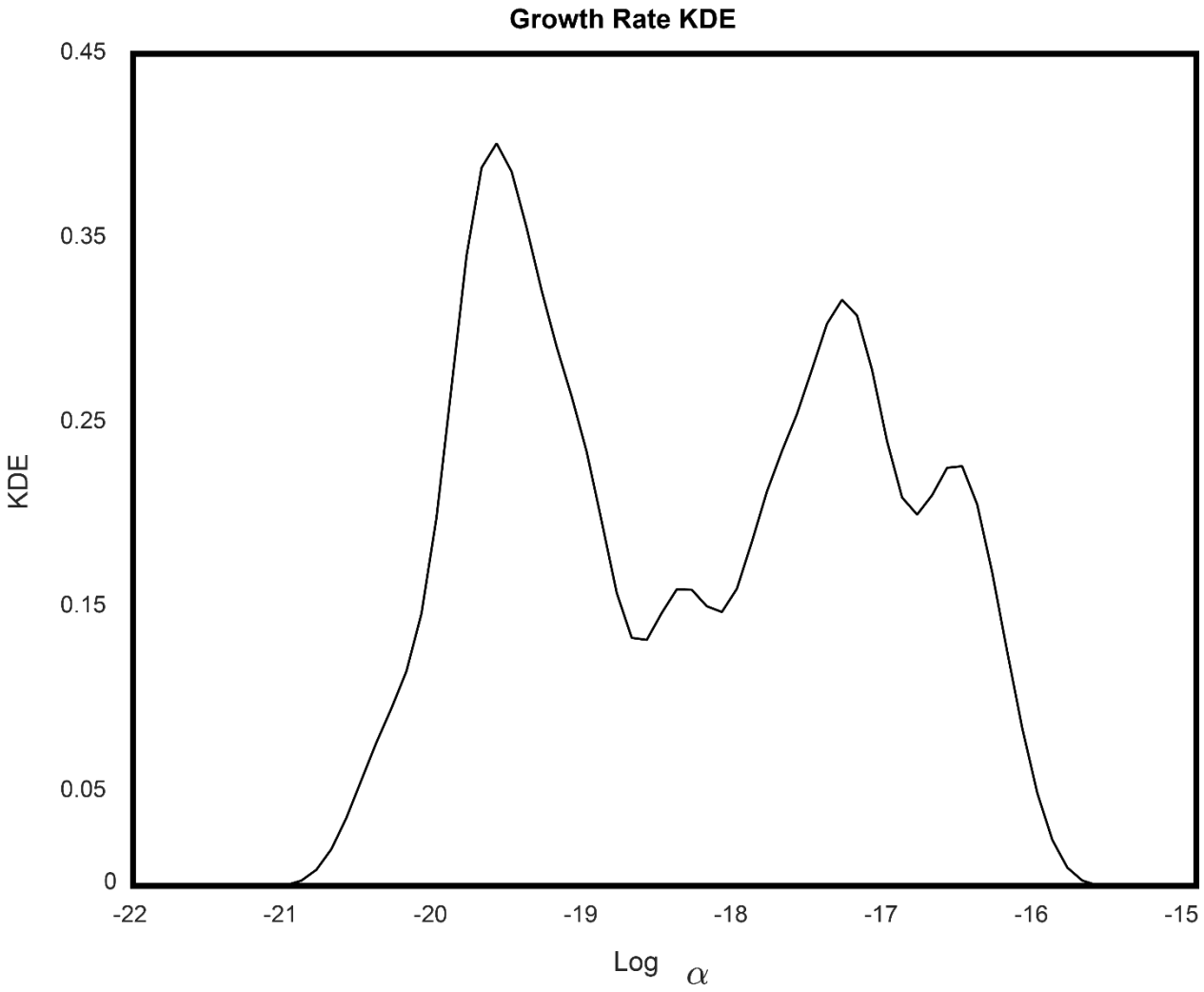

Supplementary Figure 2: Kernel density estimate of growth rate for successful N-Xe coupled model runs.

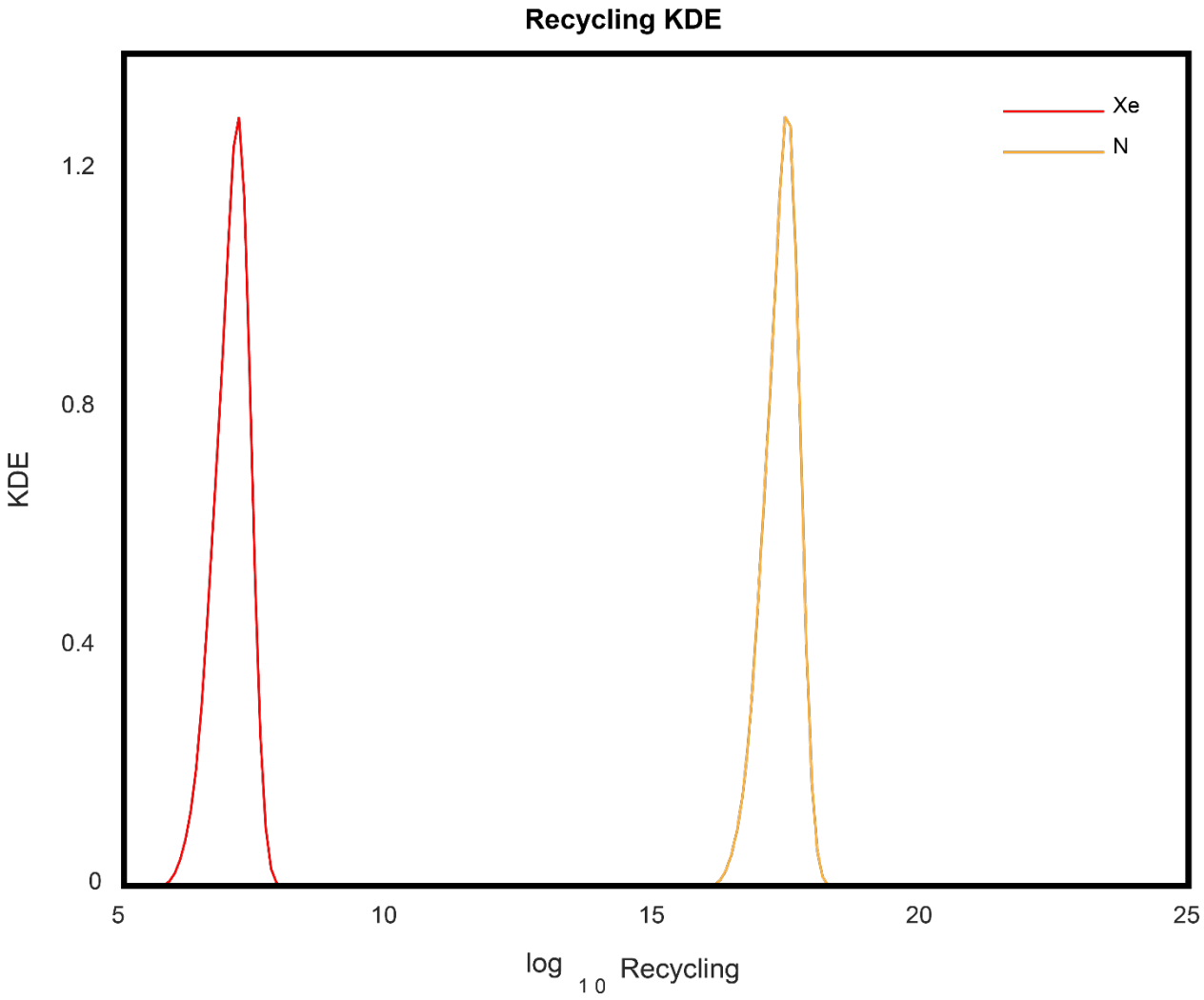

Supplementary Figure 3: Kernel density estimate of the maximum recycling concentration of N and Xe for successful N-Xe coupled model runs.

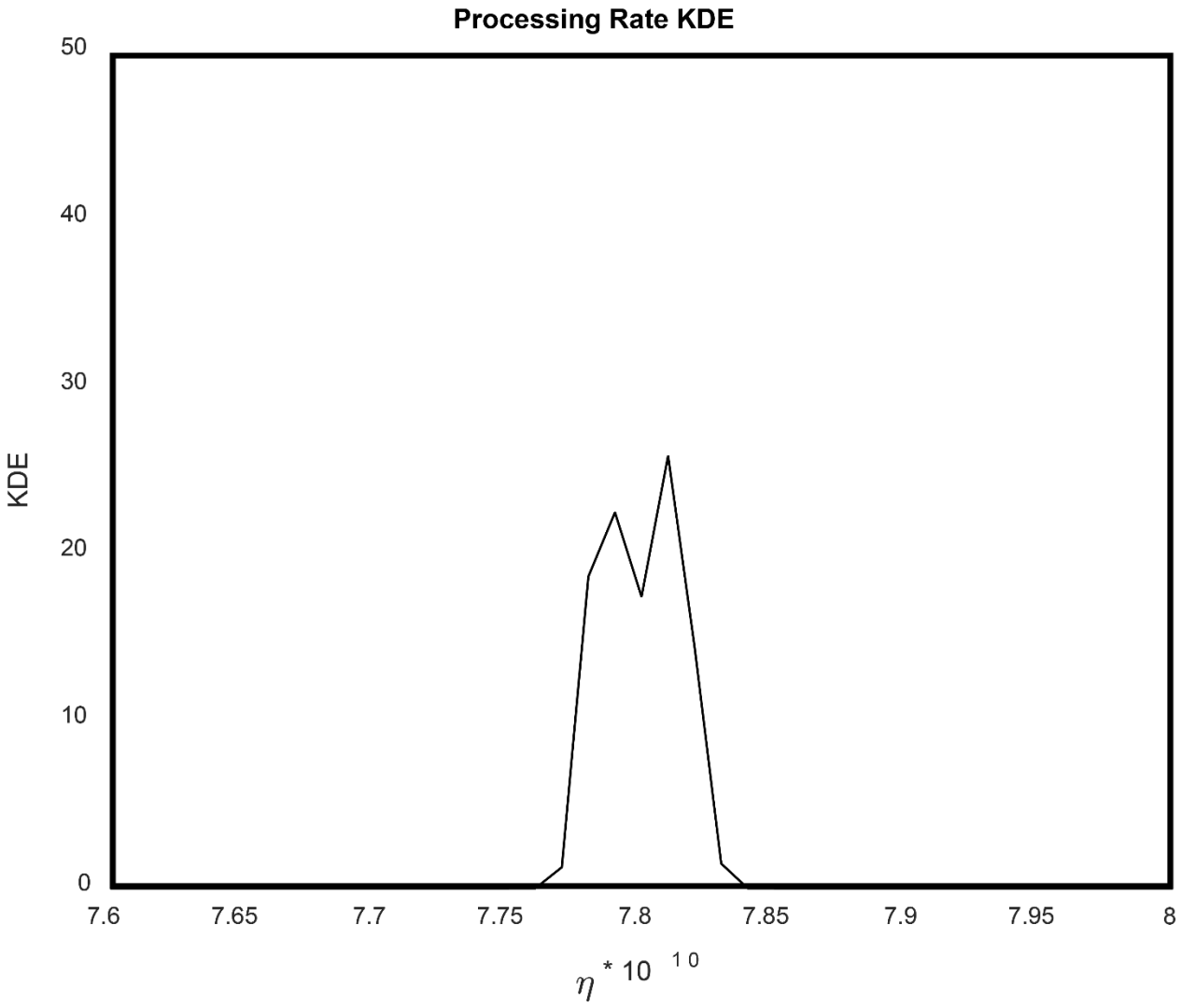

Supplementary Figure 4: Kernel density estimate of mantle processing rates for successful N-Xe coupled model runs.

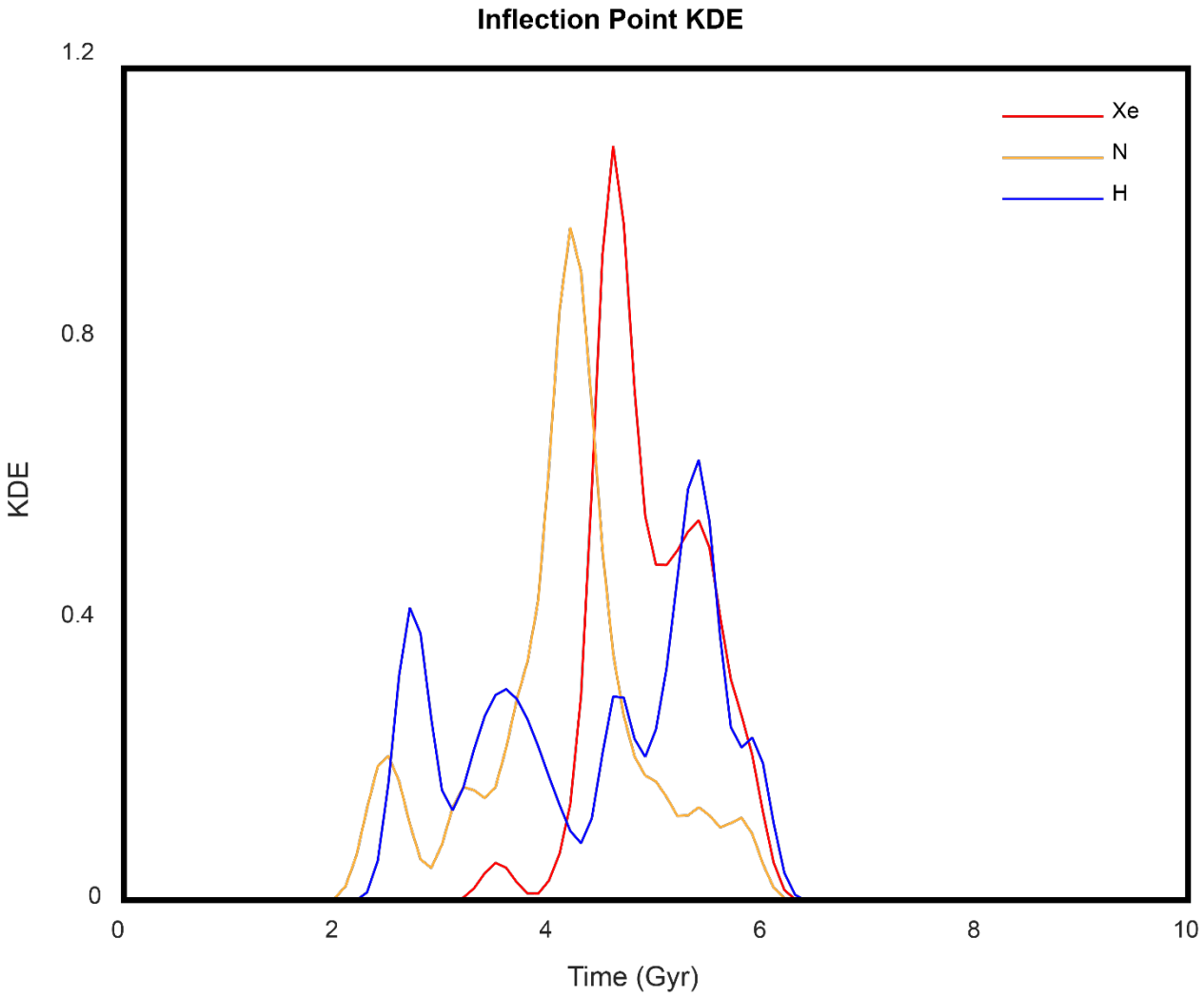

Supplementary Figure 5: Kernel density estimate of inflection points for H, N, and Xe in successful H-N-Xe model runs.

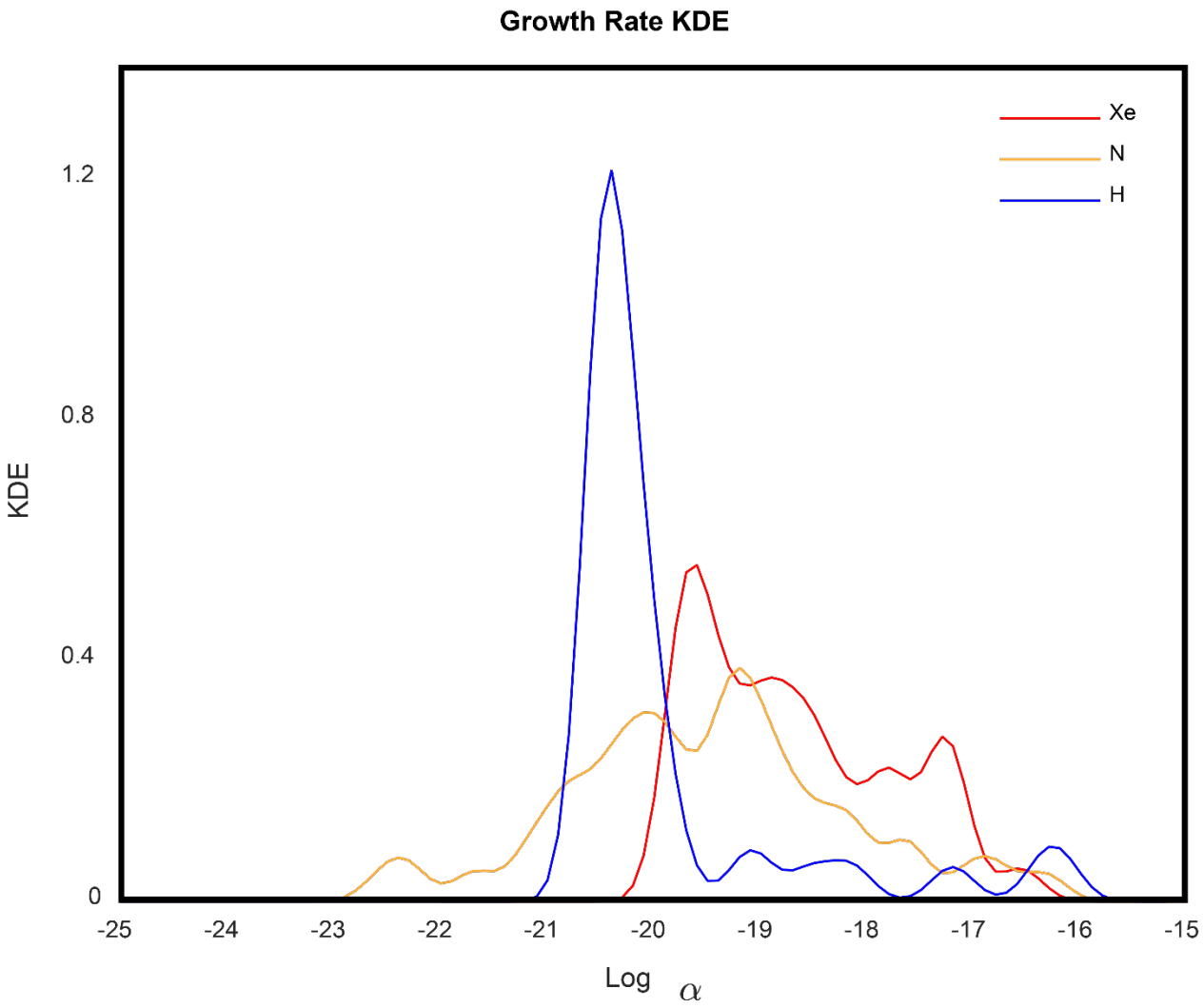

Supplementary Figure 6: Kernel density estimate of growth rate for H, N, and Xe in successful H-N-Xe model runs.

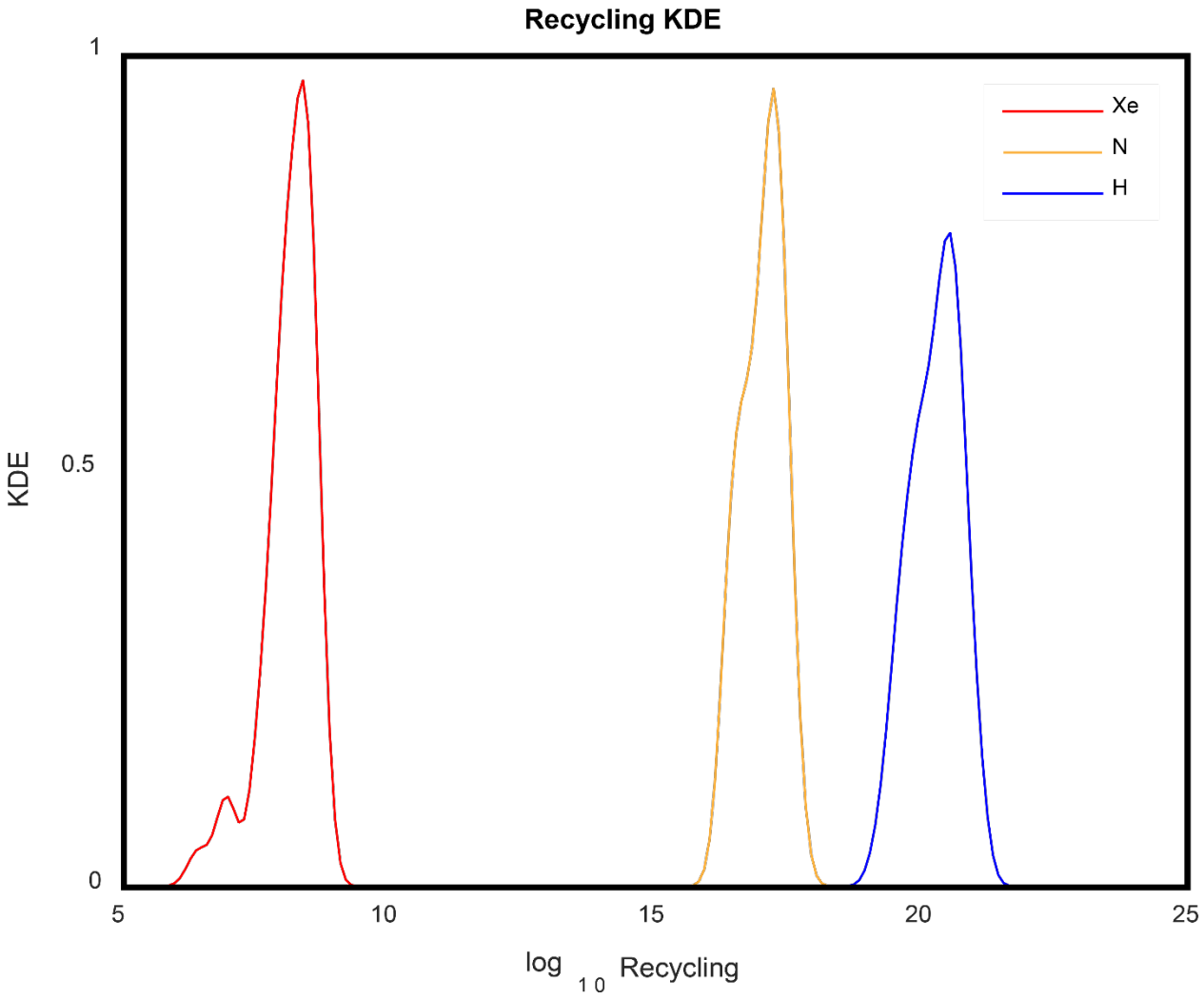

Supplementary Figure 7: Kernel density estimate of maximum recycling concentration for H, N, and Xe in successful H-N-Xe model runs.

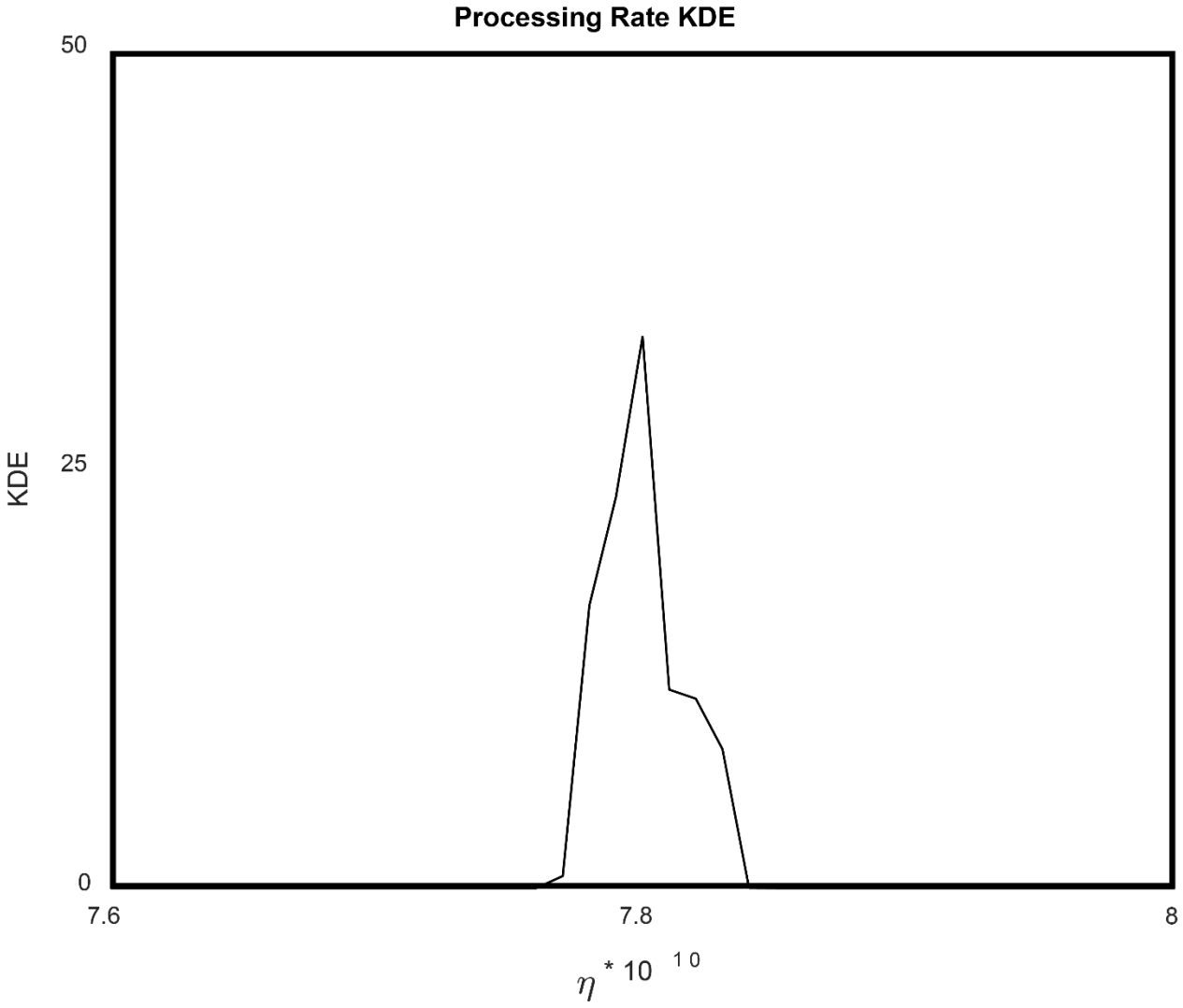

Supplementary Figure 8: Kernel density estimate of mantle processing rates for H, N, and Xe in successful H-N-Xe model runs.

CHAPTER THREE: KOMATIITIC ORIGIN OF ARCHEAN ANORTHOSITES

John A. Krantz and Stephen W. Parman

a Department of Earth, Environmental, and Planetary Sciences,

Brown University, Providence, RI

Abstract

Anorthosites from the Archean are characterized by their high Ca content and unique, megacrystic texture. These megacrystic anorthosites formed only between 2.5 and 3.8 Ga and are closely associated with contemporaneous greenstone belts. Previous works have speculated on a connection between these anorthosites and komatiites, which are similarly temporally constrained. To explore this possible connection, we perform thermodynamic modelling of the formation of Archean anorthosites using MELTS.

The high-Ca plagioclase observed in Archean anorthosites are consistent with crystallization of komatiites followed by an event which separates the liquid fraction and emplaces it at shallower depths in the crust. The petrogenetic connection between Archean megacrystic anorthosites and komatiites explains, in part, the temporal restriction of megacrystic, high-Ca anorthosites to the Archean as their source—komatiites—is also restricted to that period. This also explains the connection between Archean anorthosites and greenstone belts in general, and suggests that anorthosites record the crystallization conditions—including volatile contents—of magmas at that time.

Introduction

The oldest anorthosites found on Earth are from the Archean (2.49-3.73 Ga) and contain extremely calcic plagioclase (An_{61}-An_{94}, average An_{80}). Though volumetrically small, Archean anorthosites received a lot of attention following the Apollo program because of their similarity to high-calcium anorthosites found on the surface of the moon (e.g., Phinney *et al.*, 1979). These lunar anorthosites represent a primordial crust which formed during magma ocean crystallization, however, it has since been shown that the Archean megacrystic anorthosites are not primordial.

Rather, they are a component of greenstone belts as has been established by numerous petrologic and field studies (Ashwal and Myers, 1987; Burke, 1979; Phinney *et al.*, 1988).

Archean anorthosites, as exposed at the surface today, are typically small (~100 km^2) and were emplaced as sheets and sills in mafic lavas, tuffs, and gabbros at relatively shallow depths (Ashwal, 1993, 2010; Phinney *et al.*, 1988). In addition to the unusually high calcium content, plagioclases in these bodies also have a unique megacrystic texture: single crystals of plagioclase are typically equidimensional, chemically unzoned, 0.5 to over 30 cm in diameter, and are surrounded by a fine-grained gabbroic groundmass or other interstitial mafic silicates (Ashwal and Bybee, 2017). The bulk composition measured for a subset of megacrystic anorthosites is shown in Figure 1 and Supplementary Table 1. All exposures of these anorthosites have been hydrously altered and metamorphosed to some degree, and the extensive alteration of primary mafic silicates to amphiboles, chlorite, albite, calcite, and quartz has made it particularly challenging to characterize the parental composition. In certain exposures, interstitial amphiboles have been interpreted as primary, however, this is contentious and inconsistent between different localities (Ashwal and Bybee, 2017; Myers, 1985; Polat *et al.*, 2009; Rollinson *et al.*, 2010; Weaver *et al.*, 1981; Windley and Garde, 2009).

Consistent, close spatial associations between Archean anorthosites and the mafic dikes within greenstone belts has been used to suggest a genetic relationship, as have chemical and isotopic analyses (Ashwal, 1993, 2010; Ashwal and Bybee, 2017; Collerson *et al.*, 1976; McGregor *et al.*, 1985; Phinney *et al.*, 1988; Phinney and Halls, 2001). Generally, these anorthosites are considered to have been generated in oceanic environments based on their low U concentrations and high Th/U ratios (e.g., Garson and Livingstone, 1973; Weaver *et al.*, 1981). Additionally,

some anorthosite complexes are also characterized by Nb depletion, a fingerprint of subduction-related, oceanic arc magmas (e.g., Hawkesworth *et al.*, 1993). The oxygen and hydrogen isotopes of rocks within the Fiskenaesset complex also record a signature of hydrothermal alteration via heated seawater (Peck and Valley, 1996). Collectively, these lines of evidence suggest that the parental melts from which Archean anorthosites formed were wet, an important factor in considering the origin of the anomalously large, equant plagioclase crystals. Such large, unzoned crystals do not form in normal geological environments and may instead be the result of an unusually large volume of melt relative to the solids, a distinct cooling history, or high volatile contents. Water plays another important role in delaying the crystallization of silicates during cooling, which will affect the order and extent of crystallization. Of particular importance to the Ca/Na ratio of crystallizing plagioclase are the changes in the stability of clinopyroxene relative to plagioclase under hydrous conditions. Specifically, compared to dry conditions, the onset of plagioclase crystallization is delayed more than is that of cpx, which will result in a less calcic, more sodic melt at plag-in.

Anorthosites which have formed more recently (<2.5 Ga) are petrologically distinct from the megacrystic, Archean anorthosites. These Proterozoic anorthosites form as intrusive bodies of nearly pure anorthosite ranging from tens to tens of thousands of square kilometers in area, leading to their designation as "massif-type" anorthosites. Individual grains within these bodies are typically 1 to 10 cm long, euhedral, lath-shaped crystals which are occasionally zoned and have distinctly lower An# than their Archean counterparts (An_{30}-An_{70}, Fig. 2) (Ashwal and Bybee, 2017). Though historically contentious, a consensus has been reached on the origin of massif-type anorthosites: parental magmas of broadly basaltic composition reach the lower crust and assimilate a portion of lower crustal material prior to crystallization and subsequent

emplacement (Ashwal *et al.*, 1986; Hill, 2017; Peck *et al.*, 2010). The important contribution of crustal material for the formation of massif-type Proterozoic anorthosites further differentiates them from Archean anorthosites which show little to no crustal contamination (Ashwal and Bybee, 2017). To that end, we investigate the potential of a high-Al basalt (HAB) precursor of Proterozoic massif-type anorthosites to form plagioclase with Ca contents as high as the Archean megacrystic anorthosites if it remains uncontaminated.

In the absence of a modern analogue for comparison, many authors have investigated the temporal correlation of Archean anorthosites and komatiites, which are also largely restricted to the Archean. Experimental work has shown that at low pressure, anhydrous komatiitic compositions crystallize plagioclase with moderate to high Ca contents as a result of extreme fractional crystallization of the initial komatiite (Fig. 3) (Francis and Hynes, 1979; Kinzler and Grove, 1985; Thy, 1995). However, a hydrous origin for komatiites has been proposed with water contents as high as 6 wt% (Asafov *et al.*, 2018; Grove and Parman, 2004; Parman *et al.*, 1997; Sobolev *et al.*, 2016). Such hydrous komatiites are generated from either subduction environments or hydrous plumes. Such an environment has been compared to modern boninites, the result of high degrees of hydrous melting in subduction environments, which contain high-Ca plagioclase phenocrysts similar to those in Archean anorthosites (Ashwal and Bybee, 2017; Danyushevsky *et al.*, 1997). Boninites have also been identified interlayered with komatiites from the Archean, providing additional strong evidence of their connection (e.g., Fan and Kerrich, 1997; Kerrich *et al.*, 1998). Komatiites have been hypothesized to have formed in a variety of environments including plumes, subduction zones, back-arcs, and via impact. Whatever the tectonic setting, the presence of water in komatiitic melt will influence the liquid line of descent and the An content of crystallizing plagioclase.

While rare, modern geological systems do produce high calcium plagioclase in mid-ocean ridges and ocean islands, however, none of these settings combine the high Ca contents with the equant, nearly spherical textures and lack of zoning observed in Archean megacrystic anorthosites (Beard and Barker, 1989; Hansen and Gronvold, 2000; Hellevang and Pedersen, 2008; Kimata *et al.*, 1995; Komor and Elthon, 1990; Sheth, 2016; Stroup and Fox, 1981). The anorthite content of crystallizing plagioclase is primarily a function of the melt's Al/Si ratio, Ca/Na ratio, and water contents. This behavior has been identified from experimental studies (e.g., Danyushevsky *et al.*, 1997; Fram and Longhi, 1992; Housh and Luhr, 1991; Sisson and Grove, 1993) as well as trends in natural data (Fig. 4).

Archean anorthosites also contain layers of chromite which can be used to further constrain their origin. When plotted as Cr/(Cr + Al) vs $Fe^{2+}/(Fe^{2+} + Mg)$ (herein Cr# vs Fe#), the composition of chromites associated with Archean anorthosites forms a distinct field with higher Fe# than modern MORB and OIBs (Barnes and Roeder, 2001; Rollinson, 1995; Rollinson *et al.*, 2002, 2010) (Fig. 5). These chromite compositions further distinguish Archean anorthosites from other systems in which high-Ca plagioclase crystallizes.

If Archean megacrystic anorthosites are petrogenetically linked to komatiites, then the restriction of high An, megacrystic anorthosite to greater than 2.5 Ga is a direct consequence of the conditions which limit komatiitic eruptions to the Archean. To this end, we expand on previous work (Kinzler and Grove, 1985; Thy, 1995) by investigating the effects of initial composition and water contents on the composition and mass fraction of plagioclase crystallizing from a range of komatiitic melts.

Methods

To explore the possible petrologic connection between HABs (the precursor of Proterozoic anorthosites) or komatiites and Archean anorthosites, we start with Al-depleted and -undepleted komatiites and one HAB and use the thermodynamic model of MELTS to perform crystallization calculations (Gualda and Ghiorso, 2015). Starting compositions were based on the composition of komatiites from Barberton (Al-depleted) and Abitibi (Al-undepleted) as collated by Arndt *et al.* (2008). The initial HAB composition was based on previous experimental work on the origin of Proterozoic anorthosites (Hill, 2017).

To account for the high mobility of Na and Ca—of particular importance for the An# of crystallizing plagioclase—all available data for komatiites from these regions were gathered from the GEOROC database. For each region, the complete, unfiltered set of whole rock data were plotted as Na_2O vs MgO and CaO vs MgO (Fig. 6). In nearly all cases of alteration, komatiites have been shown to lose Ca and Na, so it is assumed that at high MgO contents (> 20 wt%) the highest Ca and Na contents are closest to the initial igneous composition. In rare cases, alteration producing talc and carbonates increases the Ca contents, so high-Ca outliers are not considered in correcting for alteration. As olivine is the only major phase to crystallize above 20 wt% MgO, an olivine fractionation trend was identified by drawing a line from the average composition of olivines in the komatiites through the highest Ca and Na values (i.e. least altered) and the intercept of this trend with the MgO content of the komatiite bulk rock was used as the alteration-corrected composition for modelling (Table 1).

The corrected starting compositions were used as the starting composition, and MELTS crystallization paths were calculated with 0 and 1 wt% water at 1 kbar. Equilibrium crystallization was allowed to proceed from the liquidus—typically through olivine, spinel, and clinopyroxene—to the onset of plagioclase crystallization. At the conditions where plagioclase first begins forming, the composition of the remaining liquid was used to start a new MELTS crystallization path (i.e. fractionated fully from all of the previously crystallized olivine, spinel, and cpx) (Table 2). It is assumed that there is no degassing of H_2O from the magma during crystallization, and the remaining liquid is thus enriched in water under hydrous conditions. The An# and mass fraction of plagioclase resulting from complete crystallization of the remaining liquid were used as criteria to identify possible sources of Archean anorthosites.

Results

Olivine is the liquidus phase for both the Abitibi and Barberton compositions between 1500 and 1600 °C (Fig. 7a, c, S1). Chromite is the second phase to crystallize, saturating between 1400 and 1500 °C. The second silicate to precipitate for both compositions under dry conditions is opx. Crystallization of opx is followed by complete resorption of opx to form cpx between 1200 and 1250 °C. This is followed by substantial, but not complete, resorption of cpx to form opx between 1150 and 1200 °C. Immediately after the resorption of cpx to form opx, cpx again crystallizes from the melt, reaching a similar or greater mass fraction as before resorption for Barberton and Abitibi, respectively. Under hydrous conditions cpx is the second phase to crystallize, followed by opx.

As crystallization of olivine and pyroxene proceeds, the Al/Si ratio in the komatiitic melts increases until plagioclase starts to crystallize at Al_2O_3/SiO_2 ratios between 0.25 and 0.31 (Figure

10a). As the Al-depleted Barberton composition has a lower initial Al_2O_3/SiO_2 ratio than the Al-undepleted Abitibi composition, substantially more crystallization is needed to reach plagioclase saturation in the Barberton composition than in the Abitibi composition (85 % and 70 %, respectively; Fig. 10c). However, both compositions saturate in cpx at roughly the same melt fraction (~0.5; Fig. 10a). Prior to cpx saturation, Ca/Na ratios in the melts are effectively constant, and then decrease once cpx forms. The longer interval between cpx saturation and plag saturation in the Barberton composition produces a much lower CaO/Na_2O ratio than the Abitibi composition (<4 and 17-22, respectively; Fig. 10b). In hydrous cases, the concentration of H_2O steadily increases to 3.18 and 3.75 wt% H_2O for Abitibi and Barberton, respectively (Fig. 10d). At the temperature where cpx begins to crystallize, there is a sharp increase in dF/dT (Fig. 9), and a second sharp increase in slope at the point where plag begins to crystallize. At the temperature where plagioclase first crystallizes, we start a new iteration of the model using the remaining liquid.

For the new iteration of the model using the remaining liquid, plagioclase is one of the liquidus phases. Under dry conditions, cpx also crystallizes at the liquidus whereas it is slightly delayed for wet compositions where opx takes its place as the second liquidus phase. For the dry Abitibi composition, opx begins to crystallize via resorption of cpx between 1000 and 1050 °C. For Barberton, in contrast, opx does not crystallize under dry conditions. The bulk composition of these fractionated liquids is compared to that of natural Archean anorthosites in Fig. 8. For most of the initial compositions, this crystallization produces a decrease in both Al_2O_3/SiO_2 and CaO/Na_2O ratios at lower melt fractions, with some minor variation at $F < 0.2$ (Figs. 11-12). For the Abitibi compositions, however, the Ca/Na ratio increases over the entire range, especially at low melt fractions. This increasing Ca/Na ratio continues to produce Anorthite with high Ca

contents at low melt fractions whereas the other compositions gradually become more sodic. Compared to the natural samples, the initial fractionated liquids are distinctly enriched in TiO_2 and H_2O by 0.5-1 and 1-2 wt%, respectively. They are also slightly lower or at the minima for Al_2O_3 and CaO and well below the natural samples' Fe contents. For Na_2O, the two compositions bracket the range of natural samples.

The composition of spinel group minerals (e.g., chromite) crystallizing throughout the course of the model runs is also tracked for the komatiitic compositions (Figs. 13-14). For the initial komatiitic compositions, spinel group minerals initially increase in Fe# at constant Cr#. At cpx-in, the Fe# becomes effectively constant while the Cr# decreases. At plag-in, both Fe# and Cr# begin to increase. For the model iterations using the remaining, separated liquid composition, the increasing trend for both Fe# and Cr# continues with plagioclase crystallization. In the Barberton compositions, the drastic change in the trend corresponds to the onset of Ti-oxide crystallization (i.e., ilmenite and geikielite). The smaller change in the trend for Abitibi compositions corresponds with both Ti-oxide crystallization and a simultaneous conversion of clinopyroxene to orthopyroxene. The progressive crystallization of the komatiitic composition approaches Archean anorthosites, and the crystallization of the remaining liquid component follows the trend identified in Fiskenaesset, if at slightly lower Fe# (Rollinson *et al.*, 2002). All modelled compositions are low in Fe compared to natural Archean anorthosites and further study of iron-rich komatiitic compositions is necessary (Fig. 8). Spinel group minerals do not crystallize for HAB as the initial composition contains no Cr. An important step in future iterations of this modelling will be to identify the appropriate Cr contents of Proterozoic anorthosite protoliths and model the composition of HAB with this added Cr.

Discussion

All of the compositions modelled are able to produce plagioclase with An# as high as An_{78}, roughly equivalent to the average of An_{80} in Archean anorthosites. The composition of the first-crystallized plagioclase is always at the highest An#, and subsequent crystallization will become progressively more sodic. The highest An# plagioclase forms from the Abitibi composition as a result of the relatively high CaO/Na_2O ratio of both the initial komatiitic melt and the remaining liquids (Fig. 15). This high initial CaO/Na2O ratio is further increased relative to the other compositions by the delay of cpx saturation. In contrast, the Barberton compositions saturate with cpx well before plag and are thus reduced in Ca when plag saturation is reached. While lower than in the whole rock analyses of Archean anorthosites, the Al_2O_3/SiO_2 ratios of all compositions are roughly the same as or slightly lower than that of the estimated parental composition for Fiskenaesset, Messina, and Bad Vermillion Lake (Ashwal, 1993). The sharp rise in the Ca/Na ratio of the dry, Abitibi komatiitic composition corresponds to the resorption of cpx and crystallization of opx which occurs over the same temperature interval as plagioclase begins crystallizing (Fig. 8a).

The similarity of the chromite compositions produced by the model to the trends identified by Rollinson *et al.* (2002) for natural systems provides further evidence for the komatiitic origin of Archean anorthosites (Figs. 12-13). The initial chromites fall within the boninite field and pass through the Archean komatiitic fields during progressive crystallization. The composition of the last chromites to form moves towards—and for the Abitibi composition, into—the field of anorthosites from Messina. While at higher Cr# or lower Fe# than the natural chromites in Fiskenaesset, both the natural samples and modelled compositions evolve towards higher Cr# and Fe# along the same slope.

In addition to the chemical difference between the Proterozoic (HAB-derived) and Archean anorthosites, the mechanism by which the two concentrate plagioclase is likely different. In the case of Proterozoic anorthosites, it is clear that plagioclase is concentrated gravitationally as plagioclase at or below An_{65} will readily float in basaltic melts under crustal pressures (Kushiro, 1980; Longhi and Ashwal, 1985). After concentrating plagioclase, the crystal-rich mush ascends through the continental crust and is emplaced as the nearly monominerallic, massive bodies observed in Proterozoic terranes. Conversely, Archean megacrystic anorthosites have not been gravitationally segregated from their host melt. Instead, the large crystals of plagioclase are hosted in a broadly basaltic matrix with outcrop-scale variation in the relative abundance of plagioclase and matrix. These textural characteristics are consistent with the minimal density contrast between plagioclase crystals and melt in the model. For the komatiitic compositions modelled herein, resultant plagioclase are within 0.1 g/cm^3 of the density of the remaining melt, slightly denser than the melt under hydrous conditions and slightly buoyant for dry compositions. This suggests that the large, neutrally buoyant plagioclase crystals were entrained in the basaltic melts during their emplacement near the surface, effectively separating them from the mafic cumulates. Phinney *et al.*, (1988) identified less calcic rims on plagioclase crystals—both megacrystic and within the matrix—from a variety of locales. These more sodic rims are interpreted to be evidence of a two-stage crystallization process, one at relatively high pressure forming the calcic megacrysts, and a subsequent low-pressure stage following emplacement at shallow depths by the fractionated melt. This two-stage model is consistent with the near-neutrally buoyant plagioclase observed in the models herein (Fig. 16).

Based on geochemical evidence, it appears that Archean anorthosites formed in oceanic environments from hydrous melts. The trace element composition of anorthosites and associated mafic rocks from the Fiskenaesset Complex—including La/Th, Sm/Th, Yb/Th, and Nb/Th—suggest that they originated in an island arc (Polat *et al.*, 2009). Similar conclusions have been reached based on trace elements as well as Hf and Nd isotopes for anorthosites from southern West Greenland, the Sittampundi Complex in southern India, and the Bad Vermillion Lake Complex in Ontario, Canada (Hoffmann *et al.*, 2012; Mohan *et al.*, 2013; Zhou *et al.*, 2015). Likewise, petrologic evidence from primary minerals and melt inclusions indicates that komatiites formed from hydrous melts (Asafov *et al.*, 2018; Grove and Parman, 2004; Parman *et al.*, 1997, 2002; Sobolev *et al.*, 2016, 2019). Furthermore, many komatiites are interlayered with boninites which form from high degrees of hydrous melting (Kerrich *et al.*, 1998; Parman *et al.*, 2001; Poidevin, 1994; Wilson, 2003). Modern boninites are produced under conditions associated with the onset of subduction (Stern and Bloomer, 1992) and are also host to large phenocrysts of high-Ca plagioclase with textures similar to those in Archean anorthosites (Danyushevsky *et al.*, 1997; Kimata *et al.*, 1995; Sobolev and Danyushevsky, 1994).

If, as has been suggested, boninites are roughly the modern equivalent of at least some komatiites (high degree, hydrous melts from the initiation of subduction), then the presence of the closest modern approximation to Archean megacrystic plagioclase suggests a komatiitic origin for Archean anorthosites. The combination of this example from natural systems, with the model results herein is strong evidence of the connection between the two and is consistent with the geochemical characteristics of Archean anorthosite complexes. Komatiitic melts with varying water contents would explain the presence of primary amphibole in some, but not all, Archean anorthosite complexes, as well as the associated geochemical characteristics.

By connecting the formation of Archean anorthosites to komatiitic magmas, the question of why high An, megacrystic anorthosites are restricted to the Archean becomes the same as why are komatiites largely restricted to the Archean? The origin of komatiites is beyond the scope of this work. Many hypotheses for their disappearance have been proposed, most of which relate either directly or indirectly to the secular cooling of the Earth (e.g., Arndt *et al.*, 2008; Asafov *et al.*, 2018; Bickle *et al.*, 1975; Herzberg, 1992; Herzberg *et al.*, 2007; Parman *et al.*, 1997; Sobolev *et al.*, 2016). Further, experimental work to validate the results of our thermodynamic modelling will be an important contribution to the ongoing investigation of the Archean Earth.

Conclusions

We present the results of thermodynamic modelling using MELTS for the formation of Archean, megacrystic anorthosites from high-Al basalt and komatiites. The high-Ca plagioclase observed in Archean anorthosites is consistent with crystallization of a wet, Al-undepleted komatiites followed by separation of the remaining liquid from the crystallized olivine and pyroxene. The petrogenetic connection between Archean megacrystic anorthosites and komatiites explains, in part, the temporal restriction of megacrystic, high-Ca anorthosites to the Archean as their source—komatiites—is also restricted to that period. The cause of komatiites' temporal restriction remains an open and important question for future work. If Archean anorthosites are a by-product of komatiitic melts, the similarity of plagioclase found in modern boninites and Archean anorthosites adds to the growing evidence that boninites are a modern parallel to komatiites.

References

Arndt, N., Lesher, M., Barnes, S. (2008) *Komatiite*. Cambridge University Press, Cambridge.

Asafov, E. V., Sobolev, A. V., Gurenko, A.A., Arndt, N.T., Batanova, V.G., Portnyagin, M. V., Garbe-Schönberg, D., Krasheninnikov, S.P. (2018) Belingwe komatiites (2.7 Ga) originate from a plume with moderate water content, as inferred from inclusions in olivine. *Chemical Geology*. Elsevier 478, 39–59.

Ashwal, L.D. (1993) *Anorthosites*. Springer-Verlag.

Ashwal, L.D. (2010) The temporality of anorthosites. *The Canadian Mineralogist* 48, 711–728.

Ashwal, L.D., Bybee, G.M. (2017) Crustal evolution and the temporality of anorthosites. *Earth-Science Reviews*. Elsevier 173, 307–330.

Ashwal, L.D., Myers, J.S. (1987) Archean Anorthosites. *Developments in Precambrian Geology* 315–355.

Ashwal, L.D., Wooden, J.L., Emslie, R.F. (1986) Sr, Nd, and Pb isotopes in Proterozoic intrusives astride the Grenville Front in Labrador: Implications for crustal contamination and basement mapping. *Geochimica et Cosmochimica Acta* 50, 2571–2585.

Barnes, S.J., Roeder, P.L. (2001) The range of spinel compositions in terrestrial mafic and ultramafic rocks. *Journal of Petrology* 42, 2279–2302.

Beard, J.S., Barker, F. (1989) Petrology and tectonic significance of gabbros, tonalites, shoshonites, and anorthosites in a late paleozoic arc-root complex in the wrangellia terrane, southern alaska. *Journal of Geology* 97, 667–683.

Bickle, M.J., Martin, A., Nisbet, E.G. (1975) Basaltic and peridotitic komatiites and stromatolites above a basal unconformity in the Belingwe greenstone belt, Rhodesia. *Earth and Planetary Science Letters* 27, 155–162.

Burke, K. (1979) How Much Are Early Terrestrial Anorthosites Analogues of Lunar

Anorthosites? *Lunar and Planetary Science X* 167–168.

Collerson, K.D., Jesseau, C.W., Bridgwater, D.D. (1976) Crustal development of the Archean gneiss complex: eastern Labrador. In: Windley, B.F. (ed.) *The Early History of the Earth*. Wiley, New York.

Danyushevsky, L.V., Carroll, M.R., Falloon, T.J. (1997) ORIGIN OF HIGH-An PLAGIOCLASE IN TONGAN HIGH-Ca BONINITES: IMPLICATIONS FOR PLAGIOCLASE-MELT EQUILIBRIA AT LOW P(H 20). *The Canadian Mineralogist* 35, 313–326.

De Wit, M.J., Ashwal, L.D. (1997) *Greenstone Belts*. Oxford University Press, Oxford.

Dymek, R.F., Owens, B.E. (2001) Chemical assembly of Archean anorthosites from amphibolite- and granulite-facies terranes, SW Greenland. *Contributions to Mineralogy and Petrology* 141, 513–528.

Fan, J., Kerrich, R. (1997) Geochemical characteristics of aluminum depleted and undepleted komatiites and HREE-enriched low-Ti tholeiites, western Abitibi greenstone belt: A heterogeneous mantle plume-convergent margin environment. *Geochimica et Cosmochimica Acta* 61, 4723–4744.

Fram, M.S., Longhi, J. (1992) Phase equilibria of dikes associated with Proterozoic anorthosite complexes. *American Mineralogist* 77, 605–616.

Francis, D.M., Hynes, A.J. (1979) Komatiite-Derived Tholeiites in the Proterozoic of New Quebec. *Earth and Planetary Science Letters* 44, 473–481.

Garson, M.S., Livingstone, A. (1973) Is the South Harris Complex in North Scotland a Precambrian Overthrust Slice of Oceanic Crust and Island Arc. *Nat. Phys. Sci.* 241, 20.

Grove, T.L., Parman, S.W. (2004) Thermal evolution of the Earth as recorded by komatiites. *Earth and Planetary Science Letters* 219, 173–187.

Gualda, G.A.R., Ghiorso, M.S. (2015) MELTS_Excel: A Microsoft Excel-based MELTS interface for research and teaching of magma properties and evolution. *Geochemistry, Geophysics, Geosystems* 16, 1–10.

Hansen, H., Gronvold, K. (2000) Plagioclase ultraphyric basalts in Iceland : the mush of the rift. *Journal of Volcanology and Geothermal Research* 98, 1–32.

Hawkesworth, C.J., Gallagher, K., Hergt, J.M., McDermott, F. (1993) Mantle and Slab Contributions in Arc Magams. *Annual Review of Earth and Planetary Sciences* 21, 175–204.

Hellevang, B., Pedersen, R.B. (2008) Magma Ascent and Crustal Accretion at Ultraslow-Spreading Ridges: Constraints from Plagioclase Ultraphyric Basalts from the Arctic Mid-Ocean Ridge. *Journal of Petrology* 49, 267–294.

Herzberg, C. (1992) Depth and degree of melting of komatiites. *Journal of Geophysical Research* 97, 4521–4540.

Herzberg, C., Asimow, P.D., Arndt, N., Niu, Y., Lesher, C.M., Fitton, J.G., Cheadle, M.J., Saunders, A.D. (2007) Temperatures in ambient mantle and plumes: Constraints from basalts, picrites, and komatiites. *Geochemistry, Geophysics, Geosystems* 8.

Hill, C.M. (2017) Experimental Constraints on Crustal Contamination in Proterozoic Anorthosite Petrogenesis. University of the Witswatersrand.

Hoffmann, J.E., Svahnberg, H., Piazolo, S., Scherstén, A., Münker, C. (2012) The geodynamic evolution of Mesoarchean anorthosite complexes inferred from the Naajat Kuuat Complex , southern West Greenland. *Precambrian Research*. Elsevier B.V. 196–197, 149–170.

Housh, T.B., Luhr, J.F. (1991) Plagioclase-melt equilibria in hydrous systems. *American Mineralogist* 76, 477–492.

Kerrich, R., Wyman, D., Fan, J., Bleeker, W. (1998) Boninite series: low Ti-tholeiite associations from the 2.7 Ga Abitibi greenstone belt. *Earth and Planetary Science Letters* 164, 303–316.

Kimata, M., Nishida, N., Masahiro, S., Saito, S., Matsui, T., Arakawa, Y. (1995) Anorthite megacrysts from island arc basalts. *Mineralogical Magazine* 59, 1–14.

Kinzler, R.J., Grove, T.L. (1985) Crystallization and differentiation of Archean komatiite lavas from northeast Ontario: phase equilibrium and kinetic studies. *American Mineralogist* 70, 40–51.

Komor, S.C., Elthon, D.O.N. (1990) Formation of Anorthosite-Gabbro Rhythmic Phase Layering: An Example at North Arm Mountain , Bay of Islands Ophiolite. *Journal of Petrology* 31, 1–50.

Kushiro, I. (1980) Viscosity, density, and structure of silicate melts at high pressures, and their petrological applications. In: Hargraves, R.B. (ed.) *Physics of Magmatic Processes.* Princeton University Press, Princeton, New Jersey, 93–120.

Longhi, J., Ashwal, L.D. (1985) Two-Stage Models for Lunar and Terrestrial Anorthosites: Petrogenesis Without a Magma Ocean. *Proceedings of the 15th Lunar and Planetary Science Conference* 90.

McGregor, V.R., Nutman, A.P., Friend, C.R.L. (1985) The Archean Geology of the Godthåbsfjord Region, Southern West Greenland. *Workshop on Early Crustal Genesis: The World's Oldest Rocks.*

Mohan, M.R., Satyanarayanan, M., Santosh, M., Sylvester, P.J., Tubrett, M., Lam, R. (2013) Neoarchean suprasubduction zone arc magmatism in southern India : Geochemistry , zircon U-Pb geochronology and Hf isotopes of the Sittampundi Anorthosite Complex. *Gondwana Research*. International Association for Gondwana Research 23, 539–557.

Myers, J.S. (1985) *Stratigraphy and and structure of the Fiskenaesset Complex, West Greenland*. Grønlands geologiske undersøgelse.

Parman, S.W., Dann, J.C., Grove, T.L., De Wit, M.J. (1997) Emplacement conditions of

komatiite magmas from the 3.49 Ga. *Earth and Planetary Science Letters* 150, 303–323.

Parman, S.W., Grove, T.L., Dann, J.C. (2001) The production of Barberton komatiites in an Archean Subduction Zone. *Geophysical Research Letters* 28, 2513–2516.

Parman, S.W., Grove, T.L., Wit, M.J. de (2002) Komatiites: the subduction perspective. *Geochimica et Cosmochimica Acta* 66.

Peck, W.H., Clechenko, C.C., Hamilton, M.A., Valley, J.W. (2010) OXYGEN ISOTOPES IN THE GRENVILLE AND NAIN AMCG SUITES: REGIONAL ASPECTS OF THE CRUSTAL COMPONENT IN MASSIF ANORTHOSITES. *The Canadian Mineralogist* 48, 763–786.

Peck, W.H., Valley, J.W. (1996) The Fiskenaesset Anorthosite Complex: Stable isotope evidence for shallow emplacement into Archean ocean crust. *Geology* 24, 523–526.

Phinney, W.C., Halls, H.C. (2001) Petrogenesis of the Early Proterozoic Matachewan dyke swarm, Canada, and implications for magma emplacement and subsequent deformation. *Canadian Journal of Earth Science* 1563, 1541–1563.

Phinney, W.C., Morrison, D.A., Ashwal, L.D., Cochran, A. (1979) Anorthosite Inclusions in Northeastern Minnesota: Remntants of Early Terrestrial Crust? *Proceedings of the 10th Lunar and Planetary Science Conference* 978–980.

Phinney, W.C., Morrison, D.A., David, E. (1988) Anorthosites and Related Megacrystic Units in the Evolution of Archean Crust. *Journal of Petrology* 29, 1283–1323.

Poidevin, J. (1994) Premmbriun Resenrth Boninite-like rocks from the Palaeoproterozoic greenstone belt of Bogoin, Central African Republic: geochemistry and petrogenesis. *Precambrian Research* 68, 97–113.

Polat, A., Appel, P.W.U., Fryer, B., Windley, B., Frei, R., Samson, I.M., Huang, H. (2009) Trace element systematics of the Neoarchean Fiskenæsset anorthosite complex and associated

meta-volcanic rocks , SW Greenland : Evidence for a magmatic arc origin. *Precambrian Research* 175, 87–115.

Polat, A., Fryer, B.J., Appel, P.W.U., Kalvig, P., Kerrich, R., Dilek, Y., Yang, Z. (2011) Geochemistry of anorthositic differentiated sills in the Archean (~2970Ma) Fiskenæsset Complex, SW Greenland: Implications for parental magma compositions, geodynamic setting, and secular heat flow in arcs. *Lithos*. Elsevier B.V. 123, 50–72.

Rollinson, H. (1995) Composition and tectonic settings of chromite deposits through time-A discussion. *Economic Geology* 90, 2091–2092.

Rollinson, H., Appel, P.W.U., Frei, R. (2002) A Metamorphosed, Early Archean Chromitite from West Greenland: Implications for the Genesis of Archean Anorthositic Chromitites. *Journal of Petrology* 43, 2143–2170.

Rollinson, H., Reid, C., Windley, B. (2010) Chromitites from the Fiskenæsset anorthositic complex, West Greenland: clues to late Archaean mantle processes. In: Kusky, T.M., Zhai, M.-G., Xiao, W. (eds) *The Evolving Continents: Understanding Processes of Continental Growth*. Geological Society, London, 197–212.

Sheth, H. (2016) Giant plagioclase basalts: Continental flood basalt–induced remobilization of anorthositic mushes in a deep crustal sill complex. *GSA Bulletin* 128, 916–925.

Sisson, T.W., Grove, T.L. (1993) Experimental investigations of the role of H2O in calc-alkaline differentiation and subduction zone magmatism. *Contributions to Mineralogy and Petrology* 113, 143–166.

Sobolev, A. V., Asafov, E. V., Gurenko, A.A., Arndt, N.T., Batanova, V.G., Portnyagin, M. V., Garbe-Schönberg, D., Krasheninnikov, S.P. (2016) Komatiites reveal a hydrous Archaean deep-mantle reservoir. *Nature*. Nature Publishing Group 531, 628–632.

Sobolev, A. V., Asafov, E. V., Gurenko, A.A., Arndt, N.T., Batanova, V.G., Portnyagin, M. V.,

Garbe-Schönberg, D., Wilson, A.H., Byerly, G.R. (2019) Deep hydrous mantle reservoir provides evidence for crustal recycling before 3.3 billion years ago. *Nature*. Springer US 571, 555–559.

Sobolev, A. V., Danyushevsky, L. V. (1994) Petrology and geochemistry of boninites from the north termination of the Tonga trench: Constraints on the generation conditions of primary high-ca boninite magmas. *Journal of Petrology* 35, 1183–1211.

Stern, R.J., Bloomer, S.H. (1992) Subduction zone infancy: Examples from the Eocene Izu-Bonin-Mariana and Jurassic California arcs. *GSA B* 104, 1621–1636.

Stroup, J.B., Fox, P.J. (1981) Geologic Investigations in the Cayman Trough: Evidence for Thing Oceanic Crust Along the Mid-Cayman Rise. *The Journal of Geology* 89, 395–420.

Thy, P. (1995) Low-Pressure Experimental Constraints on the Evolution of Komatiites. *Journal of Petrology* 36, 1529–1548.

Weaver, L., Tarney, J., Windley, B. (1981) Geochemistry and petrogenesis of the Fiskenaesset anorthosite complex , southern West Greenland : nature of the parent magma. *Geochimica et Cosmochimica Acta* 45, 711–725.

Wilson, A.H. (2003) A new class of silica enriched, highly depleted komatiites in the southern Kaapvaal Craton, South Africa. *Precambrian Research* 127, 125–141.

Windley, B.F., Garde, A.A. (2009) Earth-Science Reviews Arc-generated blocks with crustal sections in the North Atlantic craton of West Greenland : Crustal growth in the Archean with modern analogues. *Earth Science Reviews*. Elsevier B.V. 93, 1–30.

Zhou, S., Polat, A., Longstaffe, F.J., Yang, K., Brian, J., Weisener, C. (2015) Formation of the Neoarchean Bad Vermilion Lake. *Gondwana Research*. Elsevier B.V.

Figure 1 Estimated bulk composition (whole rock) of Archean anorthosites including Fiskenaesset (black circle and green triangles), Messina (orange dash), Bad Vermillion Lake (grey cross), Shawmere (yellow star), Sittampundi (blue x), Buksefjorden (blue diamonds), and Nordland (red squares). Data for Fiskenaesset (black circle), Messina, Bad Vermillion Lake, Shawmere, and Sittampundi from Ashwal (1993). Data for Fiskenaesset (green triangles) from Polat *et al.* (2011). Data for Buksefjorden and Nordland from Dymek and Owens (2001).

Figure 2 Anorthite content of plagioclase for primordial (Lunar), megacrystic (Archean), and massif-type (Proterozoic) anorthosites as a function of age. Megacrystic anorthosites are restricted to the Archean, and the composition of anorthosites abruptly changes to the lower An content of Proterozoic massif-type anorthosites. Also shown is a kernel density estimate of komatiite occurrences as a function of age, where the vertical axis represents the probability of a komatiite existing at the given time. A substantial portion of the observed komatiites formed at the same time as the Archean megacrystic anorthosites, indicating a possible connection. Data for anorthosites and komatiites from Ashwal (2010) and de Wit and Ashwal (1997), respectively.

Figure 3 Anorthite content of plagioclase crystallizing from a komatiitic basalt composition at low pressures as a function of temperature, degree of melting, and the abundance of plagioclase. Data from Thy (1995).

Figure 4 Anorthite content of plagioclase from Archean anorthosite systems as a function of **a** CaO/Na_2O ratio and **b** Al_2O_3/SiO_2 ratio. The An# of crystallizing plagioclase increases with increasing Ca/Na and Al/Si ratios. Data as in Figure 1.

Figure 5 Composition of chromites from **a** modern igneous systems and **b** Archean igneous systems. Note the distinct fields defined by anorthosites in both modern and Archean rocks. Data from Rollinson *et al.* (2002).

Figure 6 Compilation of all available data for komatiites from **a** Abitibi and **b** Barberton collated from the GEOROC database. The red arrows represent the olivine fractionation trends used to correct for possible alteration and identify the bulk composition used (red star).

Figure 7 Model results for the Abitibi corrected starting composition with **a, b** 0 and **c, d** 1 wt% H_2O at 1 kbar. **a** Crystallization of the bulk komatiitic composition results in the formation of roughly 50% olivine. Opx and cpx subsequently crystallize simultaneously with plag and undergo a complex series of resorptions over a 50 °C range. The composition of the liquid at plag-in, marked by the arrow, is used for the residual liquid **b** Crystallization of residual liquid after fractionation at the temperature where plagioclase first forms. Plagioclase rapidly crystallizes from the residual liquid, accounting for as much as 50% of the mass of the liquid **c** Crystallization of the bulk komatiitic composition results in the formation of roughly 50% olivine, followed by clinopyroxene and orthopyroxene. At 1060 °C (marked by the arrow along the horizontal axis), plagioclase starts crystallizing. **d** Crystallization of residual liquid after fractionation at the temperature where plagioclase first forms. Plagioclase rapidly crystallizes from the residual liquid, accounting for as much as 50% of the mass of the liquid, with the remainder being broadly basaltic. Note that the initial 1 wt% H_2O increases as crystallization proceeds (See Figs. 9, 11). Crystallization paths for the Barberton compositions is shown in Supplementary Figure 1.

Figure 8 Estimated bulk composition of Archean anorthosites and modelled remaining liquids at plagioclase saturation for Abitibi (orange stars) and Barberton (black stars) under dry (filled stars) and hydrous (open stars) conditions. For Na, the modelled compositions bracket the natural samples, and for Ca they are at or below the minima for their MgO contents. The composition of the liquids is at distinctly higher Ti and H_2O contents than natural samples. Conversely, the Fe and Al contents are lower in the modelled compositions. Natural data as in Fig 1.

Figure 9 Degree of melt remaining as a function of temperature for the initial compositions of Abitibi (orange) and Barberton (black). Dashed lines indicate hydrous models (1 wt% H_2O initial). For komatiitic compositions, the slope dF/dT changes sharply first at cpx-in, and then at plag-in.

Figure 10 Variation of **a** Al/Si ratio, **b** Ca/Na ratio, **c** An#, and **d** H_2O concentration as a function of the melt fraction. Symbols as in Figure 9.

Figure 11 Variation of **a** Al/Si ratio, **b** Ca/Na ratio, **c** An#, and **d** H_2O concentration as a function of the melt fraction for the remaining fractionated liquid compositions of Abitibi (orange), Barberton (black), and the bulk HAB composition (blue). Dashed lines indicate hydrous models (1 wt% H_2O initial). The HAB composition is initially nearly saturated in plagioclase and thus presented without a fractionation event. Note, komatiitic fractionated liquid compositions which appear to first crystallize plagioclase at $F < 1$ are the result of crystallization of a substantial mass of solids within the first 5 °C temperature step.

Figure 12 Degree of melt remaining as a function of temperature for model runs using the composition of the remaining liquid at plag-in. Symbols as in Figure 11.

Figure 13 Composition of spinel-group minerals (e.g., chromite) crystallizing from the initial komatiitic composition compared to the composition of chromites from **a** modern igneous systems and **b** Archean igneous systems. As plagioclase continues to crystallize, the chromite composition approaches that previously identified for Archean anorthosites. Symbols as in Fig. 8. Data from Rollinson *et al.* (2002).

Figure 14 Composition of spinel-group minerals (e.g., chromite) crystallizing from the remaining liquid composition separated from the solids at plag-in compared to the composition of chromites from **a** modern igneous systems and **b** Archean igneous systems. As these compositions continue to crystallize, the chromite composition follows the trend previously identified in the Fiskenaesset Archean anorthosite. Symbols as in Fig. 8. Data from Rollinson *et al.* (2002).

Figure 15 Composition of the modelled (**a, b**) komatiitic melt and **(c, d**) remaining liquids versus the equilibrium plagioclase compared with the compositions of bulk anorthosites. The enlarged symbols for Fiskenaesset (black circle), Messina (orange open square), and Bad Vermillion Lake (grey cross) represent estimated parental melt compositions (Ashwal, 1993) and have lower An# with similar Ca/Na ratios and lower Al/Si ratios. Other symbols as in Fig. 1. Lines of modelled composition as in Fig. 11.

Figure 16 Schematic diagram of the formation environment of Archean megacrystic anorthosites. At relatively shallow depths, komatiitic melts become trapped and start crystallizing. The dense

olivine and pyroxenes which crystallize are gravitationally segregated, while the remaining liquid becomes enriched in aluminum and calcium. After 70 to 90 % crystallization, the liquid becomes saturated in plagioclase. The neutrally buoyant plagioclase is subsequently entrained in the basaltic liquid as it escapes the magma chamber and becomes emplaced in the crust, typically as sills or dikes.

Table 1 Corrected starting compositions for komatiites and high-Al basalt. Composition of komatiites from Arndt (2008) and corrected based on all data for the region collated by GEOROC. Composition of HAB from Hill (2017).

	Abitibi	Barberton	HAB
SiO_2	45.90	47.70	48.55
TiO_2	0.33	0.36	0.84
Al_2O_3	6.49	4.15	17.44
Cr_2O_3	0.38	0.38	0
FeOT	10.80	11.20	10.88
MnO	0.19	0.19	0.09
MgO	29.20	28.50	9.33
NiO	0.18	0.20	0
CaO	6.60	7.20	9.06
Na_2O	0.68	0.50	2.35
K_2O	0.08	0.05	0.31
P_2O_5	0.03	0.03	0.17

Table 2 Composition of liquids separated from the system at plagioclase-in.

	Abitibi Dry	Abitibi Wet	Barberton Dry	Barberton Wet
SiO_2	50.56	55.85	52.80	59.26
TiO_2	1.00	0.77	1.50	0.61
Al_2O_3	15.78	16.35	14.91	15.22
Fe_2O_3	1.77	1.00	1.94	0.91
Cr_2O_3	0.06	0.06	0.04	0.04
FeO	6.83	3.60	7.00	2.96
MnO	0.19	0.18	0.21	0.22
MgO	9.74	6.57	7.60	4.61
NiO	0.03	0.02	0.03	0.03
CaO	13.05	11.42	10.51	8.38
Na_2O	0.63	0.66	2.92	3.40
K_2O	0.27	0.25	0.34	0.39
P_2O_5	0.10	0.10	0.20	0.23
H_2O	-	3.18	-	3.75

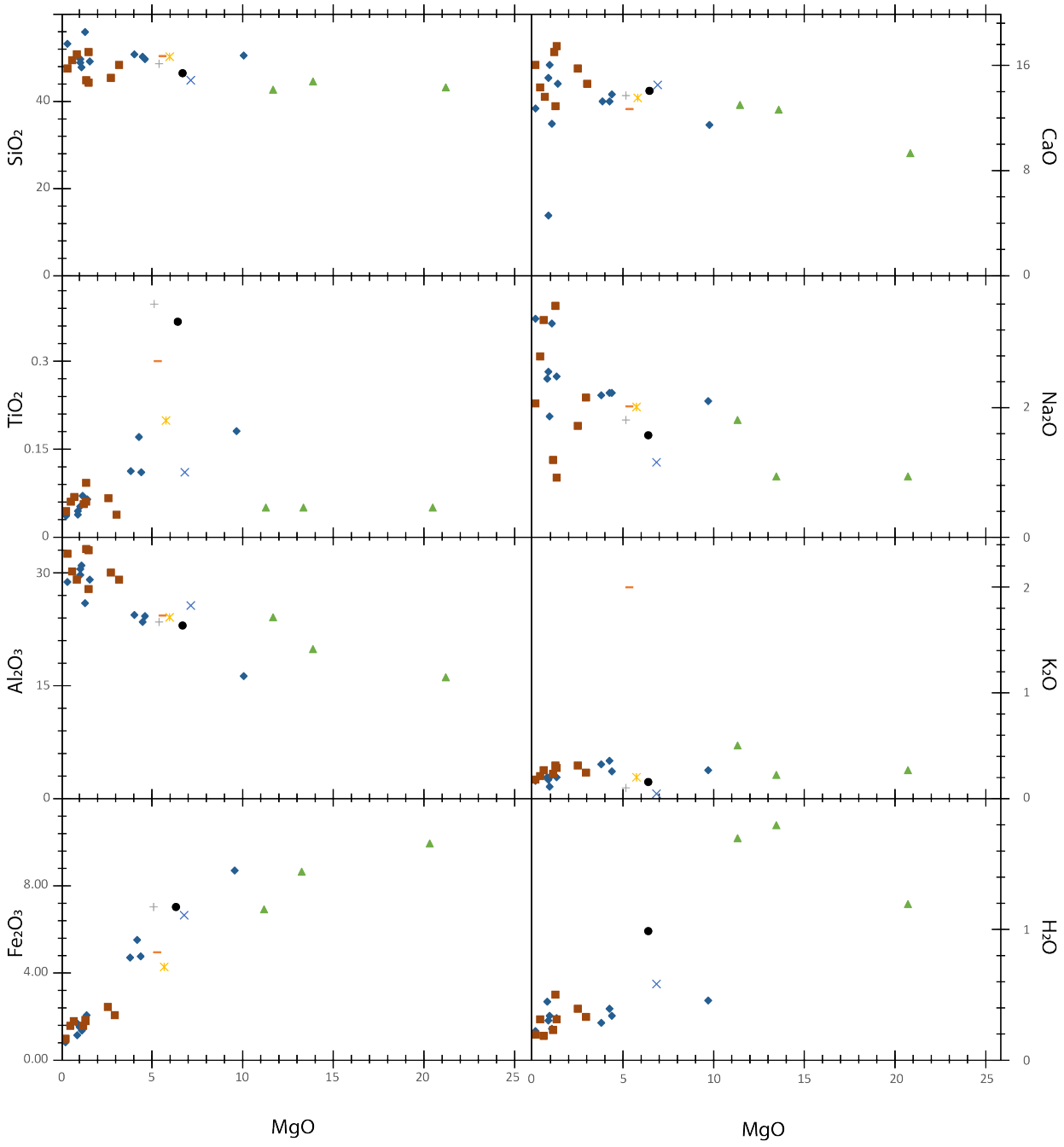

Figure 1

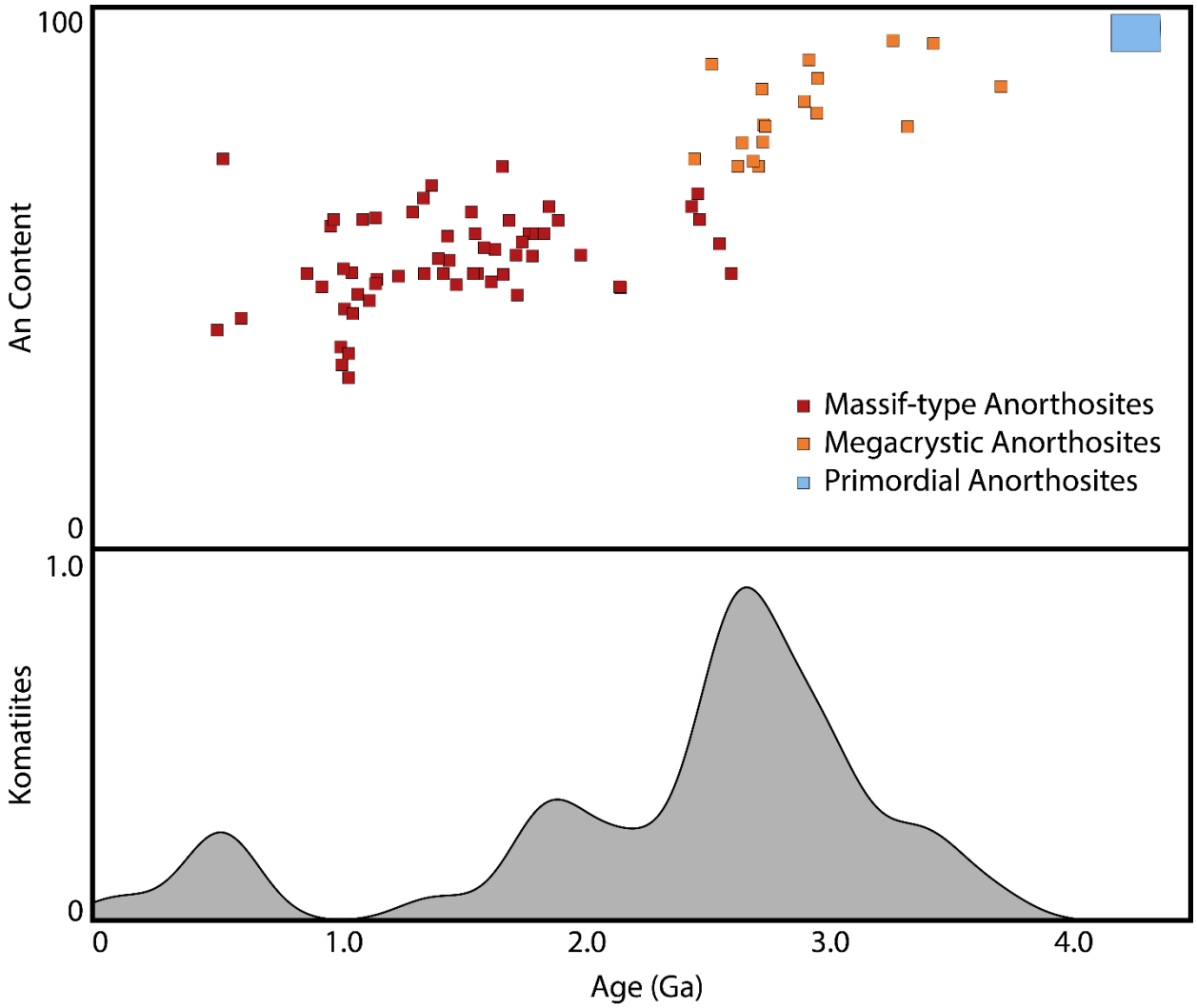
100
0
An Content
Massif-type Anorthosites
Megacrystic Anorthosites
Primordial Anorthosites
1.0
0
Komatiites
0
1.0
2.0
3.0
4.0
Age (Ga)

Figure 2

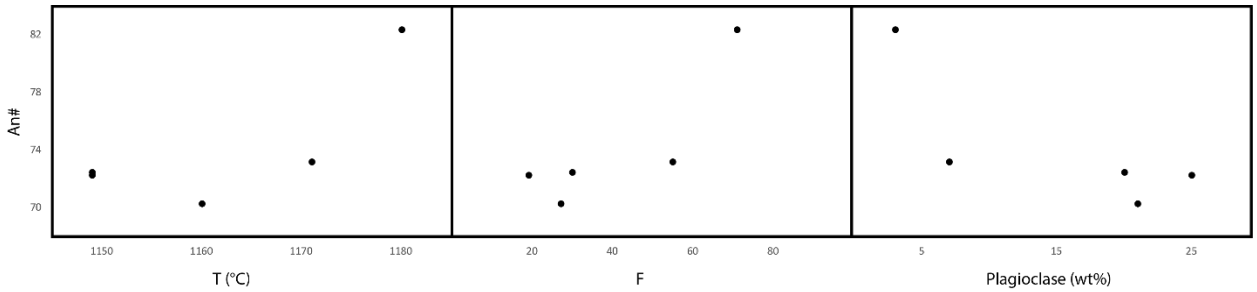
An#
82
78
74
70
1150
1160
1170
1180
T (°C)
20
40
60
80
F
5
15
25
Plagioclase (wt%)

Figure 3

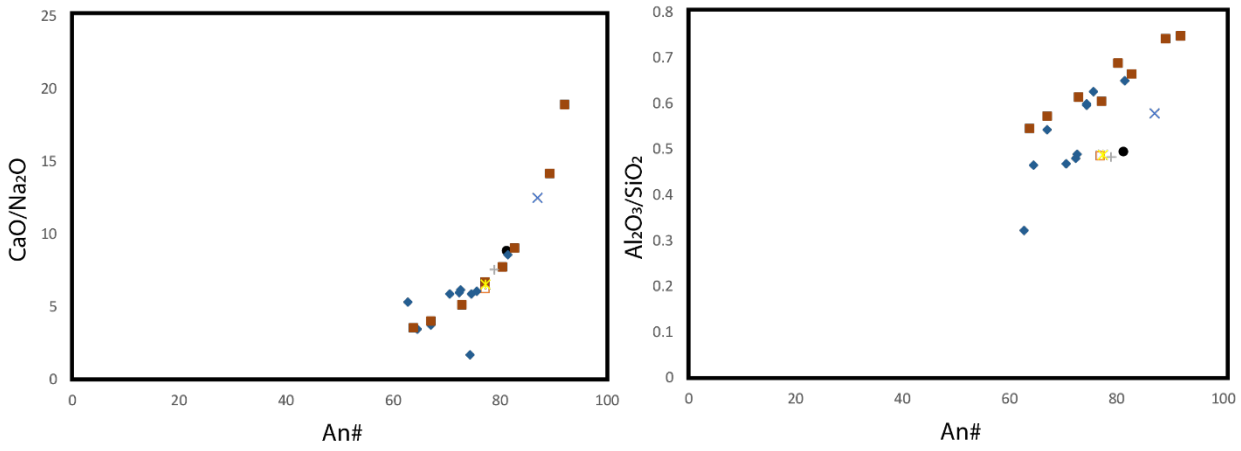
25
20
15
10
5
0
CaO/Na2O
0
20
40
60
80
100
An#
0.8
0.7
0.6
0.5
0.4
0.3
0.2
0.1
0
Al2O3/SiO2
0
20
40
60
80
100
An#

Figure 4

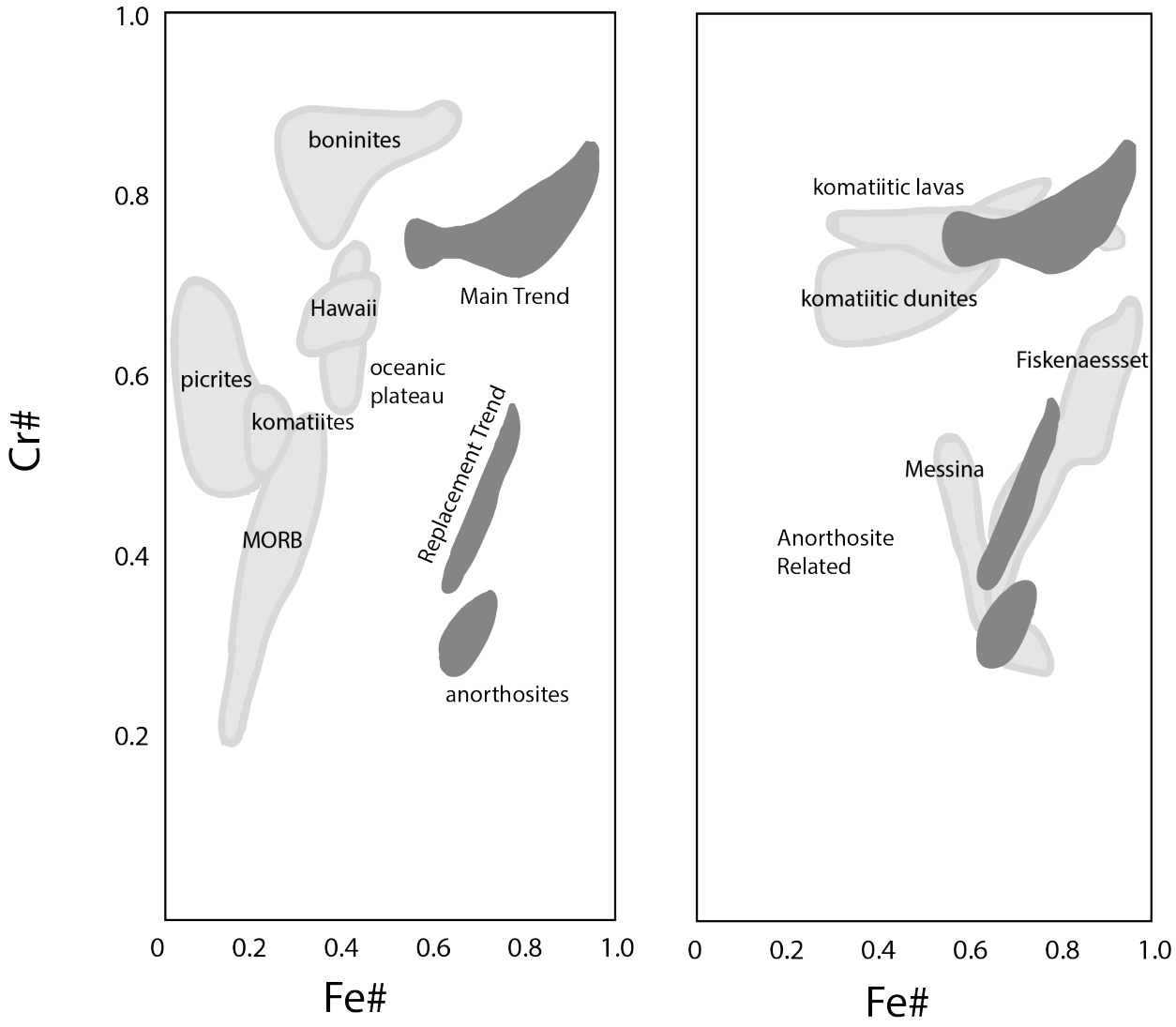
1.0
0.8
0.6
0.4
0.2
Cr#
boninites
Main Trend
Hawaii
oceanic
plateau
picrites
komatiites
MORB
Replacement Trend
anorthosites
0
0.2
0.4
0.6
0.8
1.0
Fe#
komatiitic lavas
komatiitic dunites
Fiskenaessset
Messina
Anorthosite
Related
0
0.2
0.4
0.6
0.8
1.0
Fe#

Figure 5

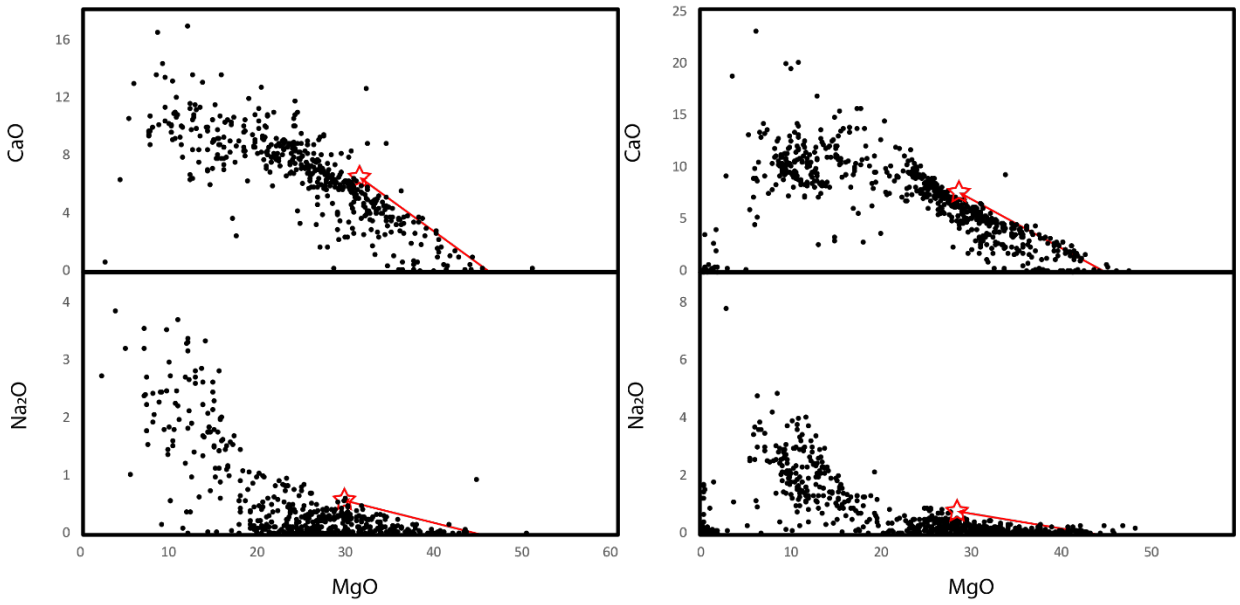

Figure 6

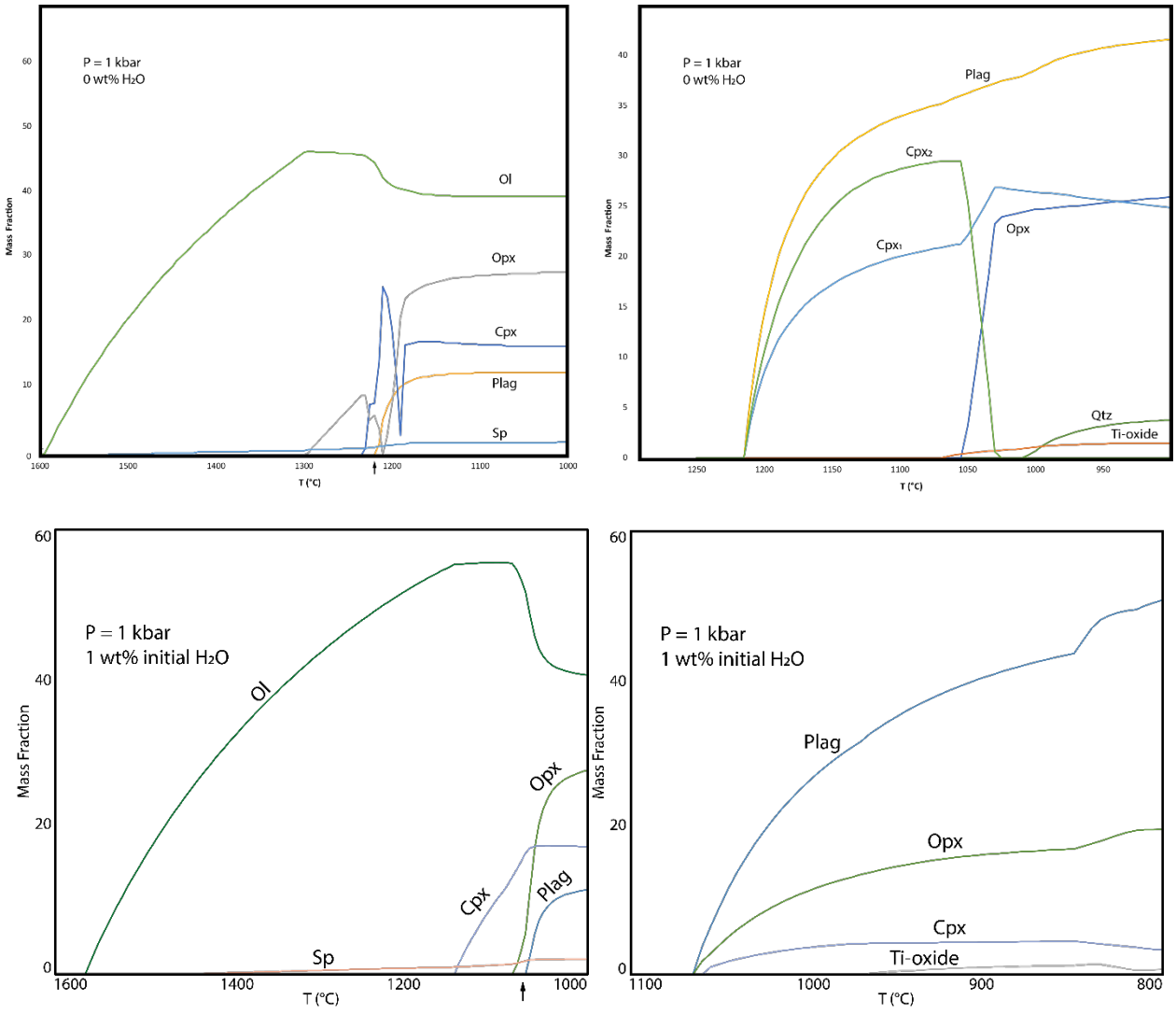
P = 1 kbar
0 wt% H2O
Ol
Opx
Cpx
Plag
Sp
Mass Fraction
T (°C)
P = 1 kbar
0 wt% H2O
Plag
Cpx2
Cpx1
Opx
Qtz
Ti-oxide
Mass Fraction
T (°C)
P = 1 kbar
1 wt% initial H2O
Ol
Opx
Cpx
Plag
Sp
Mass Fraction
T (°C)
P = 1 kbar
1 wt% initial H2O
Plag
Opx
Cpx
Ti-oxide
Mass Fraction
T (°C)

Figure 7

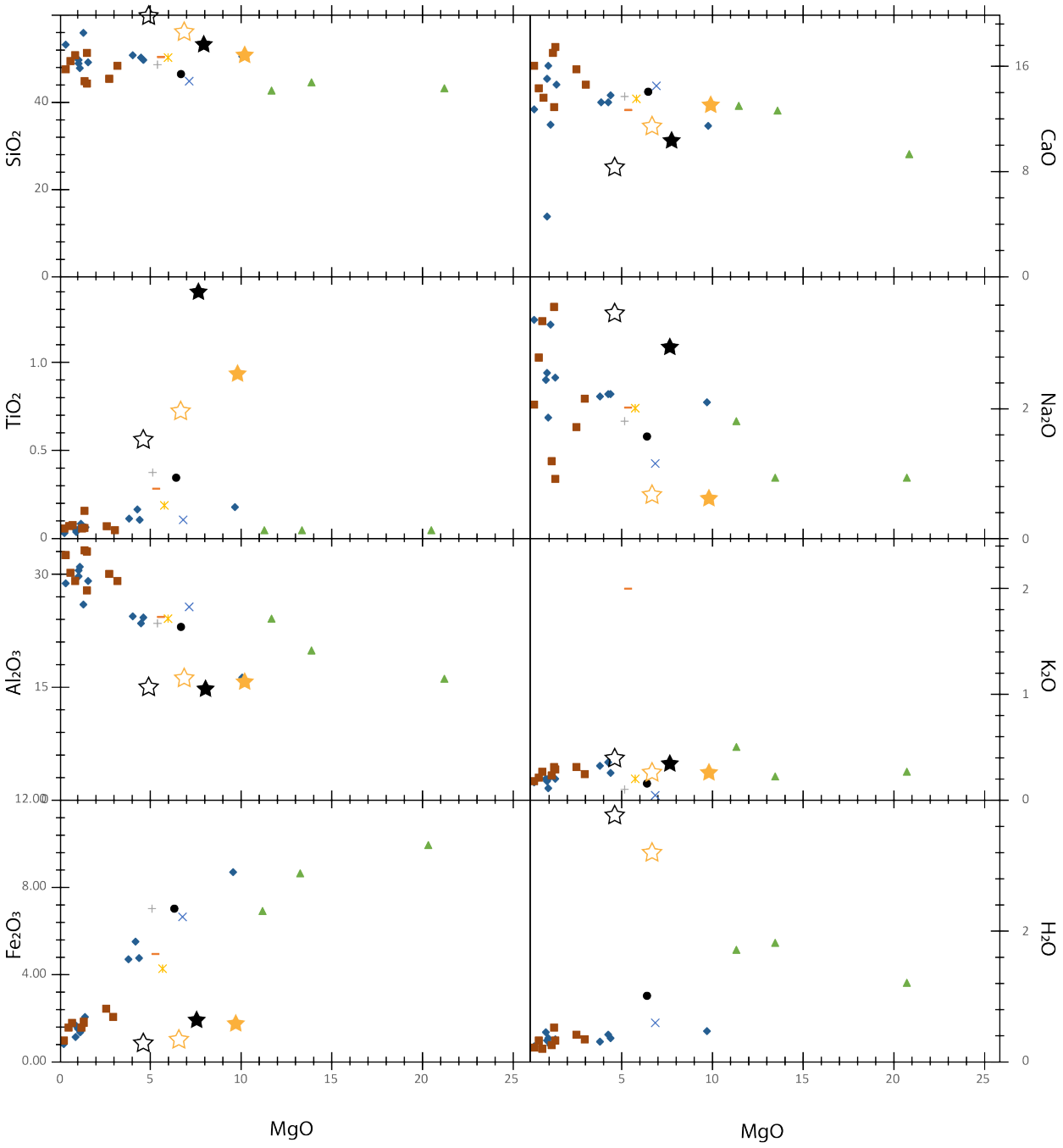

Figure 8

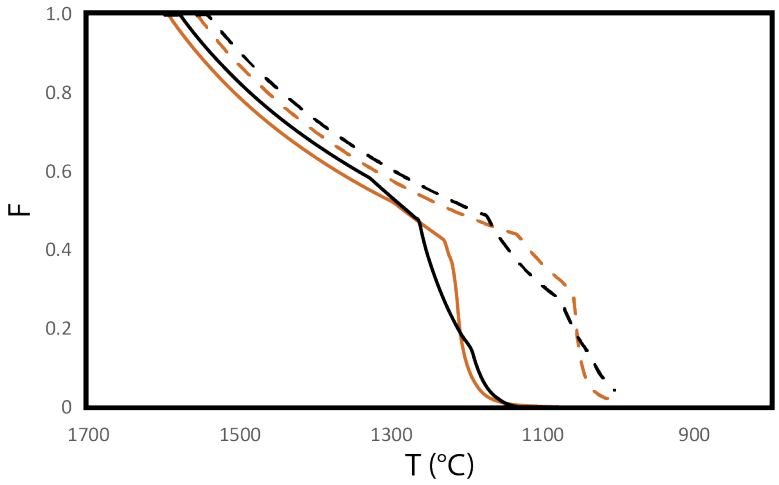

Figure 9

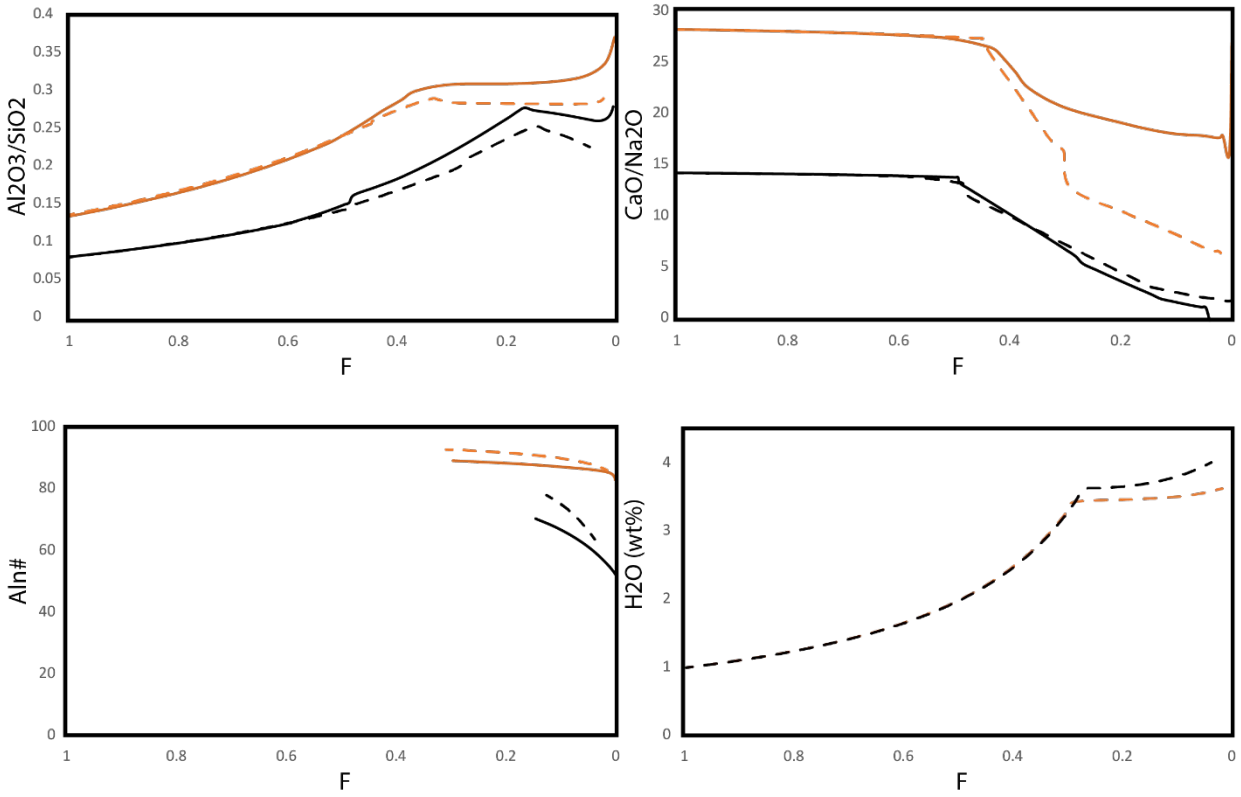

Figure 10

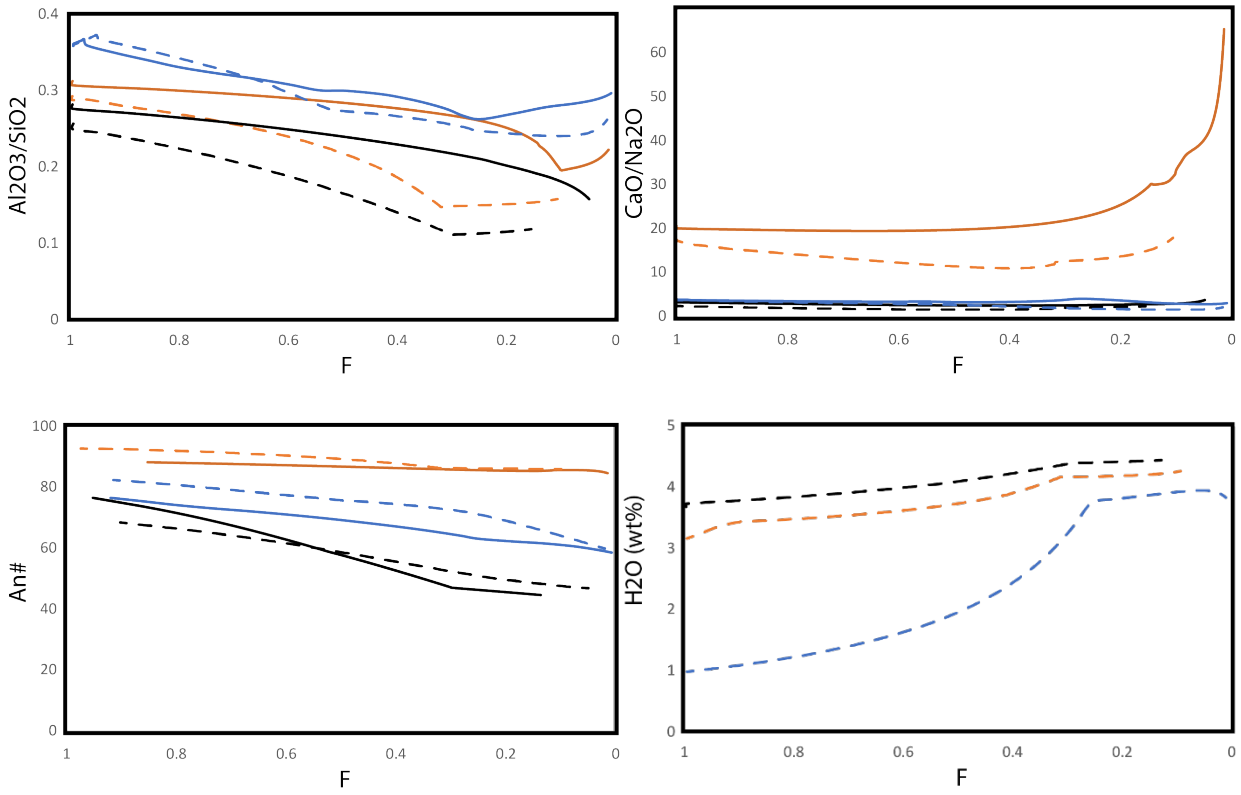
Al2O3/SiO2
0.4
0.3
0.2
0.1
0
1
0.8
0.6
0.4
0.2
0
F
CaO/Na2O
60
50
40
30
20
10
0
1
0.8
0.6
0.4
0.2
0
F
An#
100
80
60
40
20
0
1
0.8
0.6
0.4
0.2
0
F
H2O (wt%)
5
4
3
2
1
0
1
0.8
0.6
0.4
0.2
0
F

Figure 11

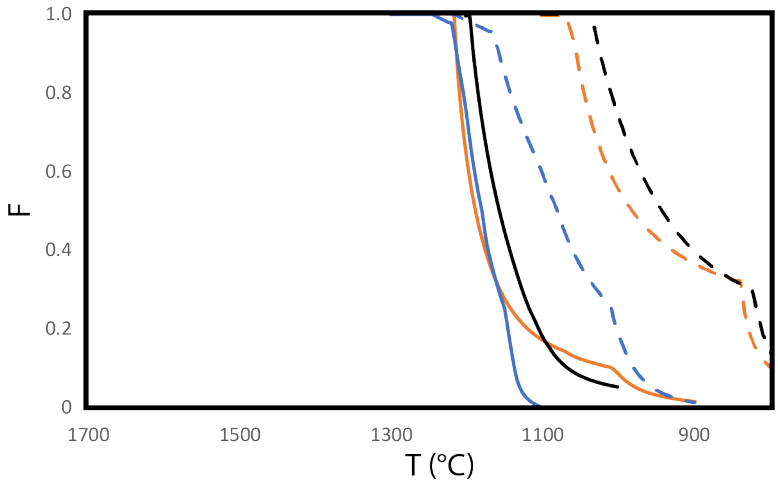

Figure 12

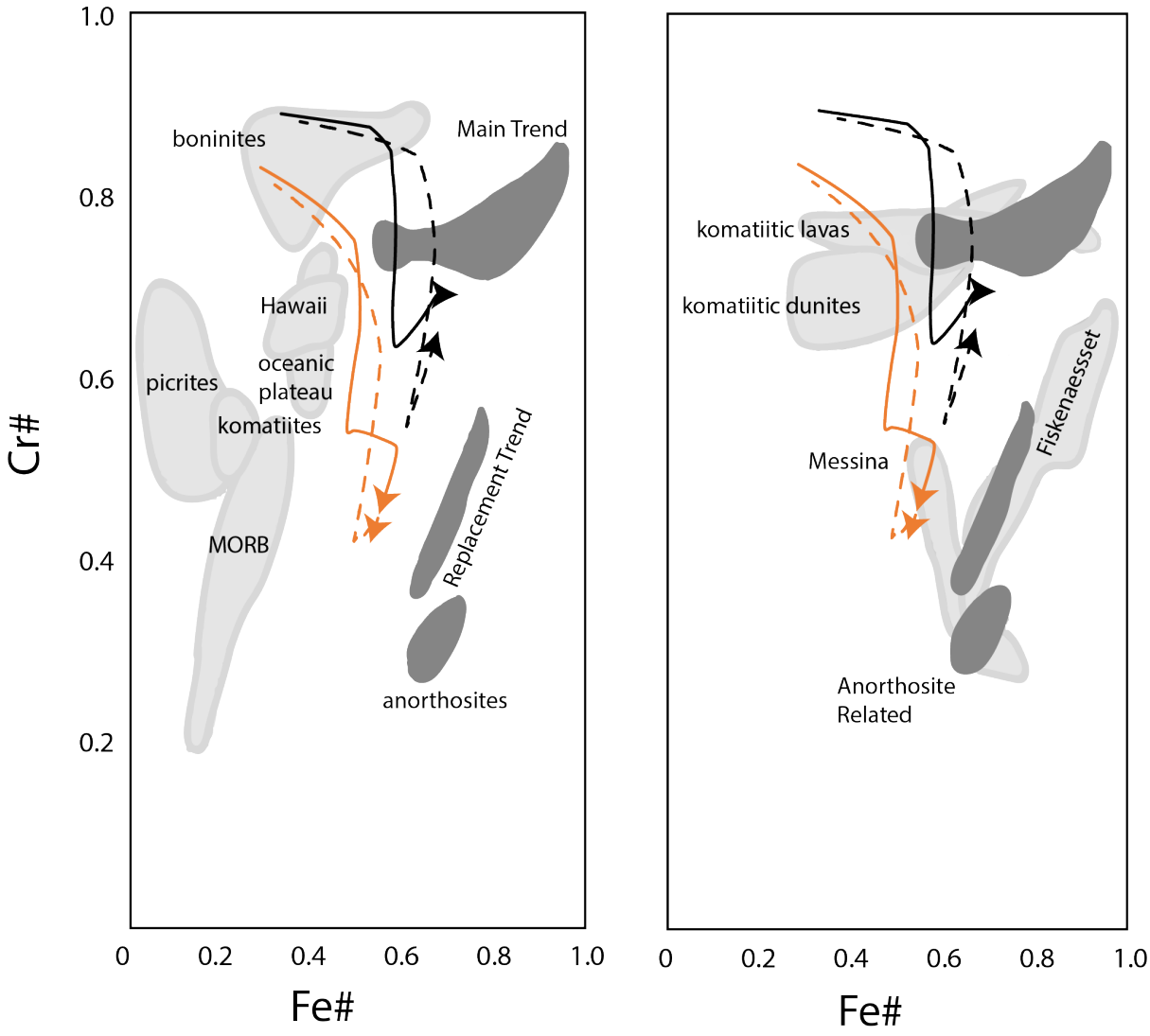
1.0
0.8
0.6
0.4
0.2
Cr#
boninites
Main Trend
Hawaii
oceanic
plateau
picrites
komatiites
MORB
Replacement Trend
anorthosites
0
0.2
0.4
0.6
0.8
1.0
Fe#
komatiitic lavas
komatiitic dunites
Messina
Fiskenaessset
Anorthosite
Related
0
0.2
0.4
0.6
0.8
1.0
Fe#

Figure 13

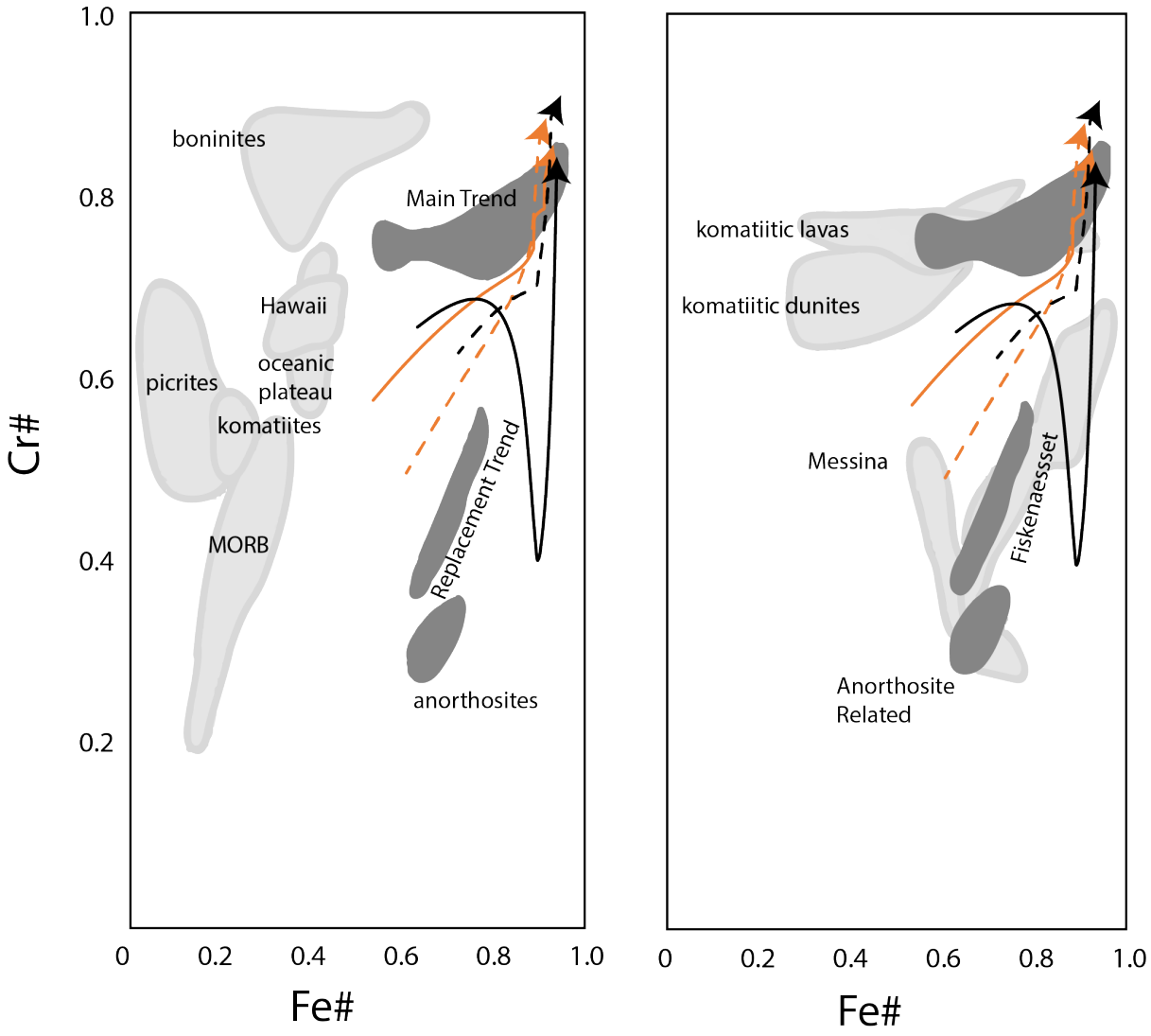
1.0
0.8
0.6
0.4
0.2
Cr#
boninites
Main Trend
Hawaii
oceanic
plateau
picrites
komatiites
MORB
Replacement Trend
anorthosites
0
0.2
0.4
0.6
0.8
1.0
Fe#
komatiitic lavas
komatiitic dunites
Messina
Fiskenaessset
Anorthosite
Related
0
0.2
0.4
0.6
0.8
1.0
Fe#

Figure 14

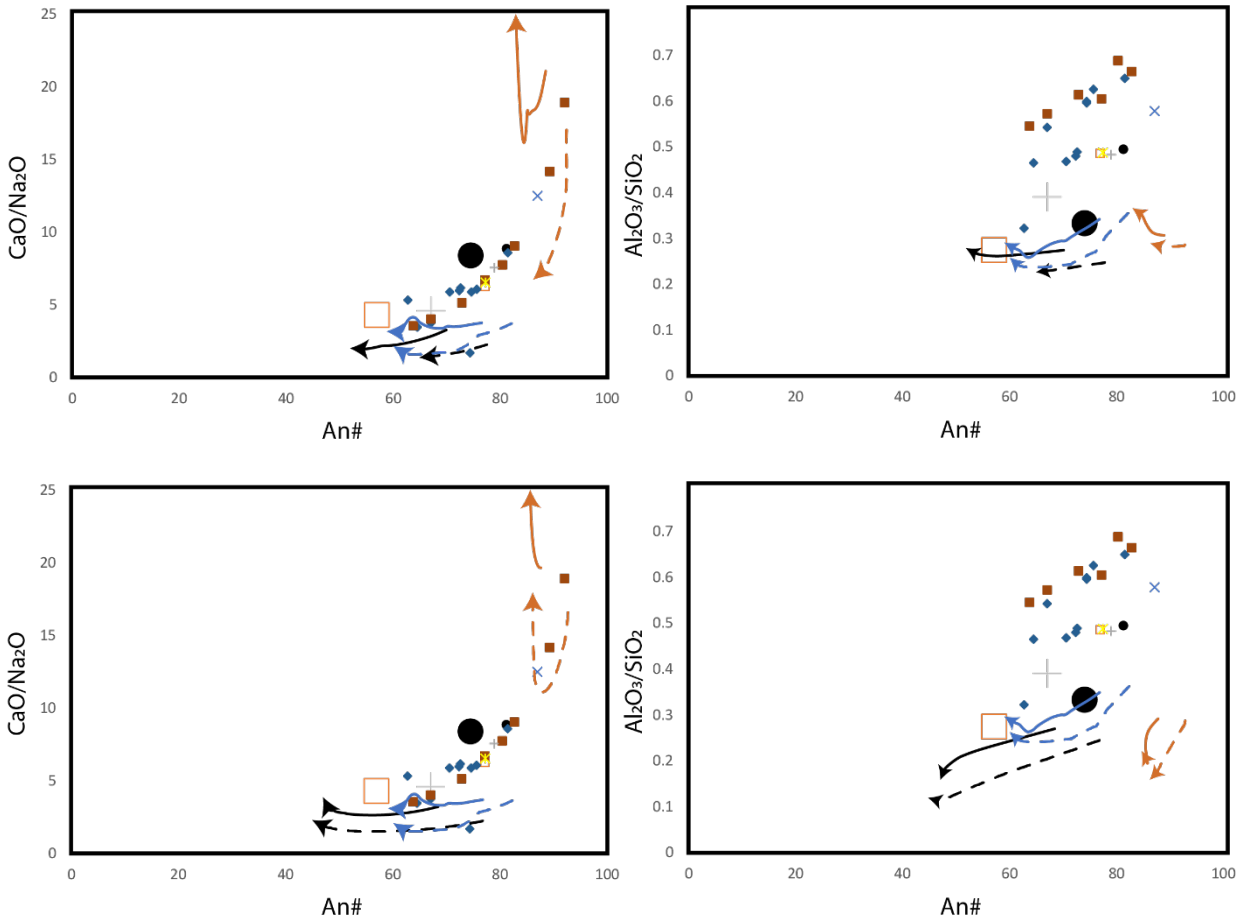
CaO/Na2O
Al2O3/SiO2
An#
0
5
10
15
20
25
0.1
0.2
0.3
0.4
0.5
0.6
0.7
0
20
40
60
80
100

Figure 15

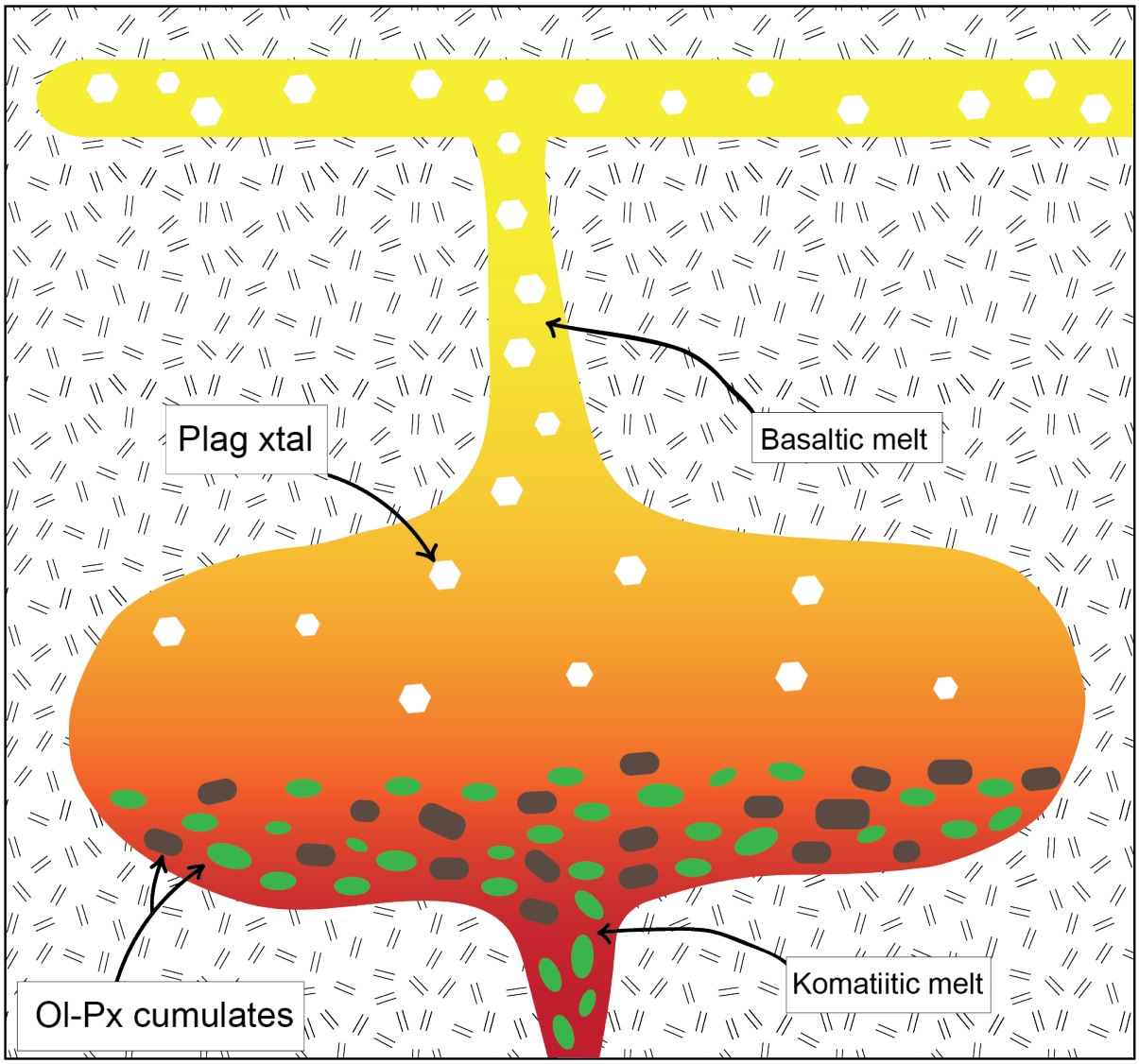

Figure 16

Supplementary Material

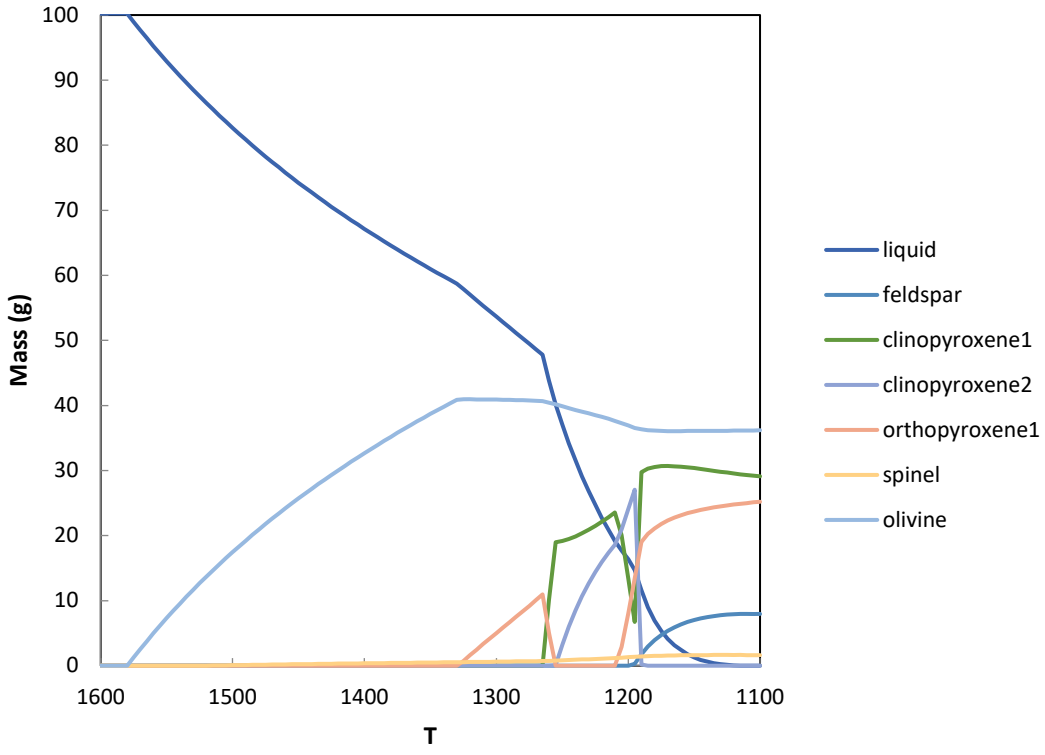

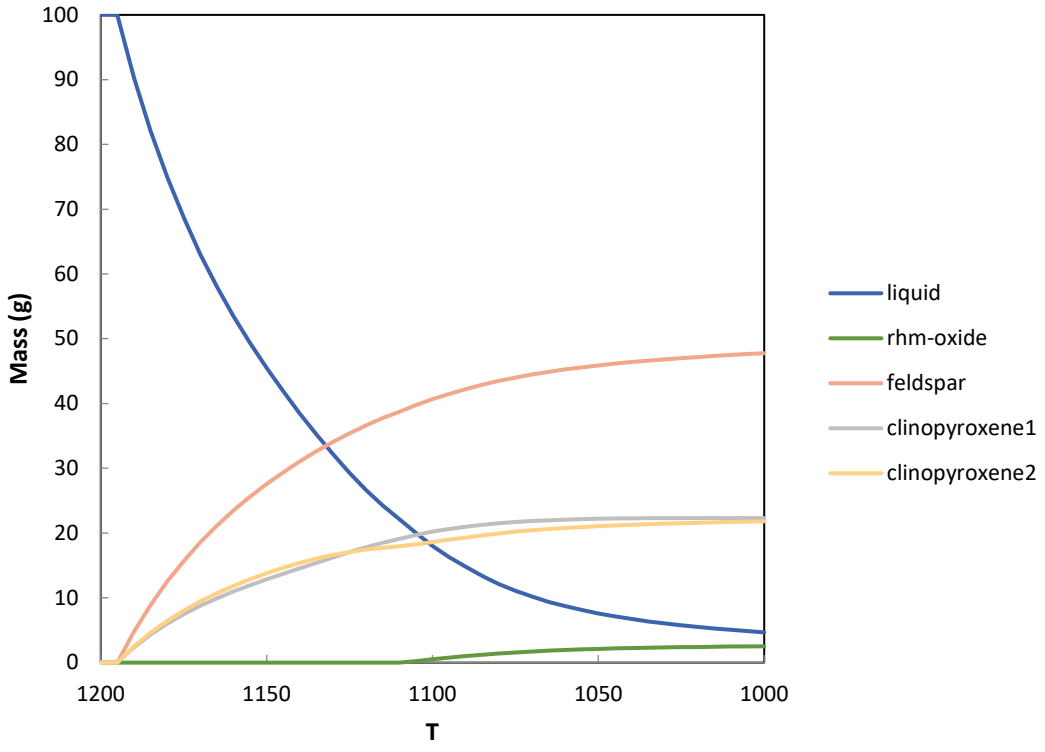

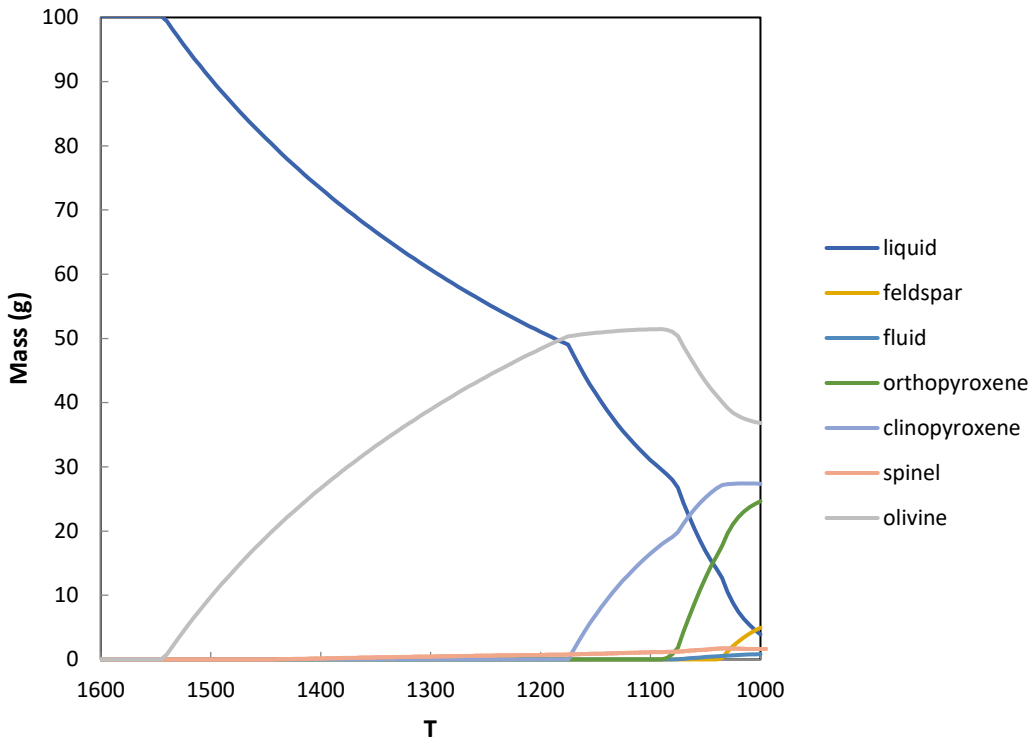
100
90
80
70
60
50
40
30
20
10
0
Mass (g)
1600
1500
1400
1300
1200
1100
1000
T
liquid
feldspar
fluid
orthopyroxene
clinopyroxene
spinel
olivine

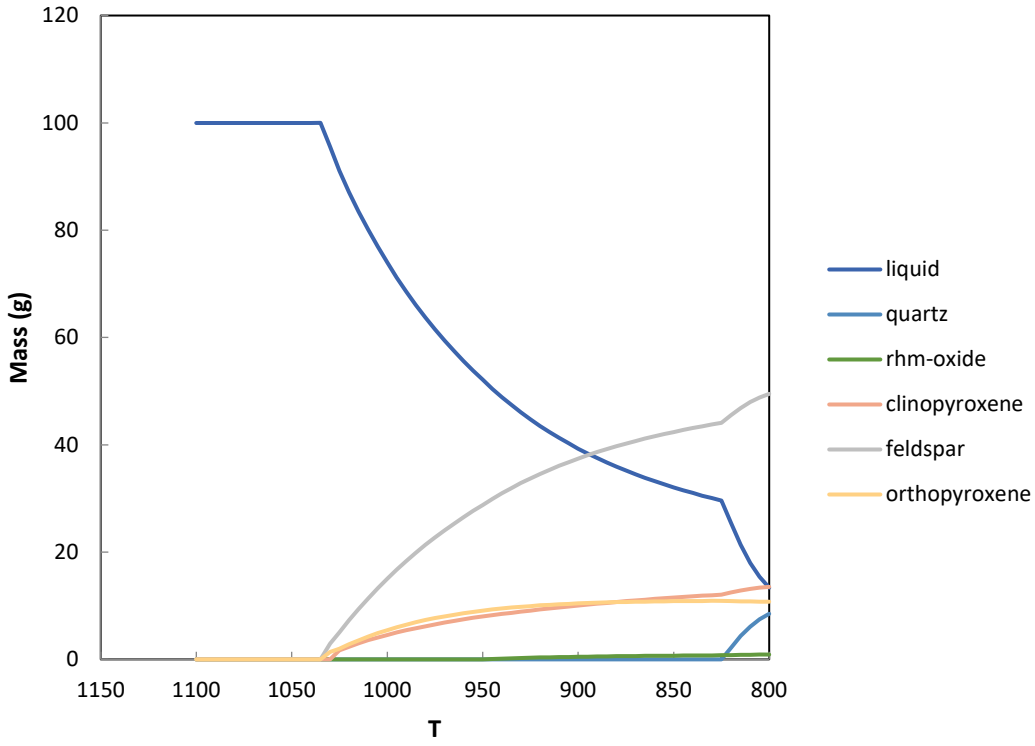
120
100
80
60
40
20
0
Mass (g)
1150
1100
1050
1000
950
900
850
800
T
liquid
quartz
rhm-oxide
clinopyroxene
feldspar
orthopyroxene

Supplementary Figure 1 Crystallization paths for **a** Barberton initial, dry komatiite, **b** Barberton dry residual liquid, **c** Barberton initial, wet komatiite, and **d** Barberton wet residual liquid at 1kbar and 0 or 1 initial wt% H_2O.

Supplementary Table 1 Estimated bulk composition of Archean anorthosites including Fiskenaesset, Messina, Bad Vermillion Lake, Shawmere, Sittampundi, Buksefjorden, and Nordland. Data for Fiskenaesset (bulk and parental), Messina (bulk and parental), Bad Vermillion Lake (bulk and parental), Shawmere (bulk), and Sittampundi (bulk) from Ashwal (1993). Data for Fiskenaesset (bulk) from Polat *et al.* (2011). Data for Buksefjorden (bulk) and Nordland (bulk) from Dymek and Owens (2001).

	Fiskenaesset		Messina		Bad Vermillion Lake		Shawmere	Sittampundi	Fiskenaesset		
	Bulk	Parent	Bulk	Parent	Bulk	Parent	Bulk	Bulk	Bulk	Bulk	Bulk
SiO2	46.45	47.2	49.9	50.2	48.4	50.07	49.9	44.52	42.9	44.3	42.4
TiO2	0.37	0.55	0.3	1.1	0.4	0.56	0.2	0.11	0.05	0.05	0.05
Al2O3	23.15	15.8	24.3	13.9	23.5	19.72	24.1	25.77	16.2	19.9	24.1
Fe2O3	7.01	10.8	4.9	12.8	7.00	8.99	4.22	6.61	9.9	8.6	6.9
MnO	0.09	0.19	0.1	0.26	0.3	0.16	0.1	0.1	0.14	0.14	0.11
MgO	6.31	9.2	5.3	9	5.1	6.92	5.7	6.79	20.4	13.3	11.2
CaO	14.15	12.7	12.6	10	13.7	11.47	13.5	14.54	9.3	12.6	13
Na2O	1.58	1.5	2	2.3	1.8	2.45	2	1.16	0.95	0.95	1.81
K2O	0.16	0.29	0.5	0.5	0.1	0.18	0.2	0.04	0.27	0.22	0.5
P2O5	0.05	0.03	0.05	0.02	0.1	0.08		0.05	0.01	0.01	0.01
H2O	1							0.59	1.2	1.8	1.7

Buksefjorden

SiO2	49.41	50.33	55.55	49.94	48.99	49.49	50.6	52.94	48.78	47.68
TiO2	0.11	0.182	0.069	0.171	0.064	0.044	0.112	0.035	0.038	0.051
Al2O3	24.25	16.28	26.02	23.46	29.24	29.8	24.44	28.79	30.65	31.02
Fe2O3	4.73	8.66	1.3	5.49	2.05	1.67	4.68	0.77	1.13	1.47
MnO	0.078	0.137	0.019	0.084	0.036	0.022	0.074	0.01	0.017	0.02
MgO	4.36	9.61	1.14	4.21	1.4	0.9	3.8	0.23	0.89	1
CaO	13.78	11.42	11.56	13.28	14.63	4.5	13.23	12.72	15.05	16.07
Na2O	2.22	2.1	3.28	2.22	2.47	2.54	2.18	3.35	2.44	1.86
K2O	0.25	0.27	0.22	0.36	0.2	0.18	0.32	0.16	0.2	0.11
P2O5	0.015	0.005	0.025	0.03	0.011	0.012	0.012	0.006	0.05	0.013
H2O	0.35	0.46	0.25	0.4	0.33	0.31	0.29	0.23	0.45	0.35

Nordland

SiO2	47.31	48.14	49.18	50.65	45.05	51.09	44.12	44.72
TiO2	0.043	0.038	0.059	0.067	0.066	0.06	0.093	0.056
Al2O3	32.6	29.23	30.35	29.14	30.08	27.9	33.12	33.23
Fe2O3	0.93	2.04	1.56	1.76	2.39	1.75	1.82	1.56
MnO	0.015	0.031	0.019	0.028	0.032	0.033	0.023	0.021
MgO	0.21	2.98	0.5	0.7	2.53	1.32	1.35	1.21
CaO	16.06	14.65	14.35	13.64	15.73	12.9	17.49	16.99
Na2O	2.05	2.14	2.77	3.33	1.72	3.55	0.92	1.19
K2O	0.17	0.24	0.21	0.27	0.31	0.31	0.29	0.23
P2O5	0.007	0.007	0.054	0.027	0.022	0.029	0.029	0.014
H2O	0.2	0.34	0.32	0.19	0.4	0.51	0.32	0.24

CHAPTER FOUR: A MINERALOGIC SOLUTION TO THE MARTIAN XE PARADOX

John A. Krantz[a], Kevin M. Cannon[b], Stephen W. Parman[a]

a Department of Earth, Environmental, and Planetary Sciences,

Brown University, Providence, RI

b University of Central Florida, Department of Physics, Orlando, FL

Submitted to:

Geochemical Perspective Letters

16 October 2019

Abstract

Xenon isotopic ratios in the Martian atmosphere are dominated by fractionation processes. Superimposed on this smooth fractionation pattern is a large overabundance of ^{129}Xe from within 100 Myr after solar system formation. Similarly, a range of Xe isotopes were produced over the first 500 Myr, however, there are no overabundances of these Xe isotopes in the Martian atmosphere. Retaining early radiogenic ^{129}Xe, while later Xe isotopes are lost is an apparent paradox. We demonstrate that hydrous minerals, especially clays, produced in the crust in the presence of an early steam atmosphere and hydrosphere (~10 Myr after accretion) could have incorporated and sequestered substantial amounts of ^{129}Xe. Subsequent atmospheric loss would have removed Xe from the atmosphere, but sequestered ^{129}Xe would be protected from this loss. The sequestered Xe could be reintroduced to the atmosphere over billion-year timescales, producing the ^{129}Xe anomaly seen today without creating anomalies in the other Xe isotopes. If excavated exposures of these primordial clays are present on Mars today, analyzing their noble gas contents should distinguish them from later hydrated silicates produced by low-temperature weathering.

Letter

Xenon isotopes in the atmospheres of Earth (Avice *et al.*, 2017; Pujol *et al.*, 2011) and Mars (Atreya *et al.*, 2013; Hutchins and Jakosky, 1996) preserve records of massive atmospheric loss. Light Xe isotopes are depleted relative to heavy Xe isotopes in both Earth and Mars's atmosphere (Fig. 1). This fractionation was produced by hydrodynamic escape (Conrad *et al.*, 2016; Pepin, 1991), a process in which light components of the atmosphere (*e.g.*, H_2, H_2O, and CO) entrain components that are too heavy to escape otherwise, such as Xe. Hydrodynamic escape is mass dependent, producing the smooth, monotonically increasing overall fractionation pattern seen in

Xe isotopes (Fig. 1). The extent of Xe isotope fractionation is similar on Mars and Earth (Mathew *et al.*, 1998), despite much greater overall atmospheric loss on Mars (Swindle, 2002).

Xe has 9 stable isotopes and is particularly useful for understanding atmospheric evolution on rocky planets. Two short-lived decay systems are sensitive to early atmospheric processes: ^{129}I-^{129}Xe ($t_{1/2}$=15.7 Myr) and ^{244}Pu-$^{131\text{-}136}$Xe ($t_{1/2}$=80.8 Myr). Due to their different half-lives, I-derived Xe (Xe_I) would be abundant in the earliest atmosphere of Mars (< 20 Myr) while Pu-derived Xe (Xe_{Pu}) would not be present in appreciable amounts until nearly 100 Myr after formation. Both these short-lived isotopes are seen in the Earth's mantle and atmosphere, while the Martian atmosphere has a much larger ^{129}Xe anomaly than Earth, but no measurable Xe_{Pu} anomaly.

In the Earth's atmosphere, small anomalies of both Xe_I and Xe_{Pu} are superimposed on the smooth mass-fractionation pattern (Porcelli and Ballentine, 2002) (Fig. 1). These are likely relics of the early atmosphere that were not entirely removed by hydrodynamic escape. The Earth's mantle sequestered early Xe_I and Xe_{Pu}, however, the total Xe_I in Earth's atmosphere cannot be accounted for by mantle degassing (Porcelli and Ballentine, 2002). In contrast, the Martian atmosphere has no Xe_{Pu} anomaly (Avice *et al.*, 2018; Conrad *et al.*, 2016; Ozima and Podosek, 2002; Swindle, 2002), suggesting complete loss during atmospheric escape in the first 500 Myr after CAI formation. However, it also has a large Xe_I anomaly (~50x Earth) (Avice *et al.*, 2018; Bogard and Garrison, 1998; Conrad *et al.*, 2016; Garrison and Bogard, 1998; Mathew *et al.*, 1998) which was produced in the first 60 Myr (Fig. 1). The presence of such a large Xe_I anomaly in the Martian atmosphere, with no corresponding Xe_{Pu} anomaly, is difficult to explain by atmospheric escape models, and defines an apparent paradox: how did the complete loss of Xe_{Pu} after 500 Myr not

also erase the Xe_I anomaly? Some models suggest iodine could be concentrated in the crust to produce the Xe_I anomaly, but do not explain the absence of Xe_{Pu} (Musselwhite *et al.*, 1991; Musselwhite and Drake, 2000). Any process that removed Xe_{Pu} from the Martian atmosphere should also have removed any Xe_I in the atmosphere. Xe_I must have been protected from hydrodynamic escape, likely by sequestration in the Martian interior. Like Earth's mantle, the Martian mantle has both Xe_I and Xe_{Pu} (Mathew and Marti, 2001, 2002; Ott, 1988), and so mantle degassing cannot explain the absence of Xe_{Pu} in the modern atmosphere. This suggests a third reservoir exists on Mars, which sequestered Xe_I, but not Xe_{Pu}. Given their different half-lives, one possibility is that this third reservoir formed very early in Mars's history, before substantial Xe_{Pu} was produced.

Recent work suggests a substantial volume of hydrous minerals could be produced in the Martian crust during the first tens of Myr after solar system formation (Cannon *et al.*, 2017; Wade *et al.*, 2017). Outgassing of Mars's magma ocean likely produced a dense, hot atmosphere—and possibly a condensed hydrosphere—which would have rapidly altered the mafic volcanic crust (Cannon *et al.*, 2017; Elkins-Tanton, 2008; Wade *et al.*, 2017). Using an updated crustal evolution model (see Supplementary Methods for details), we find ~8×10^{18} kg of originally buried primordial clay should end up in the upper 10 km of crust (*i.e.* above the pore closure depth) due to impact excavation (Fig. 2). This equates to a Global Equivalent Layer (GEL) of ~25 m. Our previous experimental studies have shown that phyllosilicates have noble gas solubilities orders of magnitude greater than common mantle silicates (Jackson *et al.*, 2013, 2015; Krantz *et al.*, 2019). Therefore, the primordial clays should have trapped substantial amounts of Xe directly from the early Martian atmosphere, forming an early reservoir that can explain the observed discrepancies in Martian Xe data.

To explore this idea, we incorporated Xe sequestration in an early hydrous crustal reservoir into existing hydrodynamic escape models (Conrad *et al.*, 2016; Meshik *et al.*, 2014) (Fig. 3; see Supplementary Methods for description of model). Mixing sequestered Xe with an atmosphere highly fractionated by hydrodynamic escape produces a close fit to observations of modern Martian atmosphere (Fig. 4). The gases trapped in hydrous minerals are those representing the initial, pre-loss atmosphere of Mars (solar wind-like Xe) with the addition of Xe_I. The lack of Xe_{Pu} reflects the very early nature of the sequestration, prior to any significant production of these isotopes. The modern atmosphere can be fit by a range of parameters because variations in the extent of isotopic fractionation are balanced by variations in the mixing ratio of sequestered gas and post-escape atmosphere: a less fractionated post-escape atmosphere can be mixed with less of the sequestered component to produce the modern atmosphere.

The total volume of clays required to trap the equivalent of the modern Martian atmosphere's Xe is a function of both the time at which hydrous minerals form and the degree to which Xe is retained within the host minerals (Supplementary Figure S-1). For 100 % retention of Xe in the clays, a very small volume is needed (~15-20 cm GEL). In the more likely cases where the hydrous minerals do not retain all their initial Xe, the required volume increases linearly as a function of retention. For retention rates as low as 10 %, an equivalent layer 1.5-2 m thick is required, far less than the 25 m in model runs. For cases where clays form earlier, there is less ^{129}Xe available in the atmosphere, and a larger volume is required to trap the same amount of ^{129}Xe. For simplicity, all gases produced during the first 10 Myr after CAI formation are lost during planetary accretion in our model. If this window of loss were narrower, or non-existent, the Xe_I contents of the early atmosphere increase by as much as 90 % whereas Xe_{Pu} is increased

by only 13 %. Conversely, if the period of loss lasted twice as long, 48 % less Xe_I and 12 % less Xe_{Pu} would be retained. In all our models, essentially all Xe_I in the modern atmosphere comes from the hydrous mineral reservoir. Additionally, sequestered Xe_{Pu} accounts for 4 % or less of the modern $^{131\text{-}136}Xe$, consistent with independently derived constraints wherein nearly all of the $^{131\text{-}136}Xe$ is primordial (Conrad *et al.*, 2016).

Any primordial hydrous minerals present in the modern crust should preserve Xe isotope ratios closer to solar wind than the modern atmosphere and should be easily distinguished from later-formed smectites and chlorites produced by low-temperature alteration and diagenesis in crustal aquifers or surface weathering environments (Bishop *et al.*, 2018; Ehlmann *et al.*, 2011). Measurement of solar wind-like Xe in clays would be direct evidence of their production in an early steam atmosphere or hydrosphere. Relative amounts of Xe_I and Xe_{Pu} in samples could also be used to place constraints on the timing of clay formation as well as the timing and extent of magma ocean degassing. Current instruments deployed to Mars are unable to directly measure these trapped gases, however, future missions may be able to provide data via in-situ analysis or sample return.

While such a distinct ^{129}Xe anomaly has only been observed on Mars, the modelled processes could operate on other planetary bodies. The lack of a large anomaly on Earth is consistent with the absence of early (pre-4.0 Ga) crust at the surface due to plate tectonics. Like Earth, Venus has been resurfaced and primordial materials are unlikely to have been preserved. Tectonically inactive bodies—like Ceres and Vesta—are more likely to preserve primordial materials. While they have essentially no atmosphere today, measurements of Xe isotopes representing early outgassing in primordial materials would provide a variety of new constraints on their formation.

Likewise, analyzing noble gases in samples from other planetary bodies would open a window to their earliest evolutionary histories.

Acknowledgements

This work was supported by NSF EAR 1347772 to S.W.P.

Author Contribution

J.A.K. conceived the idea in discussion with K.M.C. and S.W.P. and performed initial calculations of solubility and fractionation. K.M.C. performed crustal evolution modeling. All authors contributed to writing the final manuscript.

References

Atreya, S.K. *et al.* (2013) Primordial argon isotope fractionation in the atmosphere of Mars measured by the SAM instrument on Curiosity and implications for atmospheric loss. *Geophysical Research Letters* 40, 5605–5609.

Avice, G., Bekaert, D.V., Chennaoui Aoudjehane, H., Marty, B. (2018) Noble gases and nitrogen in Tissint reveal the composition of the Mars atmosphere. *Geochemical Perspectives Letters* 6, 11–16.

Avice, G., Marty, B., Burgess, R. (2017) The origin and degassing history of the Earth's atmosphere revealed by Archean xenon. *Nature Communications*. Nature Publishing Group 8, 1–9.

Basford, J.R., Dragon, J.C., Pepin, R.O., Coscio, M.R., J., Murthy, V.R. (1973) Krypton and Xenon in lunar fines. *Proceedings of the Lunar Science Conference* 4, 1915.

Bishop, J.L., Fairén, A.G., Michalski, J.R., Gago-Duport, L., Baker, L.L., Velbel, M.A., Gross,

C., Rampe, E.B. (2018) Surface clay formation during short-term warmer and wetter conditions on a largely cold ancient Mars. *Nature Astronomy* 2, 206–213.

Bogard, D.D., Garrison, D.H. (1998) Relative abundances of argon, krypton, and xenon in the Martian atmosphere as measured in Martian meteorites. *Geochimica et Cosmochimica Acta* 62, 1829–1835.

Cannon, K.M., Parman, S.W., Mustard, J.F. (2017) Primordial clays on Mars formed beneath a steam or supercritical atmosphere. *Nature*. Nature Publishing Group 552, 88–91.

Conrad, P.G. *et al.* (2016) In situ measurement of atmospheric krypton and xenon on Mars with Mars Science Laboratory. *Earth and Planetary Science Letters*. Elsevier B.V. 454, 1–9.

Ehlmann, B.L., Mustard, J.F., Murchie, S.L., Bibring, J.P., Meunier, A., Fraeman, A.A., Langevin, Y. (2011) Subsurface water and clay mineral formation during the early history of Mars. *Nature*. Nature Publishing Group 479, 53–60.

Elkins-Tanton, L.T. (2008) Linked magma ocean solidification and atmospheric growth for Earth and Mars. *Earth and Planetary Science Letters* 271, 181–191.

Garrison, D.H., Bogard, D.D. (1998) Isotopic composition of trapped and cosmogenic noble gases in several Martian meteorites. *Meteoritics and Planetary Science* 33, 721–736.

Hutchins, K.S., Jakosky, B.M. (1996) Evolution of Martian atmospheric argon: Implications for sources of volatiles. *Journal of Geophysical Research* 101, 14,933-14,949.

Jackson, C.R.M., Parman, S.W., Kelley, S.P., Cooper, R.F. (2013) Noble gas transport into the mantle facilitated by high solubility in amphibole. *Nature Geoscience*. Nature Publishing Group 6, 562–565.

Jackson, C.R.M., Parman, S.W., Kelley, S.P., Cooper, R.F. (2015) Light noble gas dissolution into ring structure-bearing materials and lattice influences on noble gas recycling. *Geochimica et Cosmochimica Acta*. Elsevier Ltd 159, 1–15.

Krantz, J.A., Parman, S.W., Kelley, S.P. (2019) Recycling of heavy noble gases by subduction of serpentinite. *Earth and Planetary Science Letters*. Elsevier B.V. 521, 120–127.

Mathew, K.J., Kim, J.S., Marti, K. (1998) Martian atmospheric and indigenous components of xenon and nitrogen in the Shergotty, Nakhla, and Chassigny group meteorites. *Meteoritics & Planetary Science* 33, 655–664.

Mathew, K.J., Marti, K. (2001) Early evolution of martian volatiles: Nitrogen and noble gas components in ALH84001 and Chassigny. *Journal of Geophysical Research E: Planets* 106, 1401–1422.

Mathew, K.J., Marti, K. (2002) Martian atmospheric and interior volatiles in the meteorite Nakhla. *Earth and Planetary Science Letters* 199, 7–20.

Meshik, A., Hohenberg, C., Pravdivtseva, O., Burnett, D. (2014) Heavy noble gases in solar wind delivered by Genesis mission. *Geochimica et Cosmochimica Acta*. Elsevier Ltd 127, 326–347.

Meshik, A., Pravdivtseva, O., Burnett, D. (2018) New analyses of Solar Wind Xenon: Confirmation of earlier Genesis mission results and thire implications. *49th Lunar and Planetary Science Conference* 1–2.

Meshik, A., Pravdivtseva, O., Hohenberg, C., Burnett, D. (2015) Refined composition of Solar Wind xenon delivered by Genesis: Implication for primitive terrestrial xenon. *46th Lunar and Planetary Science Conference* 1–2.

Musselwhite, D.S., Drake, M.J. (2000) Early Outgassing of Mars: Implications from Experimentally Determined Solubility of Iodine in Silicate Magmas. *Icarus* 148, 160–175.

Musselwhite, D.S., Drake, M.J., Swindle, T.D. (1991) Early outgassing of Mars supported by differential water solubility of iodine and xenon. *Nature* 352, 697–699.

Ott, U. (1988) Noble gases in SNC meteorites: Shergotty, Nakhla, Chassigny. *Geochimica et*

Cosmochimica Acta 52, 1937–1948.

Ozima, M., Podosek, F.A. (2002) *Noble Gas Geochemistry*. Cambridge University Press.

Pepin, R.O. (1991) On the origin and early evolution of terrestrial planet atmospheres and meteoritic volatiles. *Icarus* 92, 2–79.

Porcelli, D., Ballentine, C.J. (2002) Models for Distribution of Terrestrial Noble Gases and Evolution of the Atmosphere. *Reviews in Mineralogy and Geochemistry* 47, 411–480.

Pujol, M., Marty, B., Burgess, R. (2011) Chondritic-like xenon trapped in Archean rocks: A possible signature of the ancient atmosphere. *Earth and Planetary Science Letters*. Elsevier B.V. 308, 298–306.

Swindle, T.D. (2002) Martian Noble Gases. *Reviews in Mineralogy and Geochemistry* 47, 171–190.

Wade, J., Dyck, B., Palin, R.M., Moore, J.D.P., Smye, A.J. (2017) The divergent fates of primitive hydrospheric water on Earth and Mars. *Nature*. Nature Publishing Group 552, 391–394.

Figure 1 Xenon isotopic composition of the atmospheres of Earth and Mars (Basford *et al.*, 1973; Conrad *et al.*, 2016). Values are plotted as δ-values referenced to solar wind (Meshik *et al.*, 2014, 2015, 2018), where $\delta^{M}=[(^{M}Xe/^{132}Xe)_{Observed}/(^{M}Xe/^{132}Xe)_{SW}-1]\cdot 1000$ ‰. Both planets preserve smooth, mass-dependent fractionation trends resulting from hydrodynamic escape, a mass-dependent process in which heavier isotopes are preferentially preserved. The addition of I-derived ^{129}Xe produces a clear anomaly in this smooth pattern. The short half-life of ^{129}I requires this anomaly be produced within the first 100 Myr after solar system formation. Due to discrepancies in measurements of modern Martian ^{124}Xe and ^{126}Xe, for reasons that remain unclear, these isotopes have not been considered in assessing the quality of mixing models (Avice *et al.*, 2018; Conrad *et al.*, 2016).

Figure 2 Plan view and cross section of crustal evolution model. Distribution of different clay types (primordial and later-formed) in the Martian southern highlands crust. **(a)** Plan view of the upper surface of the model, where material is dominated by unaltered lavas and clays are found associated with crater walls and ejecta; primordial clays mostly surround large basins in patchy exposures. **(b)** Cross section of the model with cutaways showing all clays and just primordial clays. Primordial clays are mostly sequestered at >20 km depth but are exposed in isolated patches in the upper crust (arrows).

Figure 3 Schematic diagram of Xe sequestration model. **(a)** Volatiles are outgassed from the crystallizing magma ocean to form a thick steam atmosphere with solar wind-like Xe isotope ratios. **(b)** Hydration of the early crust creates clays and sequesters solar wind-like Xe with added ^{129}Xe from the decay of ^{129}I. **(c)** Subsequent hydrodynamic escape and atmospheric loss removes Xe from the atmosphere, including the products of ^{129}I and ^{244}Pu decay. **(d)** Later degassing of the

clays mixes early sequestered atmospheric gases with the post-escape atmosphere to produce the modern atmosphere.

Figure 4 Fractionation and mixing model for an early Martian atmosphere. Values are plotted as δ-values referenced to solar wind (Meshik *et al.*, 2014, 2015, 2018), where $\delta^{M}=[(^{M}Xe/^{132}Xe)_{Observed}/(^{M}Xe/^{132}Xe)_{SW}-1]\cdot 1000$ ‰. The early atmosphere (blue) consists of solar wind-like gases (Meshik *et al.*, 2018) from accretion with the addition of radiogenic ^{129}Xe from the decay of ^{129}I. The atmosphere after hydrodynamic escape (Conrad *et al.*, 2016; Pepin, 1991) (green) is mixed with sequestered early atmospheric gases to produce the modern Martian atmosphere (Conrad *et al.*, 2016) (observed, circles; modelled, red line). Also shown is the best-fit pure hydrodynamic escape model (dashed, black). *Inset*: variation in the modelled extent of fractionation from hydrodynamic escape ($f_{124/130}$) are balanced by variations in the mixing ratio (k) of trapped and post-escape components; shown here is the best-fit model ($f_{124/130}$=0.6263, k=0.41).

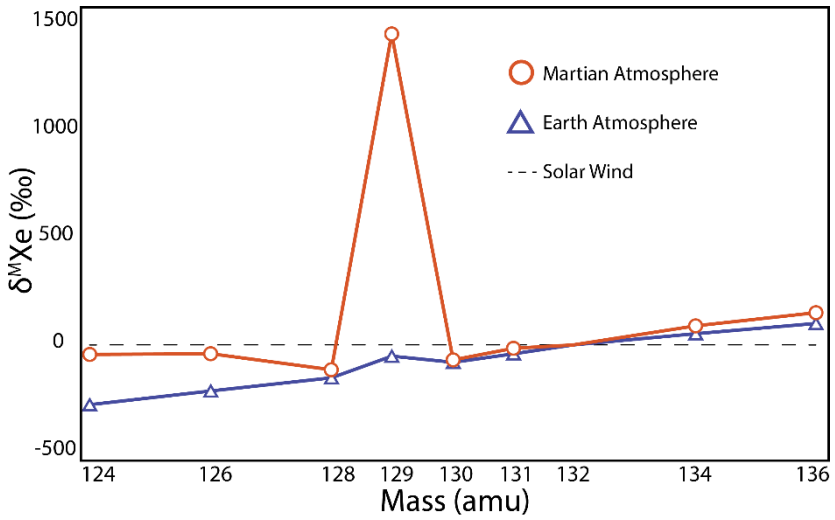
1500
1000
500
0
-500
δ^MXe (‰)
Martian Atmosphere
Earth Atmosphere
Solar Wind
124
126
128
129
130
131
132
134
136
Mass (amu)

Figure 1

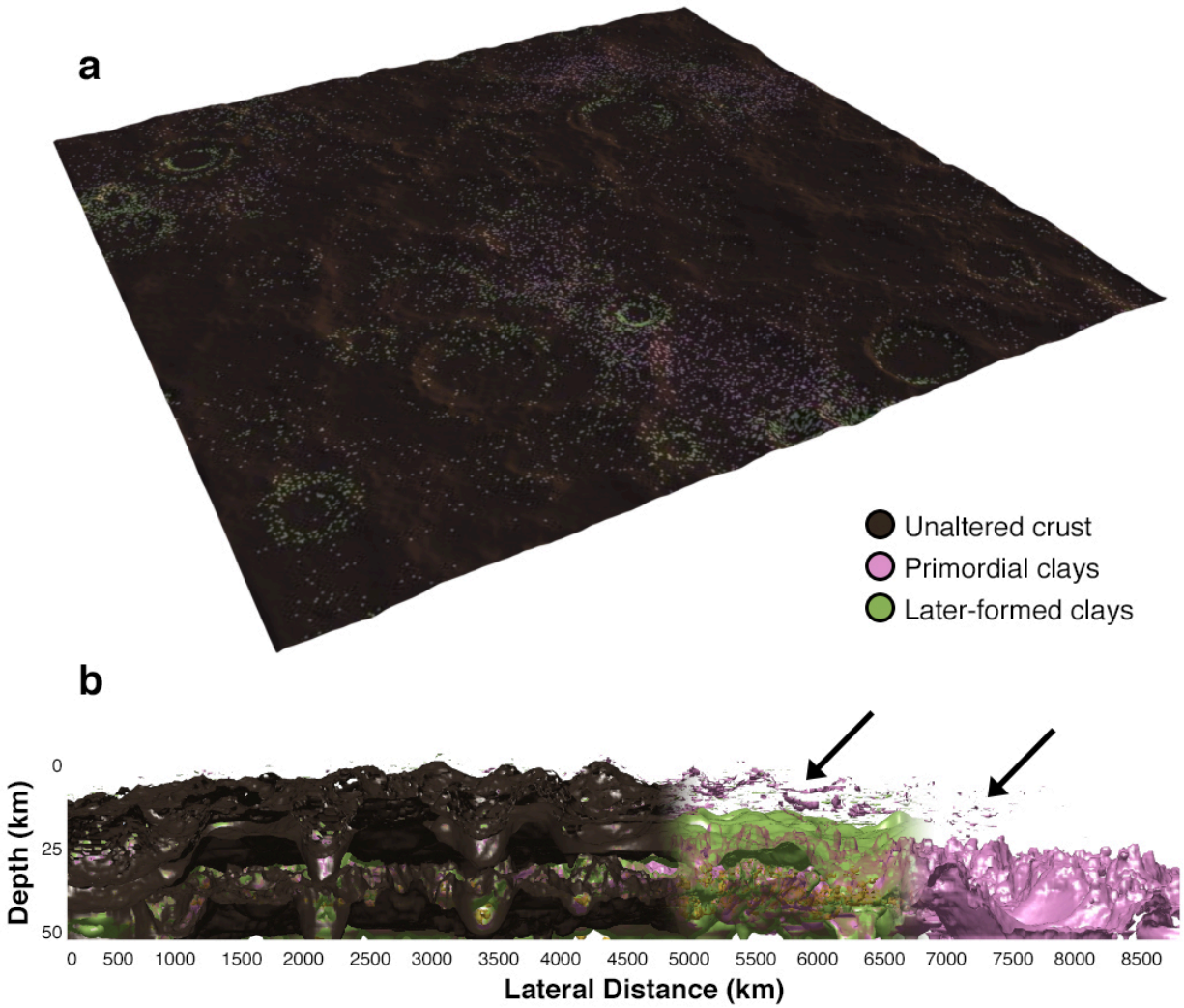
a
Unaltered crust
Primordial clays
Later-formed clays
b
Depth (km)
0
25
50
0 500 1000 1500 2000 2500 3000 3500 4000 4500 5000 5500 6000 6500 7000 7500 8000 8500
Lateral Distance (km)

Figure 2

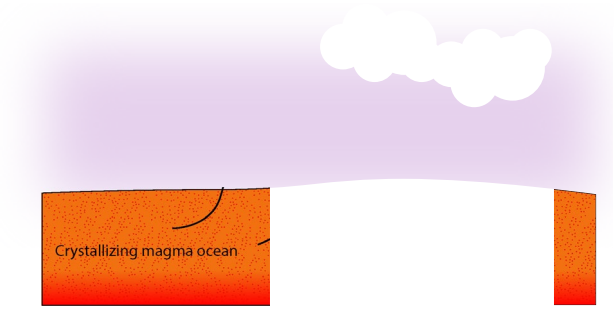

Figure 3

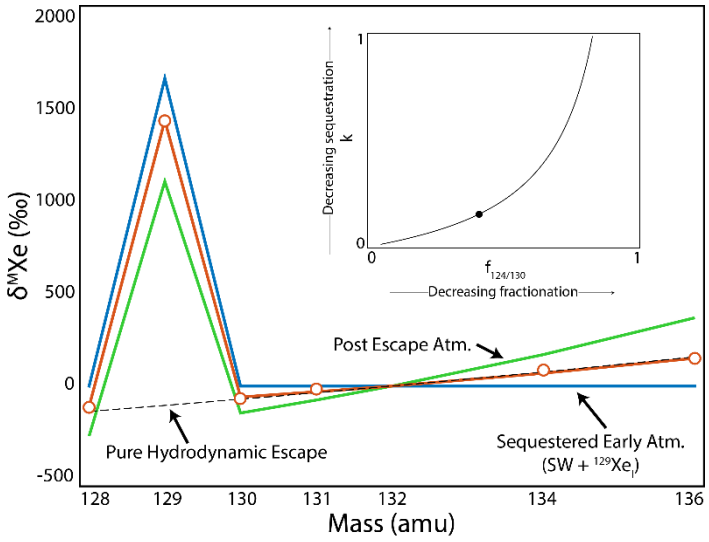
2000
1500
1000
500
0
-500
δ^MXe (‰)
128
129
130
131
132
134
136
Mass (amu)
Pure Hydrodynamic Escape
Post Escape Atm.
Sequestered Early Atm.
(SW + 129Xe_I)
Decreasing sequestration
k
1
0
0
1
f124/130
Decreasing fractionation

Figure 4

Supplementary Information

The Supplementary Information includes:

- Noble Gas Modelling Methods
- Crustal Evolution Modelling Methods
- Table S-1
- Figure S-1
- Supplementary Information References

Noble Gas Modelling Methods

To model the radiogenic and fissiogenic production of Xe, initial compositions of I, U, and Pu in Bulk Silicate Mars were back-calculated to 4.56 Ga (Supplementary Table S-1). Measurements of SNC-meteorites constrain the modern I and U composition (Dreibus and Wanke, 1985), and, based on these modern values, an initial value for U was calculated using the radioactive decay equation:

$$N_0 = N \cdot 2^{\frac{t}{T_{1/2}}} \quad \text{(Eq. S-1)}$$

Where N_0 represents the initial composition, N represents the composition at time t, and $T_{1/2}$ is the half-life for a given isotope. To constrain the initial ^{244}Pu, we assumed isotopic ratios are nebular and reflect those preserved in chondrites (Hudson *et al.*, 1989). Initial ^{129}I was calculated using ^{129}I/^{127}I ratios from measurements of ^{127}I and ^{129}Xe in four C3V and four C3O chondrites (Crabb *et al.*, 1982). Decay products of ^{129}I and ^{244}Pu were assumed to fully degas from the primordial magma ocean, and all Xe produced in the first 10 Myr after solar system formation

was assumed to be lost during accretion. Degassed Xe was then distributed into the early, steam atmosphere, producing solar wind-like Xe isotopic ratios, with excess ^{129}Xe. A cometary origin for Xe was also considered, however, the abundances of the primordial Xe isotopes (^{128,130}Xe) measured from comet 67P are not consistent with the Martian atmosphere (Marty *et al.*, 2017) through direct addition combined with contributions from radioactive decay. Xe, acting as a nearly ideal gas, is concentrated in the atmosphere and then partitioned into hydrous phases (Jackson *et al.*, 2013, 2015; Krantz *et al.*, 2019) as a function of the partial pressure of Xe in the atmosphere and the Henry's Constant for Xe in a representative mineral phase:

$$C^{Xe}_{Mineral} = P^{Xe}_{Atmosphere} \cdot H^{Xe}_{Gas-Min} \text{ (Eq. S-2)}$$

Although serpentine is a rare phase on Mars (Pahlevan *et al.*, 2017), serpentinite was used as the host phase in this model because of the availability of Xe solubility data and structural similarities between smectites and serpentine suggest the partitioning behavior will be similar.

Within the first 10 Myr after solar system formation, the magma ocean begins crystallizing and degassing (Fig. 3a). During this degassing phase, a steam atmosphere is produced and consists of H_2O, CO, and H, or H_2O and CO_2 for reducing and oxidizing conditions, respectively (Elkins-Tanton, 2008; Pahlevan *et al.*, 2017). This dense, hot steam atmosphere also contains I and solar wind-like Xe. Over the following tens of millions of years, a substantial fraction of the ^{129}I decays to ^{129}Xe. During this same time frame, reactions between the steam atmosphere and the early crust begin producing hydrous minerals (Cannon *et al.*, 2017). As these hydrous phases are produced, they trap solar wind-like Xe and additional ^{129}Xe from ^{129}I decay (Fig. 3b). Following sequestration, hydrodynamic escape begins to outweigh degassing. Mass-dependent fractionation during hydrodynamic escape produces a post-escape atmosphere with higher $^{134\text{-}136}$Xe/^{132}Xe ratios, and lower $^{124\text{-}131}$Xe/^{132}Xe ratios (Conrad *et al.*, 2016; Pepin,

1991) (Fig. 3c). Loss of primary and trace volatiles from the atmosphere puts an end to the formation of clays and causes the loss of most Xe in the atmosphere, including Xe_{Pu}. Subsequent outgassing of the primordial clays into the post-escape atmosphere produces the Xe isotopic ratios observed today (Fig. 3d, 4).

Crustal Evolution Modelling Methods

An updated version of the crustal evolution model described in detail by Cannon *et al.* (2017) was used to estimate the mass of primordial clays in the upper crust (10 km) able to exchange with the modern atmosphere (Fig. 2). The entire southern highlands crust of Mars was modeled as a rectangular 3-dimensional grid with a horizontal resolution of 17 km and a vertical resolution of 0.5 km. Each grid cell represents a type of material: unaltered crust, primordial clays, or later clays from subsurface or surface weathering. The model runs from 4.548 Ga (crust formation) to 3.548 Ga with a timestep of 10^5 years. Primordial clays capable of trapping Xe are assumed to form in the uppermost 10 km of crust during the first 10^7 years after crust formation; after this they are affected by parameterized impact cratering (excavation and melting), burial by secondary crust formation, and by the Borealis basin that likely destroyed most of the northern hemisphere crust and deposited ~20 km of melt on the southern hemisphere crust (Marinova *et al.*, 2008). Impact fluxes (Morbidelli *et al.*, 2018) and crustal production rates (Morschhauser *et al.*, 2011) appropriate for Mars were used. Figure 2 shows a plan view and cross section through the crust at the end of the model (minimal changes are observed if the model is run out to present day). The primordial clays are mostly sequestered at depth where they are unlikely to exchange with the atmosphere; however, a small fraction are present in the upper crust due to the excavation effects of later large

impact basins. To calculate the total mass in the upper 10 km of crust, we assumed a lunar-like porosity of 10 % (Wieczorek *et al.*, 2013), an alteration extent of 70 vol. % in primordial clay grid cells, and a conservative clay density of 2200 kg/m^3. The average mass of primordial clays in the upper crust from different model runs was ~8×10^{18} kg, much smaller than that of later-formed clays (~8×10^{20} kg), but more than enough to outgas significant amounts of trapped noble gases, especially considering that a greater proportion of primordial clays should have been present in the upper crust further back in Martian history.

Supplementary Tables

Table S-1 Composition of modern and ancient Bulk Silicate Mars.

	Modern (ppb)	**Ancient (ppb)**	**Ancient (mol)**
^{238}U	15.9	32.2	7.30×10^{16}
^{235}U	0.1	10.4	2.38×10^{16}
^{244}Pu	-	0.225	4.97×10^{14}
^{127}I	37	37	1.55×10^{17}
^{129}I	-	4.97E-03	2.08×10^{13}

Supplementary Figure Captions

Figure S-1 Minimum thickness of hydrous mineral global equivalent layer (GEL) required to trap all ^{129}Xe observed in the modern atmosphere (Conrad *et al.*, 2016). The minimum GEL thickness varies as a function of the time of formation and the fraction of trapped gas retained through hydrodynamic escape processes.

Supplementary Information References

Cannon, K.M., Parman, S.W., Mustard, J.F. (2017) Primordial clays on Mars formed beneath a steam or supercritical atmosphere. *Nature*. Nature Publishing Group 552, 88–91.

Conrad, P.G. *et al.* (2016) In situ measurement of atmospheric krypton and xenon on Mars with Mars Science Laboratory. *Earth and Planetary Science Letters*. Elsevier B.V. 454, 1–9.

Crabb, J., Levels, R.S., Anders, E. (1982) Extinct I 129 in C3 chondrites. *Geochimica et Cosmochimica Acta* 46, 2511–2525.

Dreibus, G., Wanke, H. (1985) Mars, a volatile-rich planet. *Meteoritics* 20, 367–381.

Elkins-Tanton, L.T. (2008) Linked magma ocean solidification and atmospheric growth for Earth and Mars. *Earth and Planetary Science Letters* 271, 181–191.

Hudson, G.B., Kennedy, B.M., Podosek, F.A., Hohenberg, C.M. (1989) The Early Solar System Abundance of 244Pu as Inferred from the St. Severin Chondrite. *Proceedings of the 19th Lunar and Planetary Science Conference* 547–557.

Jackson, C.R.M., Parman, S.W., Kelley, S.P., Cooper, R.F. (2013) Noble gas transport into the mantle facilitated by high solubility in amphibole. *Nature Geoscience*. Nature Publishing Group 6, 562–565.

Jackson, C.R.M., Parman, S.W., Kelley, S.P., Cooper, R.F. (2015) Light noble gas dissolution into ring structure-bearing materials and lattice influences on noble gas recycling. *Geochimica et Cosmochimica Acta*. Elsevier Ltd 159, 1–15.

Krantz, J.A., Parman, S.W., Kelley, S.P. (2019) Recycling of heavy noble gases by subduction of serpentinite. *Earth and Planetary Science Letters*. Elsevier B.V. 521, 120–127.

Marinova, M.M., Aharonson, O., Asphaug, E. (2008) Mega-impact formation of the Mars hemispheric dichotomy. *Nature* 453, 1216–1219.

Marty, B. *et al.* (2017) Xenon isotopes in 67P/Churyumov-Gerasimenko show that comets contributed to Earth's atmosphere. *Science* 356, 1069–1072.

Morbidelli, A., Nesvorny, D., Laurenz, V., Marchi, S., Rubie, D.C., Elkins-Tanton, L., Wieczorek, M., Jacobson, S. (2018) The timeline of the lunar bombardment: Revisited. *Icarus*. Elsevier Inc. 305, 262–276.

Morschhauser, A., Grott, M., Breuer, D. (2011) Crustal recycling, mantle dehydration, and the thermal evolution of Mars. *Icarus*. Elsevier Inc. 212, 541–558.

Pahlevan, K., Desch, S.J., Schaefer, L.K., Elkins-tanton, L.T. (2017) A massive hydrogen-rich Martian greenhouse recorded in D/H. *AGU Fall Meeting 2017* Abstract P31F-02.

Pepin, R.O. (1991) On the origin and early evolution of terrestrial planet atmospheres and meteoritic volatiles. *Icarus* 92, 2–79.

Wieczorek, M.A. *et al.* (2013) The Crust of the Moon as Seen by GRAIL. *Science* 339, 671–675.

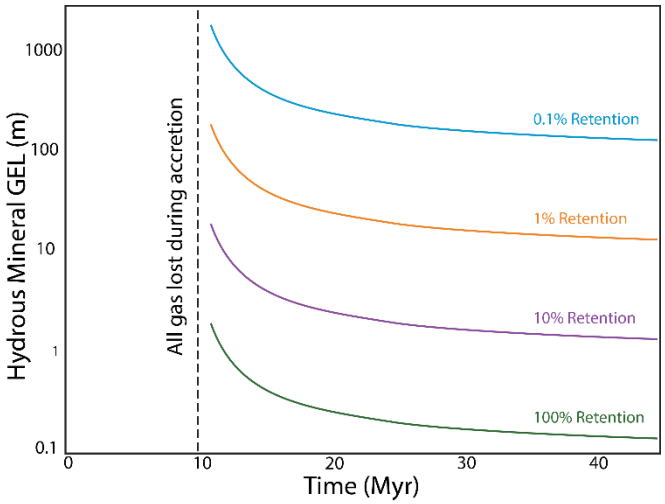
1000
100
10
1
0.1
Hydrous Mineral GEL (m)
All gas lost during accretion
0.1% Retention
1% Retention
10% Retention
100% Retention
0
10
20
30
40
Time (Myr)

Figure S-1

SYNTHESIS

"Trust the data, not the interpretations… and not always the data."
-RF Cooper

"Remember that all models are wrong; the practical question is how wrong do they have to be to not be useful."
-George Box, *Empirical Model-Building and Response Surfaces*

"Ce qui est simple est toujours faux. Ce qui ne l'est pas est inutilisable."
What is simple is always wrong. What is not is unusable.
-Paul Valéry, *Mauvaises pensées et autres*

The noble gases themselves are not hugely impactful; their role as volatiles is negligible in comparison to water, carbon, and nitrogen. Chemically, they are inert and lack the crucial characteristics of other volatiles in making the Earth, so far, unique as a life-sustaining planet. Carbon, oxygen, hydrogen, nitrogen, sulfur, and phosphorus, are essential to sustaining life and have enormous impacts on climate, mantle dynamics, and nearly every other major planetary process. As geologists, however, we are interested not only in the current state of the Earth, but how it has evolved through time. It is in tracing that evolution that the noble gases are unparalleled. Where the other volatiles are important because of the way that they interact chemically, the inert nature of noble gases can be leveraged to understand the origin and motion of volatiles.

The exchange of noble gases between surface reservoirs and multiple, distinct mantle reservoirs is the result of physical processes the scope of which far exceeds volatiles. By

improving our understanding of noble gas systematics, constraints can be placed on any number of mantle processes. With this in mind, this thesis leads to two primary areas of research which will require analytical, empirical, and numerical approaches:

Where are they? What are the isotopic ratios and concentrations of noble gases in the mantle-plume end-members? To what degree does MORB preserve mantle heterogeneities in the noble gases? Where are they stored within the solid Earth, with an emphasis on potential storage in the core and during subduction?

Where did they come from? Do the noble gases within disparate mantle reservoirs correlate with different accretionary events? If so, can the relative contribution of these events to the planetary volatile budget be determined?

Numerical

The most immediate of these approaches will be numerical, namely, a substantial improvement to the models presented in Chapter 2. The model, in its current state, is an extreme simplification, which has had its value. Emergent behavior in the model (e.g., downwelling of more reactive volatiles begins earlier) is an excellent indicator of the model's potential. In such a simple model, this behavior hasn't been "added" by the modeller but results from the necessity of meeting the constraints applied. If we had started with a more complex model, perhaps one which prescribes the timing and rate of subduction for example, it would not have been possible to gain such confidence in the model. That said, the model has its shortcomings, including: the atmosphere is treated as an infinite reservoir and the lack of plume source or reservoir.

The next generation of this model will need to make substantial improvements, some of which I will enumerate herein. As discussed in Chapter 2, the N isotopic composition of the Earth's atmosphere has been constant since the Archean. While it is possible that this represents some form of modern atmospheric contamination, we must explore a case in which it is accurate. For the atmosphere not to have changed, the most probable series of events is one in which only a negligible fraction of the atmosphere has been removed via subduction or added via degassing. A future iteration of the model in which the atmosphere has a finite concentration, and which allows for loss of atmospheric gases to space.

One of the most fundamental findings from analyses of N in natural samples is that MORBs and OIBs have isotopically distinct N, as has long been clear for other volatiles (e.g., He). As discussed in Chapter 1, the noble gases are not recycled equally. OIBs with recycled atmospheric Xe alongside primordial He and Xe exist and must be accounted for. Future iterations of the model must allow for degassing and regassing of the MORB and OIB sources separately. Treating these sources separately requires that the relative contributions of the two reservoirs must be allowed to vary through time, as must the fraction of recycled volatiles being regassed to each. Additional consideration must also be given to the possibility that primordial gases in plumes originate within the core.

An additional direction to be explored by new versions of the model will be aimed at early, massive atmospheric loss events. There is no shortage of evidence that Earth's atmosphere was lost as a result of impact events, at least once (e.g., Tucker and Mukhopadhyay, 2014). If not a necessary component of a new finite atmosphere model, atmospheric loss events will be crucial to constraining the relative contribution of different meteorites to the accreting Earth.

Empirical

In addition to themselves producing new findings, constraints from the rock record are required to inform and validate any numerical approach. High quality analyses of Xe continue to reveal new information about the interplay of MORB and OIB sources (e.g., Parai *et al.*, 2019; Parai and Mukhopadhyay, 2018; Tucker *et al.*, 2018) and the evolution of the atmosphere (e.g., Avice *et al.*, 2017; Bekaert *et al.*, 2018, 2019; Parai and Mukhopadhyay, 2018). Likewise, numerous studies have exploited nitrogen isotopes ($\delta^{15}N$) in mantle-derived fluids and rocks to address issues such as the formation of Earth's atmosphere, the origin of volatiles in the terrestrial mantle, as well as the degassing history of Earth (see Chapter 2). The foundation of many of these studies is based on the interpretation of high-quality $\delta^{15}N$ data from mantle-derived materials (i.e., oceanic basalts and mantle xenoliths), many of which contain extremely small amounts of N. However, the $\delta^{15}N$ database is surprisingly small, particularly for major terrestrial reservoirs such as the oceanic mantle. Recently, the analytical capabilities of making low-level $\delta^{15}N$ measurements have been developed. Analyzing key samples – well characterized for their other chemical and isotopic properties – will allow for the characterization of $\delta^{15}N$ variations in various mantle reservoirs.

Experimental

Additional constraints on the origin of volatiles within the solar system can be produced experimentally. The primary carrier of noble gases within meteorites, for example, is the poorly characterized Phase Q. It is thought to be a mixture of organics and sulfides. The noble gases released during thermal and chemical analyses of Phase Q exhibit behaviour similar to that of iron sulfides found in meteorites. These same Phase Q gases are observed in chondrites independent of their alteration history, and Phase Q-bearing sulfides thus preserve evidence of the

conditions that existed during the period of chondrule formation. Future work experimentally characterizing the solubility of noble gases in meteoritic sulfides has the potential to provide constraints on the portion of Phase Q gases which can be stored in sulfides, and thereby constrain the noble gas contents of the solar system during chondrule formation. Alongside empirical results, experimentally characterizing the properties of Phase Q and other carriers of noble gases in the early solar system will allow for the production of models which predict the relative contribution of different types of meteorites to the accreting Earth.

References

Avice, G., Marty, B., Burgess, R. (2017) The origin and degassing history of the Earth's atmosphere revealed by Archean xenon. *Nature Communications*. Nature Publishing Group 8, 1–9.

Bekaert, D. V., Broadley, M.W., Caracausi, A., Marty, B. (2019) Novel insights into the degassing history of Earth's mantle from high precision noble gas analysis of magmatic gas. *Earth and Planetary Science Letters*. Elsevier B.V. 525, 115766.

Bekaert, D. V., Broadley, M.W., Delarue, F., Avice, G., Robert, F., Marty, B. (2018) Archean kerogen as a new tracer of atmospheric evolution: Implications for dating the widespread nature of early life. *Science Advances* 4, 1–9.

Parai, R., Mukhopadhyay, S. (2018) Xenon isotopic constraints on the history of volatile recycling into the mantle. *Nature*. Springer US 560, 223–227.

Parai, R., Mukhopadhyay, S., Tucker, J.M., Pető, M.K. (2019) The emerging portrait of an ancient, heterogeneous and continuously evolving mantle plume source. *Lithos* 346–347, 105153.

Tucker, J.M., Mukhopadhyay, S. (2014) Evidence for multiple magma ocean outgassing and

atmospheric loss episodes from mantle noble gases. *Earth and Planetary Science Letters*. Elsevier B.V. 393, 254–265.

Tucker, J.M., Mukhopadhyay, S., Gonnermann, H.M. (2018) Reconstructing mantle carbon and noble gas contents from degassed mid-ocean ridge basalts. *Earth and Planetary Science Letters*. Elsevier B.V. 496, 108–119.